Universität der Bundeswehr München
Fakultät für Luft- und Raumfahrttechnik
Institut für Strömungsmechanik und Aerodynamik

Thermo-Liquid Crystal (TLC) Thermography and Astigmatism Particle Tracking Velocimetry (APTV) for the simultaneous time-resolved 3D measurements of microscopic temperature and velocity flow fields

M. S. Rodrigo Segura

Vollständiger Abdruck der bei der
Fakultät für Luft- und Raumfahrttechnik
der Universität der Bundeswehr München
zur Erlangung des akademischen Grades eines

Doktor der Ingenieurwissenschaften (Dr.-Ing.)

eingereichten Dissertation

Vorsitzender: Markus Klein
1. Berichterstatter: Christian J. Kähler
2. Berichterstatter: Michael Schlüter

Diese Dissertation wurde am 10.06.2014 bei der Universität der Bundeswehr München, 85577 Neubiberg eingereicht und durch die Fakultät für Luft- und Raumfahrttechnik am 16.06.2014 angenommen.

Tag der Prüfung: 10.11.2014

Este trabajo va dedicado a mi papá y mi mamá.

ACKNOWLEGEMENTS

I want to thank Professor Christian J. Kähler for inviting me to take part in his research team at the Institute of Fluid Mechanics and Aerodynamics (LRT7) of the Universität der Bundeswehr München, and allowing me the opportunity to work on this project. Had it not been for his vote of confidence and his patience, the achievements reported in this document would not have become a reality. Furthermore, his expertise and prompt counsel were of great help in overcoming a myriad of challenges during the course of my scientific work here. I would also like to thank Professor Markus Klein for agreeing to be chairman of my committee, and Professor Michael Schlüter for serving as second reviewer. Their time and suggestions are appreciated.

My coming to Germany and my involvement in Professor Kähler's group was made possible by the support of the German Research Foundation (DFG). I am grateful to have been part of the Mikropart research group FOR 856, under which my research was financially supported. I thank Professor Arno Kwade and Ingo Kampen for structuring and managing the collaboration and the general project. I would also like to thank Professor Heike Bunjes, Sonja Joseph and Sandra Gehrmann, at the Institute of Pharmaceutical Technology of the Technische Universität Braunschweig, for their essential collaboration in the manufacture of materials for the experiments here presented.

My fluency in the German language was never good and I want to thank Elzbieta Hamerski and Marion Kranz, who played an indispensable role in assisting me to comply with the endless bureaucracy required to keep things in the proper German order. Johann Hofer and Ludwig Kassecker, of the technical staff at the LRT7, were very helpful during the course of the project and I thank them for their time and support in the manufacture of custom parts for my experimental arrangements.

None of this would have been possible without the invaluable technical assistance and guidance of my fellow researchers. I must say that all my achievements during this time stand on the shoulders of their wisdom and collaboration. I would like to express my infinite gratitude to Massimiliano Rossi and Christian Cierpka for their help, support, patience, constructive criticism and camaraderie without which completing the work that I am now reporting would have been orders of magnitude more difficult if not impossible. I would also like to thank Rainer Hain, Sven Scharnowski, Dirk Sonnemann, and Rune Barnkob for their regular help and technical advice.

Of course, though their role is not directly related to my scientific development or that of the project, I do not know how I would have managed to complete this work without the company of those people whose precious friendship contribute to my day-to-day well-being and strengthen my will to continue. My special thanks go to Daniel Correa, Rodrigo Guevara, Camila Botero, Monica Ramirez, Javier Lopez, Carolina Camacho, Julio Ortiz, Lis Hebel, Teo Mezger, Natalia Breton, Erwin Smit, Lorena Galvis, Jens Ower, Michelle Hines, Andre Pedroso, Nicolas Ruiz, Oscar Ardila, Luis Guillermo Arboleda, Jaime Andres Rueda, and my brother Luis Carlos Segura. Your friendship and constant company

were crucial in my survival these years. I also want to give special thanks to Katja Zhuk for standing by me and caring for me the way she has. To her friendship, company and love I owe a substantial personal evolution and growth over the last four years.

And most importantly, I want to say thank you to my mom and my dad. Thank you for being there, willing and available, at all times. You are the meaning of this life. I love you.

TABLE OF CONTENTS

LIST OF FIGURES

SYMBOLS

$\delta\lambda$	reflection bandwidth
λ	wavelength / eigenvalue
μ	micro
σ	standard deviation from true value
$\times$	times
n	index of refraction
p	molecular pitch

Superscripts

$-$	mean
-1	inverse
t	Transpose

Subscripts

max	maximum
meas	measured value
min	minimum
real	real

Acronyms

2D	Two-dimensional
3C	Three-component
3D	Three-dimensional
APTV	Astigmatism Particle Tracking Velocimetry
CCD	Charge-Coupled Device
CIE	Commission International de l'Éclairage
DFG	Deutsche Forschungsgemeinschaft (German Research Foundation)
HSI	Hue, Saturation, Intensity
IR	Infrared
LC	Liquid Crystal
NA	NumericalAperture
LIF	Laser Induced Fluorescence
PIV	Particle Image Velocimetry
POD	Proper Orthogonal Decomposition
PTV	Particle Tracking Velocimetry
RGB	Red, Green, Blue
SNR	Signal-to-Noise Ratio
SPG	Shirasu Porous Glass
TLC	Thermo-Liquid Crystal

ABSTRACT

Segura, Rodrigo. M. S., Universität der Bundeswehr München, 16.06.2014. Thermo-Liquid Crystal (TLC) Thermography and Astigmatism Particle Tracking Velocimetry (APTV) for the simultaneous time-resolved 3D measurements of microscopic temperature and velocity flow fields. Professor: Christian J. Kähler.

The ever accelerating state of technology has powered an increasing interest in heat transfer solutions and process engineering innovations in the microfluidics domain, many of which require reliable temperature flow diagnostic techniques. Thermo-liquid crystal (TLC) thermography has been a widely accepted and commonly used technique for the measurement of temperature fields in macroscopic flows. Furthermore, its combination with optical velocimetry techniques, such as Particle Image Velocimetry (PIV), has provided a means to simultaneously characterize macroscopic two-dimensional (2D) temperature and velocity flow fields. Unfortunately, however, the state of technology has not allowed for this task to be carried out in microscopic flows. Low seeding density, volume illumination, and low TLC particle image quality at high magnifications present unsurpassed challenges to its application to three-dimensional flows with microscopic dimensions. In the following chapters, a combination of cutting edge technology is presented as a means to accomplish precisely this objective: to simultaneously measure time-resolved 3D temperature and velocity fields in microscopic flows where multi-camera methods and light sheets are not possible. The process of achieving this goal happened in three phases: 1. TLC thermography had to be improved and adapted to the point where the temperature of individual particles could be evaluated and tracked over time. An emulsion of TLC micro spheres (with a narrow size distribution and no encapsulation) was manufactured to improve the image quality of TLC particles and a multi-variable calibration approach, applied to a mathematically optimal variable space, was developed to improve the estimation of temperature from color information. 2. Astigmatism Particle Tracking Velocimetry (APTV) was developed to precisely locate particles in a flow volume and track their displacement in three dimensions (3D). 3. The the signal-to-noise ratio (SNR) of TLC images had to be improved enough for the application of defocusing techniques, such as APTV, which encode the third component of the particles' position in their images' geometry. A state-of-the-art balanced light source which combines the light spectrum of multiple light pipes was used instead of the conventional high power flash lamps and a circular polarization filter was designed to exploit the optical properties of chiral nematic polymers. This combination made it possible to boost the SNR just enough for the combination of TLC thermography and APTV to work. Finally, a proof-of-concept experiment was performed in a simple microscopic flow example, and the 3D displacement of TLC particles was tracked simultaneously with their temperature. More complex applications were not possible due to current technological hardware limitations but the capability and potential of the measurement technique was clearly demonstrated.

KURZFASSUNG

Der ständig andauernde technische Fortschritt führt im Bereich der Mikroströmung zu einer steigenden Nachfrage von Wärmetransportlösungen und Prozessoptimierungen, die zuverlässige Messmethoden für Temperatur und Strömungsfeld erfordern. Thermoliquid crystal (TLC)-Thermographie ist eine weithin akzeptierte und häufig verwendete Technik zur Messung von Temperaturfeldern in makroskopischen Strömungen. In Kombination mit optischer Geschwindigkeitsmesstechnik, wie Particle Image Velocimetry (PIV), kann gleichzeitig sowohl die Temperatur als auch die Strömungsgeschwindigkeit für makroskopische zweidimensionale (2D) Strömungsfelder bestimmt werden. Leider erlaubt der Stand der Technik aber nicht, dass diese Methode auf mikroskopische Strömungen übertragen werden kann. Niedrige Partikeldichte, Volumenbeleuchtung und die schlechte Qualität der TLC-Partikelbilder bei großen Vergrößerungen führen zu unüberwindbaren Herausforderungen bei der Anwendung auf dreidimensionale Strömungen mit mikroskopischen Dimensionen. In den folgenden Kapiteln wird eine Kombination verschiedener Neuentwicklungen vorgestellt, die sich genau diesen Herausforderungen stellt: Das 3D-Temperaturfeld sowie das Geschwindigkeitsfeld einer Mikroströmung sollen zeitaufgelöst vermessen werden, ohne auf Mehrkamerasysteme oder Lichtschnittverfahren aus der makroskopischen Strömungsmesstechnik zurückgreifen zu können. Dieses Ziel wurde in drei Phasen erreicht: 1. TLC Thermographie musste optimiert und angepasst werden, so dass die Temperatur der einzelnen Partikel ausgewertet und über die Zeit verfolgt werden konnte. Eine Lösung von TLC Mikro-Partikeln (mit einer engen Größenverteilung und ohne Verkapselung) wurde benutzt, um die Bildqualität der TLC Partikel zu verbessern. Durch eine mehrdimensionale Kalibrierung eines optimierten Parameterraums war es möglich, die Temperaturbestimmung aus der Farbinformation zu verbessern. 2. Astigmatismus Particle Tracking Velocimetry (APTV) wurde entwickelt, um die Partikel im Strömungsvolumen genau zu lokalisieren und deren Bewegung in drei Dimensionen (3D) zu folgen. 3. Das Signal-zu-Rausch-Verhältnis (SNR) der TLC-Partikelbilder musste soweit verbessert werden, dass es für defokussierende Methode, wie APTV, anwendbar ist, da sich die dritte Raumkoordinate in der Form der Partikelbilder verbirgt. Anstelle einer einzelnen konventionellen Hochleistungsblitzlampe wurden die Spektren verschiedener geregelter Lichtquellen über Lichtwellenleiter kombiniert. Mittels eines zirkularen Polarisationsfilters konnten die optischen Eigenschaften der chiralen nematischen Polymere ausgewertet werden. Diese Kombination machte es möglich, das Signal-zu-Rausch-Verhältnis gerade so weit zu steigern, dass die gleichzeitige Anwendung von TLC-Thermografie und APTV möglich war. Somit konnte schließlich ein Demonstrationsexperiment am Beispiel einer einfachen mikroskopischen Strömung durchgeführt werden. Die 3D-Verschiebung der TLC-Partikel wurde dabei gleichzeitig mit ihrer Temperatur verfolgt. Komplexere Anwendungen waren aufgrund der aktuellen technologischen Hardware-Einschränkungen noch nicht möglich. Dennoch konnten die Fähigkeit und das Potenzial der Messtechnik demonstriert werden.

1. Introduction

1.1. Purpose

Flow diagnostic experimental techniques have been the subject of extensive research for more than one hundred years. To this day, there exist well-established methods to reconstruct two-dimensional (2D) and three-dimensional (3D) velocity and temperature fields in macroscopic flows. When geometries and test sections shrink to microscopic dimensions, however, challenges arise that make the simultaneous velocity and temperature reconstruction of 2D and 3D flows a cumbersome task. The purpose of this research is to develop a reliable calibrated measurement method to simultaneously reconstruct the temperature and velocity fields of microscopic flows. A measurement approach that uses individual non-encapsulated thermochromic liquid crystal (TLC) micro particles was developed to track their temperature, as well as their 3D motion by means of Astigmatism Particle Tracking Velocimetry (APTV).

1.2. Motivation and Background

Heat transfer problems are commonplace in modern science and engineering and their solutions have led to a long list of technological developments, many of which have played a major role in transportation, communications, consumer electronics and personal computing, amongst many other areas that affect our lives and society. Today, with the strong downward trend in the size of electronic components down to micro and nano scales, combined with the upward trend in their heat tolerance demand, innovations in heat transfer solutions become more and more relevant. Experimental techniques used to solve heat transfer problems have played an essential role in understanding a myriad of the physical phenomena that occur in its many applications. A number of these applications involve fluids, which are naturally dynamic, whose constant transformation and motion can be used to optimize heat transfer processes. Therefore, the successful design and optimization of such heat transfer processes requires not only the precise reconstruction of the flow temperature, but also its velocity field.

1.2.1. Thermochromic Liquid Crystal (TLC) Thermography

A substantial amount of research has been carried out over the last century to develop experimental methods that can accomplish precisely these tasks in macroscopic flows. Point-wise measurements, such as hot- and cold-wire anemometry as well as mounted

thermocouples, continue to be used in the macroscopic domain to evaluate the flow temperature at individual points. However, their implementation in microscopic experimental arrangements is virtually impossible on top of the inconvenient truth of their being intrusive diagnostic techniques that alter the flow in question.

On the other hand, optical methods have also been the focus of a vast accumulation of research over many decades, yielding useful qualitative approaches such as flow visualization (Merzkirch 1987), as well as robust and precise non-intrusive methods that allow for instantaneous 2D measurements like surface temperature measurements with a pyrometer or an infrared (IR) digital camera (Michalski et al. 2001, Chung et al. 2003). Furthermore, the fast technological evolution of recent decades has brought along better and faster camera sensors, which combined with powerful light sources, gave birth to optical flow diagnostic techniques that are far better suited for microfluidics than intrusive point-wise approaches and provide instantaneous 2D and 3D characterizations of the flow. One common way to estimate temperatures by means of optical methods is the use of laser induced fluorescence (LIF) or luminescence. The physical principle is that the fluorescence intensity of a dye dissolved in the fluid changes as a function of temperature. In order to decrease the uncertainty due to illumination variations, ratiometric LIF uses the signals of two different dyes, where only one exhibits a temperature dependence (Coppeta & Rogers 1998, Sakakibara & Adrian 1999, 2004, Someya et al. 2005). The development of the LIF technique up to this point, however, relies on the use of a laser sheet that illuminates a planar section of the flow which is not trivial to produce in an experimental setup with microscopic dimensions. For this reason, micro optical flow diagnostic techniques use volume illumination which means that the measurement signal is integrated over the entire flow volume. In microfluidics, however, flow fields are most often fully three-dimensional and in many instances include strong gradients. Hence, a temperature measurement approach that does not integrate across the flow volume, such as the tracking of individual particles, is preferable. Someya et al. (2009) and Someya et al. (2011) used a high speed camera to measure the 2D velocity and temperature fields using particles, labeled with a temperature dependent luminophore, and evaluating their luminescence's lifetime. Only recently, Vogt & Stephan (2012) showed results of an experiment where particles were labeled with two dyes. They reported higher uncertainties compared to dissolved dyes but proved that the technique works using averages over interrogation windows. Nevertheless, two-dye particle labeling is not currently a common procedure, thus making the particles very expensive.

Another way to determine the temperature is to evaluate the Brownian motion of particles (Hohreiter et al. 2002). The major drawback of this method is that in order to be able to reliably measure Brownian motion, the particles have to be very small, thus substantially decreasing their signal. Furthermore, their size distribution must be very narrow and the viscosity of the fluid should not change if a consistent relationship between Brownian motion and temperature is to be established. On top of that, only time-averaged measurements are possible. Besides these techniques, liquid-crystal thermography has received great attention over the last several decades due to its capability to quickly re-

construct temperature fields in surfaces and flow planes/volumes. TLCs are substances whose molecular structure has both solid and liquid properties, hence the name liquid crystal, that change their color as a function of temperature (Fergason 1966, Adams et al. 1969, Parsley 1991, Oswald & Pieranski 2005, Sage 2011). Their use as a thermal diagnostic tool is commonplace in the heat transfer and fluid dynamics research communities. Today, TLCs have a broad range of applications including flow visualization (Smith et al. 2001, Dabiri & Gharib 1991), microfluidics thermal mapping (Chaudhari et al. 1998), heat transfer design for electronic components (Farina 1995, Azar & Farina 1997), and medical applications (Stasiek et al. 2006, Bharara et al. 2008), among others. An extensive account of most, if not all, of the research in the field of TLC thermography has been reported in a number of review articles over the last two decades (Baughn 1995, Roberts & East 1996, Wozniak et al. 1996, Behle et al. 1996, Stasiek 1997, Stasiek & Kowalewski 2002, Stasiek et al. 2006, Dabiri 2009, Nasarek 2010, Abdullah et al. 2010, Sage 2011). They thoroughly describe and discuss most of the available literature, dating back to the 1800's, on several subjects that concern this technique such as the motivations for its development, properties of TLCs, colorimetry, imaging, commercial availability, time response, calibration, uncertainty analysis, hysteresis, and applications, among others. Several studies have been performed using TLCs in thin films that are applied to surfaces to measure their temperature (Akino et al. 1989, Farina 1995, Sabatino et al. 2000) and the concept has even been extended to the microscopic domain with the aim of measuring two-dimensional temperature fields or point-wise average heat transfer coefficients in the walls of micro tubes and channels (Höhmann & Stephan 2002, Muwanga & Hassan 2006b,a, 2007, Chin et al. 2002). All the experimental results reported in the aforementioned literature were obtained by illuminating the TLC material with high-power flash lamps. Table 1 of Dabiri's (2009) review specifically lists the illumination source types used in most of these experiments. Unfortunately, the light spectrum generated by the light bulbs or tubes in such flash-lamps is far from uniform and displays one or a few narrow peaks in the visible spectrum. This means that some bands of visible wavelengths will be scattered with substantially less intensity than other bands, hence making the detected color patterns weaker.

Over the years, many calibration methods have been engineered to extract the temperature from the color of TLCs. Section 4 of Behle et al.'s (1996) and Smith et al.'s (2001) articles, Section 5 of Dabiri's (2009) review, and Section 3 of Abdullah et al.'s (2010) report provide a thorough account of the various attempts to perform this task over the last two decades. Rao & Zang (2010), Bednarz et al. (2010), Cukurel et al. (2012), and Segura et al. (2013) are some of the latest reports of novel techniques and ideas on this topic that are not covered in the earlier reviews. The general tendency over the last decades has been to use the temperature-hue relationship of TLCs to calibrate the digital images, where hue is a parameter, derived from the Red, Blue and Green (RGB) signals of the color camera's digital sensors, that represents a color shade and will be defined in more detail in Chapter 2.2. On the other hand, multi-variable calibration approaches using the color images' hue (H), saturation (S), and intensity (I) have also been studied, since the

S and I signals also contain valuable information that plays a substantial role in relating the TLCs' temperature to the color of their digital images (Fujisawa & Hashizume 2001, Segura et al. 2013). Fujisawa & Hashizume (2001) performed a study of synthetic data, using a multi-variable calibration approach, and reported uncertainty values of 0.06 K in a range of 2.3 K (2.6 %) for two-dimensional interrogation windows. Fujisawa et al. (2005) later reported uncertainty values of 0.13 K, using a stereoscopic setup, on TLCs with a temperature response range of 2.3 K (5.7 %), using a similar approach. It should be noted, however, that even though the HSI color space has been the transformation of choice for most research groups using this measurement technique, it is not the only means of interpreting color of digital images in order to extract their temperature information. Roesgen & Totaro (2002) proposed a statistical calibration approach that uses proper orthogonal decomposition (POD) to transform the raw RGB digital image data into a fully decorrelated variable space with the potential of providing a steeper calibration curve that yields a lower uncertainty for a one- or two-variable calibration.

1.2.2. TLC Thermography Combined With Particle Image Velocimetry (PIV)

The principle of the technique has also been combined with Particle Image Velocimetry (PIV) to simultaneously measure temperature and velocity fields (Dabiri & Gharib 1991, Nasarek 2010) in two dimensions. PIV is a measurement technique used to reconstruct instantaneous 2D velocity flow fields (Raffel et al. 2007). In very simple terms, it works by seeding the flow with tracer particles, illuminating a planar region of it, recording digital image pairs of the illuminated tracers (separated by a known time delay), and cross-correlating them to get a grid of velocity vectors that represent the mean velocity over the corresponding flow sections. Since Santiago et al.'s (1998) introduction of a PIV system for microfluidics, this method has become a major flow diagnostics tool for microfluidic devices used in a myriad of science and engineering applications. For a comprehensive explanation and discussion of μPIV and is applications, the reader its referred to the most recent reviews on this measurement technique (Lindken et al. 2009, Lee & Kim 2009, Wereley & Meinhart 2010, Williams et al. 2010).

Several researchers have used the combination of TLC thermography and PIV over the last two decades and their contributions are summarized and tabulated in Table 1 of Dabiri's (2009) review and Tables 2.1 and 2.2 of Nasarek's (2010) dissertation. Today, the technique continues to evolve into better and more efficient temperature and velocity measurement methods. It is worth noting that in order to simultaneously measure the flow temperature and velocity, researchers have seeded the flow with solutions containing microencapsulated TLC material, as well as other tracer particles that are better suited for PIV cross-correlation, due to the low image quality of the TLC particles. Up to this day, all of the reports on this flow diagnostics technique are based on acquiring color images of flows, with high concentrations of TLC material, and reconstructing planar temperature fields. Extensions of this principle like scanning methods (Fujisawa & Funatani 2000, Fu-

jisawa et al. 2005, Lutjen et al. 2001), stereoscopic (Funatani & Fujisawa 2002, Fujisawa et al. 2004, 2005), and tomographic arrangements (Mishra et al. 2000, Ciofalo et al. 2003) have also been used to reconstruct average 3D temperature and velocity flow fields. All of these measurements rely on the concept of breaking the color images into sections and evaluating the mean temperature of the flow in each section. Even though sophisticated methods have been successfully employed to extract the mean temperature of the flow by evaluating these so-called interrogation windows, the resolution of such measurements is limited by the size of the windows and the reconstruction of temperature gradients is necessarily biased when using this approach. Furthermore, when the flow volumes are reduced to microscopic dimensions, the measurement paradigm changes and, for one, the use of a light sheet is not possible thus introducing another bias in the measurement of flows that contain a temperature gradient in the depth direction. Secondary flows, commonly encountered in micro channel geometries, possess flow features that are completely hidden to two-dimensional measurements with volume illumination (Rossi et al. 2011). On the other hand, as explained in Cierpka & Kähler (2012)'s review, seeding concentration tends to be lower in microfluidics experiments and correlation methods become less reliable while the individual tracking of particles would be a convenient solution to avoid bias errors. Moreover, if the TLC particles would have a narrow size distribution and produce a high signal-to-noise (SNR) ratio, defocusing methods, such as astigmatism particle tracking velocimetry (APTV) could be used to track their motion in three dimensions as well as their temperature (Cierpka et al. 2010, 2011a). To this day, however, the application of TLC thermography, combined with particle velocimetry, to three-dimensional micro flows presents currently unsurpassed challenges caused by sparse seeding density, volume illumination, and low particle image quality at high magnifications. Even though Park et al. (2001) also used the average temperature over sections to reconstruct the flow's two-dimensional temperature field, they reported uncertainty figures for the temperature estimation of individual particles ranging from around 5 % to 20 % over a temperature span of 2.5 K using a neural network calibration approach. They used micro-encapsulated TLCs manufactured by Hallcrest (BM40C26W20) with a useful temperature response range approximately between 26 and 29 °C. Due to the high uncertainty in the temperature measurement of individual particles, they calculated the mean temperature over interrogation windows of 32×32 pixel and obtained lower error values of $2-8$ %. This reduction in uncertainty, however, comes at the expense of a lower spatial resolution due to the averaging over interrogation windows. Basson & Pottebaum (2012), recently reported temperature measurements in a micro channel using individual encapsulated TLC particles. They demonstrate interesting advantages provided by an innovative circularly polarized illumination system on micro-encapsulated TLCs also manufactured by Hallcrest (NSL33R35C5 W), yielding average uncertainties of 1.2 K over a temperature range between 36.3 and 43.7 °C (16 %). These uncertainty levels remain too high for a reliable temperature field reconstruction but can be brought down by improving the images of the TLC particles.

1.3. Approach

An experimental method, comprised of a combination of cutting edge technology, is presented to generate high quality color images of non-encapsulated TLCs, which allow for their individual tracking in order to perform time-resolved measurements of 3D temperature and velocity fields in microscopic flows where multi-camera methods and light sheets are not an option.

An emulsion of TLC micro spheres without encapsulation was manufactured by Shirasu Porous Glass (SPG) membrane emulsification, a technique that allows for the production of particles with narrow size distributions (Joscelyne & Trägårdh 2000). Additionally, a state-of-the-art white light source, which provides a more homogeneous illumination spectrum than those produced by high power flash lamps, was used in combination with a circular polarization filter that exploits the optical properties of chiral nematic polymers, to boost the SNR of the particle images. This increment in SNR not only enhances the temperature estimation of the TLC particles from their color but also allows for the implementation of defocusing methods to encode the depth position of the particles in the geometry of their images.

Astigmatism Particle Tracking Velocimetry (APTV), is such a defocusing technique where the optical symmetry of the imaging system is broken with a cylindrical lens, and particles are projected as ellipses on the camera sensor, allowing for an unambiguous determination of their depth position in the flow volume from the shape of their elliptical images. The main reason this technique was developed over the last five years is its ease of implementation to microfluidics experiments with a single optical access to the flow.

A multi-variable calibration approach was also developed, which makes use of all three RGB color components to compute an optimally decorrelated variable space that can be used to find a robust calibration function to extract temperature information from the particle images' color, as opposed to the commonly used Hue-Temperature relationship.

Finally, the TLC thermography method was combined with APTV and a proof-of-concept experiment was performed, where the displacement of TLC particles is tracked in 3D while their temperature is also being measured. More complex applications were not possible due to current technological hardware limitations but the capability and potential of the measurement technique is clearly demonstrated.

2. Fundamentals

2.1. Thermochromic Liquid Crystals (TLCs)

Thermocromic liquid crystals (TLCs) are fluids that reflect different colors as a function of their temperature. They belong to a more general material class, referred to, by Brostow (1990) and Mitchell (2004), as liquid crystal (LC) polymers that are neither completely liquids nor solids. Instead, these polymers exist in an intermediate material phase in which they can flow but also exhibit long-range order interactions between molecules as well as crystalline structures. This state provides a convenient combination of physical properties where the material mechanically behaves like a liquid but exhibits the optical characteristics of a crystal. LCs consist of cigar-shaped molecules and exist in different phases, reviewed and explained in detail by Fergason (1964) and Brostow (1990), with particular molecular arrangements.

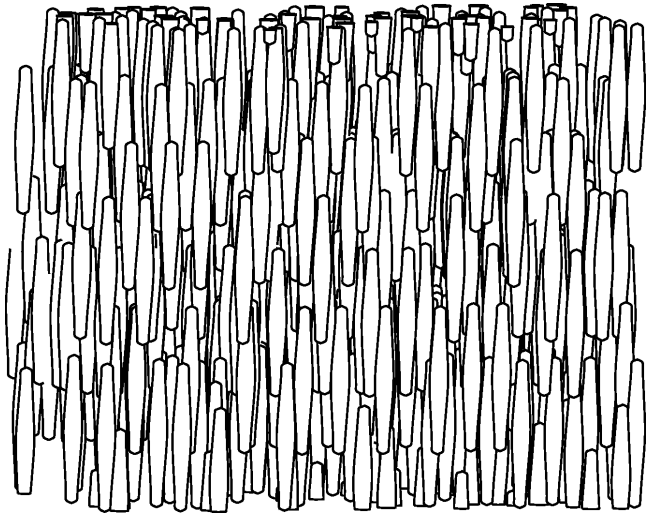

Figure 2.1.: Liquid crystals in their nematic phase. The molecules float freely, with their long axes parallel to each other, with no apparent order or layering scheme.

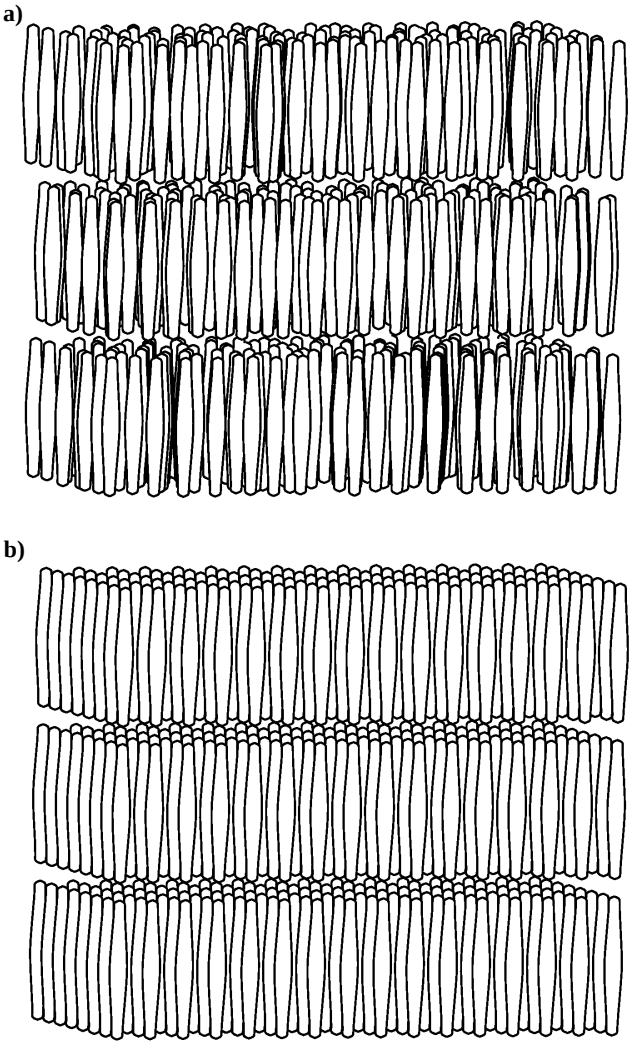

Figure 2.2.: Liquid crystals in their smectic phase. a) A case where the molecules in the layers are randomly distributed. b) A different case where the molecules in the layers are aligned in rows.

All phases of LCs have in common that their molecules are almost parallel to each other. The average orientation of the molecules' long axes is known as the 'director', which is responsible for their anisotropic behavior. By anisotropic it is meant that the index of refraction of LCs, as well as their dielectric constant, is not constant and varies as a function of the polarization orientation and propagation direction of the light that travels through them. The 'nematic' phase of LCs happens when the only long-range order exhibited by the material is the alignment of molecules with the director. In other words, nematic LCs consist of free floating molecules whose long axes are parallel to each other as shown in Figure 2.1. The 'smectic' phase exhibits additional degrees of long-range order. Molecules in smectic LCs, aside from being aligned to a director, have their centers fixed in equidistant planes, forming planar layers as shown in Figure 2.2a. Moreover, the smectic phase can have further degrees of long-range order where the molecules lie in organized two-dimensional lattices (Figure 2.2b) or the layers are not perpendicular to the director. The third phase, in which TLCs exist, is called 'cholesteric' or 'chiral nematic'. Its name accounts for the fact that it possesses a molecular structure commonly found in materials that contain cholesterol. Molecules in cholesteric LCs, like those in smectic LCs, are arranged in layers with their long axes aligned parallel to each other. In the cholesteric phase, however, the layers are parallel to the director which rotates from layer to layer by approximately 15 arc-minutes causing a continuous rotation of the molecules along a helical path, as schematically shown in Figure 2.3 (Fergason 1964). The meticulously ordered molecular structure of cholesteric LCs grants them unique optical properties, tabulated and thoroughly discussed by Fergason (1966), Parsley (1991) and Sage (2011). The relevant characteristics, mainly responsible for their visible change in color as a function of temperature, are summarized as follows:

- Cholesteric LCs are birefringent materials, meaning that their index of refraction changes as a function of polarization orientation and propagation direction. Furthermore, unlike nematic and smectic LCs, they are optically negative; linearly polarized light that travels through cholesteric LCs experiences an index of refraction, n, in the range between n_{min} and n_{max} which correspond to the cases when polarization orientation is perpendicular and parallel to the director, respectively.

- As explained by Fergason (1964), cholesteric LCs are extremely optically active materials that rotate the polarization plane of incident linearly polarized light at a rate as high as $18,000\,^{\circ}$ per millimeter.

- Cholesteric LCs are circularly dichroic and selectively reflect circularly polarized light whose polarization chirality matches that of the LCs director's rotation (de Vries 1951). The reflected circularly polarized light is a product of constructive interference between reflected light waves from different molecular layers, analogous to Bragg reflections inside a solid crystal (Cowley 1995, Myers 2009). This

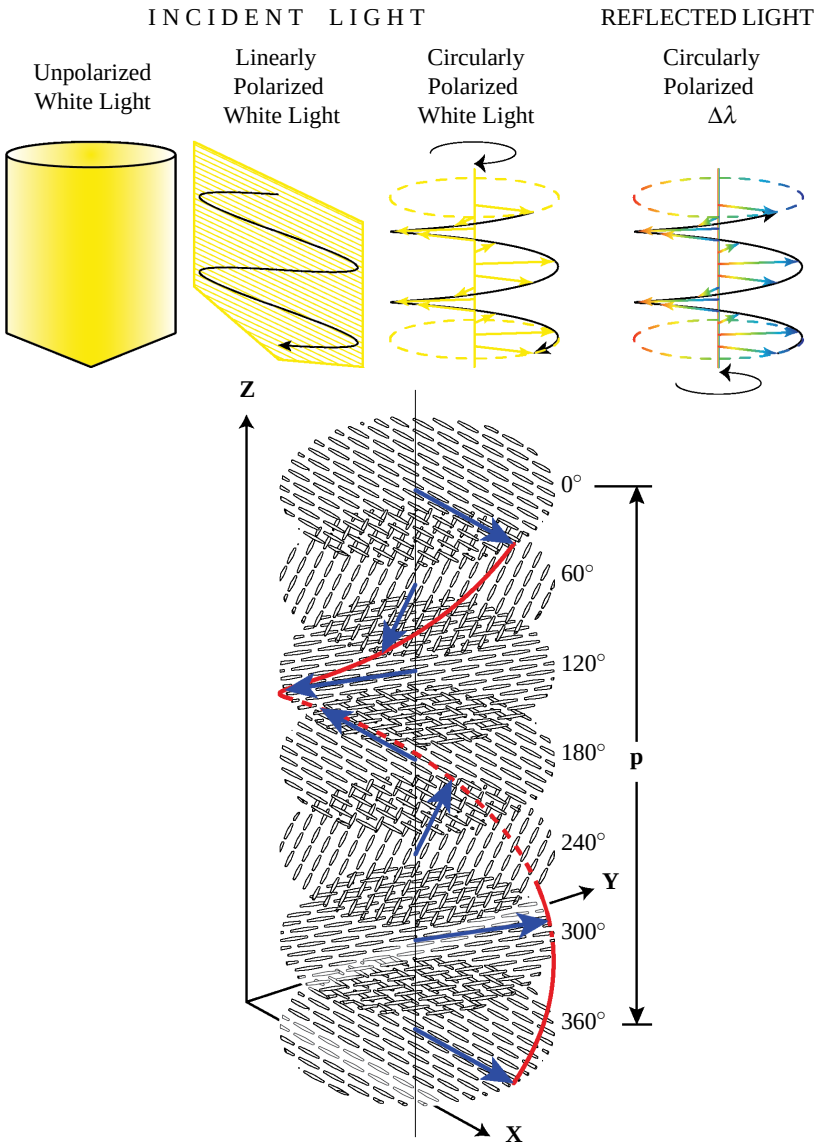

Figure 2.3.: Liquid crystals in their cholesteric phase. The molecules are arranged in layers with their long axes aligned parallel to each other. The director of the layers rotates from one layer to the next causing a continuous rotation of the molecules along a helical path.

reflected light exhibits a maximum intensity at a specific wavelength (de Vries 1951),

$$\lambda_{\max} = p\frac{n_{\min} + n_{\max}}{2} \tag{2.1}$$

that is also the center of the narrow reflection bandwidth (Fergason 1966),

$$\delta\lambda = p(n_{\min} - n_{\max}) \tag{2.2}$$

where p, defined by de Vries (1951) as the pitch, is the distance required for the director of molecular layers to rotate 360 °.

- As explained by de Vries (1951) (note that he uses a stationary coordinate system when evaluating rotation chirality), type 'dextro' materials, as are TLCs, do not invert the chirality of circularly polarized light upon reflection from molecular layers. This is due to the fact that when polarized light travels from one layer to the next, the angle between its polarization plane and the director of the layer changes. This relative rotation causes one orthogonal component of the electric vector to experience a higher index of refraction while the other orthogonal component necessarily experiences a lower one. Consequently, only one of these components will experience a phase shift, thus inverting the reflected light's circular polarization chirality, which is normally opposite to that of the incident wave.

- The pitch, p, of TLCs exhibits an inversely proportional relationship to temperature. Ergo, as temperature rises the reflected wavelength band, $\delta\lambda$, shifts to shorter wavelengths and the TLCs appear to gradually change colors across the visible spectrum from red to blue.

The different material phases of LCs have been a common subject of research over the last century and there are a myriad of scientific reports on their molecular characteristics and properties. Several models, outside the scope of this study, have been proposed to quantify their optical behavior as well as experimental data to validate them. For further information, the reader is referred to previous reports on this matter (Oseen 1933, de Vries 1951, Fergason 1966, Adams et al. 1969, Berreman & Scheffer 1970c,a,b, Melamed & Rubin 1971, Dreher & Meier 1971, 1973, Gleeson & Coles 1989, Zink & van Dael 1993, Abbate et al. 2007, Chen & Yeh 2012).

2.2. Colorimetry in digital photography of TLCs

TLCs reflect selective wavelength ranges as a function of their temperature, which makes them a potentially useful instrument to measure the temperature of their surrounding medium, granted that a reliable relationship can be established between their color and

their temperature. This invites the question of how color is measured and/or interpreted, which is addressed thoroughly in the colorimetry (science of color) literature. Newton was the first to break white light into its colored components using a prism, which led to the understanding, years later, that colors correspond to different wavelengths of electromagnetic radiation. In 1802, Young stated, in the third hypothesis of his lecture on the theory of light and colors, that "the sensation of different colours depends on the different frequency of vibrations, excited by light in the retina", and proposes that the retina can separately detect intensities of three principal wavelength bands which, compounded, produce the human interpretation of color. However, it should be noted that this was merely a suggestion, without physiological evidence, and was not experimentally shown until the 1960s, when Brown & Wald (1964) and Wald (1964) presented evidence of the three types of cone photodetector cells present in human eyes, along with their respective sensitivities in the red, green and blue spectral ranges (Brown & Wald 1964, Wald 1964). In 1855, Maxwell was the first to report an experimental qualitative method for creating any variety of visible color by combining colored light of three primary colors. This procedure was then quantified in the late 1920s (Wright 1929b,a, Guild 1931), and resulted in the RGB and XYZ mathematical colorimetric standards of the Commission International de l'Éclairage (CIE) of 1931 (Smith & Guild 1931, Fairman et al. 1997, Brill 1998). These international standards define specific parameters of observation, illumination and viewing conditions, evaluation of brightness, and a trichromatic system to measure the expression of color, such that any light signal (of an arbitrary color) can be comprehensively interpreted as a function of the superposition of three primary color intensities. The theoretical derivations of the 1931 CIE colorimetric standards are beyond the scope of this study. This three-dimensional interpretation of color, however, became the platform for the revolution that has taken place in color digital photography and cinematography during the last decades.

The basis of the trichromatic color matching theory used in digital photography is a subtractive system where light is filtered with different wavelength bands to reconstruct a certain recorded color. The imaging process of a color digital camera begins with light being focused on to a charge-coupled device (CCD) array sensor. Since the CCD sensor is monochromatic and cannot tell the difference between a green photon and a red one, the CCD array must be segregated with color filters in order for it to gather the necessary information to reproduce color. There are two main ways of achieving this task. The first is the placement of color filter arrays on individual CCD sensors, known as Bayer Mosaic sensors, so that adjacent pixels are exposed to red, green and blue light, exclusively, and the trichromatic data required for the color reconstruction is recorded. The second is the placement of a prism system, such that white light travels through a red, a green and a blue filter, and is focused on three CCD sensors, carrying the individual color information to each, known as 3CCD cameras. The latter has a better resolution, since all the color information is available for every single pixel of the sensors. For the purposes of this study, a 3CCD color camera is used to acquire all color digital images. Therefore, each recorded color image, is composed of three data matrices, containing its red, green, and

blue (RGB) monochromatic intensities. These data must then be interpreted to establish a reversible relationship with the TLCs' variations of temperature.

The first sensible approach would be to fit a mathematical function to the RGB data of TLC images at different temperatures. This would be done with the intention of establishing a reversible relationship between RGB values and temperature, in order to be able to extract the latter from the former.

As the temperature of TLCs varies and their color changes from red to blue, the individual R, G, and B intensities exhibit trends which have been used to directly calibrate the temperature response of TLC thin sheets in surface coatings (Vejrazka & Marty 2007). However, these values are all directly affected by the light-source's intensity and orientation, digital camera settings, optical arrangements, etc., and do not necessarily respond to variations of these experimental factors in the same manner, thus making them very susceptible to bias errors in the temperature calibration.

An alternative to directly using the R, G, and B components of color is to use the H, S, and I (HSI) color space. This is an alternative perspective of color perception that uses relationships between R, G, and B instead of their raw values.

- H describes the shade of a particular color; conventional color names like yellow, orange, etc. are examples of hue.
- S quantifies the degree of purity of the color, also described as the extent to which the color is diluted with white.
- I relates to the chromatic-independent brightness of the color.

There have been several formulations to the transformation from RGB to HSI color space (Russ 2002, Hay & Hollingsworth 1996, 1998, Pratt 2007). For the purposes of this study, a simplified version of Hay & Hollingsworth (1996)'s formulation will be used, employed by the 'rgb2hsv' function of the MATLAB software package where,

$$\begin{aligned} I &= \max(R,G,B) \\ S &= I - \min(R,G,B)/I \\ H &= \frac{1}{6}\left\{ \begin{array}{ccc} (G-B)I/S & | & R>B,G \\ 2+(B-R)I/S & | & G>R,B \\ 4+(R-G)I/S & | & B>R,G \end{array} \right\} \end{aligned} \tag{2.3}$$

This transformation provides non-dimensonal HSI values, where H is a simplified approximation of Hay & Hollingsworth's (1996) formulation, normalized with 2π, and I is normalized with the maximum pixel count for an individual sensor of the digital camera (255 for 8-bit camera sensors).

The reader should note that the HSI color space is a non-reversible mathematical transformation of the raw images' RGB data. In the introduction of this transformation approach, Joblove & Greenberg (1978) states that most viewers notice a color's hue before they notice other characteristics so this convention arose as a convenient system for the specification of colors based on more humanly intuitive quantities than red, green and blue levels. Nevertheless, it is not the only way to interpret color and a more precise transformation may exist that is better suited for temperature estimation from the color of TLCs. Roesgen & Totaro (2002), for instance, introduced a statistical calibration approach that uses proper orthogonal decomposition (POD) to transform the raw RGB digital image data into a fully decorrelated variable space with the potential of providing a steeper calibration curve that yields a lower uncertainty. They used normalized RGB values

$$\begin{aligned} r &= R/(R+G+B) \\ g &= G/(R+G+B) \\ b &= B/(R+G+B) \end{aligned} \tag{2.4}$$

to calculate the covariance matrix

$$\begin{aligned} C &= Cov(r,g,b) \\ &= \begin{pmatrix} \overline{(r-\overline{r})^2} & \overline{(r-\overline{r})(g-\overline{g})} & \overline{(r-\overline{r})(b-\overline{b})} \\ \overline{(r-\overline{r})(g-\overline{g})} & \overline{(g-\overline{g})^2} & \overline{(g-\overline{g})(b-\overline{b})} \\ \overline{(r-\overline{r})(b-\overline{b})} & \overline{(g-\overline{g})(b-\overline{b})} & \overline{(b-\overline{b})^2} \end{pmatrix} \end{aligned} \tag{2.5}$$

where $\overline{x} = \frac{1}{n}\sum_{i=1}^{n} x_i$. The POD is then a linear transformation expressed as,

$$\begin{pmatrix} x_1 \\ x_2 \\ x_3 \end{pmatrix} = \underline{\underline{T}} \begin{pmatrix} (r-\overline{r}) \\ (g-\overline{g}) \\ (b-\overline{b}) \end{pmatrix} \tag{2.6}$$

where $\underline{\underline{T}}$ is a rotation matrix such that $\underline{\underline{T}}^{-1} = \underline{\underline{T}}^{t}$, composed of the eigenvectors, arranged in rows below each other, of the eigenvalue problem

$$C\overrightarrow{t} = \lambda\overrightarrow{t}. \tag{2.7}$$

The x_1 and x_2 components, associated with the direction of the non-zero eigenvalues λ_1 and λ_2 carry all the color information while the third component, associated with the direction of the lowest eigenvalue $\lambda_3 = 0$, vanishes due to the raw data normalization ($r+g+b=1$).

3. Experimental Setup

3.1. Dispersion of Non-Encapsulated TLC particles

A major factor behind the high uncertainty of temperature measurements in individual TLC particles, such as those reported by Park et al. (2001) and Basson & Pottebaum (2012), is the fact that the polymer shell around the TLC material causes aberrations and distorts the detected color of each particle creating a substantial bias error in the evaluation of color, especially for high magnification images. Additionally, the encapsulation process may also alter the molecular structure of the TLC material causing each particle to react differently to temperature changes. Parsley (1991) states, in Hallcrest's TLC handbook, that raw TLC materials need to be protected and stabilized in order to be successfully used for commercial applications due to their susceptibility to degradation from UV light and certain organic chemicals. This is why small droplets of TLC material are surrounded by a polymer coating, or microencapsulated, in order to shield them from the atmosphere. Section 2.3 of the TLC handbook discusses different types of microencapsulation and provides the reader with further information and literature regarding this matter. Figure 3.1 shows an example of what a particle from a sample of Hallcrest encapsulated TLCs (NSL40/R25C5W) looks like over its useful temperature range. Even though the color variation with temperature is clearly visible, the particle image displays a very strong outer ring that occurs due to the strong reflection of light from the encapsulating material, which produces errors that affect the evaluation process. Furthermore, complex structures inside the particle are evident, which vary from particle to particle. This is why the successful temperature tracking of individual TLC particles requires several improvements to the current state-of-the-art TLC thermography technique. First of all, the quality of the particle images must be considerably better than that of encapsulated TLC particles. Second, a preprocessing algorithm that works consistently for the varying color intensity profiles that correspond to different temperatures is necessary to reliably detect all particles in the temperature range. And third, a reliable relationship between the color of each particle and its temperature must be established.

Since encapsulated TLC particles are clearly not a viable option for individual temperature tracking, non-encapsulated material was used. Thermography using non-encapsulated TLC material has been investigated to a limited extent for two-dimensional or point-wise temperature measurements (Muwanga & Hassan 2006b,a, 2007) but no attempts to fabricate stable TLC droplets for particle tracking have been made so far. The TLC particles used in this study were produced at the Institute of Pharmaceutical Technology of the

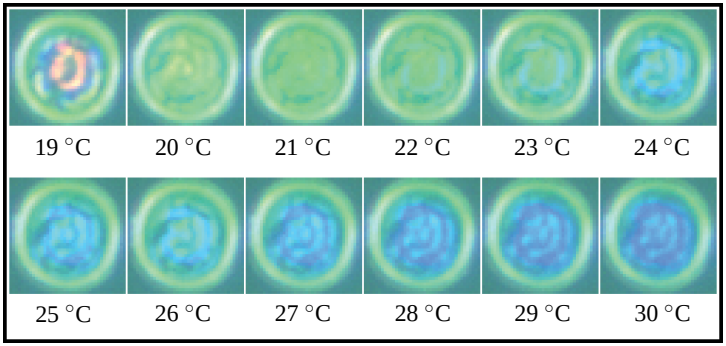

Figure 3.1.: Color images of encapsulated TLC particles (Hallcrest NSL40/R25C5W) over their color response temperature range (20x magnification, illuminated with a HXP 120 W flash lamp).

Braunschweig University of Technology using a direct SPG membrane emulsification process as described in detail by Nakashima et al. (1992). Four TLC bulk materials were studied (fabricated by Hallcrest Inc.): R20C1W, R20C5W, R20C10W, R20C20W, with temperature color response ranges of 1 K, 5 K, 10 K, 20 K, respectively. All four TLC materials, with a red-start temperature of 20 °C, were briefly heated to 55 °*C*, beyond their melting point of $45 - 47$ °*C*, and placed in a 10 ml custom built, double walled, temperature controlled, pressurized, stainless steel, external pressure micro kit type vessel manufactured by MCTech Co. The device was equipped with a Haake D1 water bath, manufactured by Thermo Haake GmbH, used for tempering the lipid phase of the material. A pressure of $25 - 35$ kPa was applied to force the lipid phase through a pre-wetted hydrophilic SPG membrane with a pore size of 5.5 μm, fabricated by SPG technology Co., into 80 ml of 5% poloxamer 188 emulsifier (aqueous phase) with 0.01% thiomersal as preservative. The solution was continually stirred with a temperature controlled magnetic stirrer (IKA-Werke GmbH) at 300 rpm. Evaporated water was replenished every 12 hours during the 48 hours of preparation. After the direct emulsification process, the solution container was dipped into ice-water for at least 20 minutes, giving birth to the TLC particles that would be used for the temperature tracking experiments, which take form when the emulsion droplets are cooled below the liquid crystal phase transition temperature. All samples were stored at room temperature ($18 - 20$ °C). A direct comparison of the resulting non-encapsulated particles' raw color appearance with their encapsulated counterpart is displayed in Figures 3.1 and 3.2 (illuminated with a HXP 120 W flash lamp). The non-encapsulated TLC particles display a much more homogeneous color profile and, even though the raw images' contrast is low at higher temperatures. This lack of contrast occurs due to the inhomogeneous light spectrum generated by the high-power flash lamp.

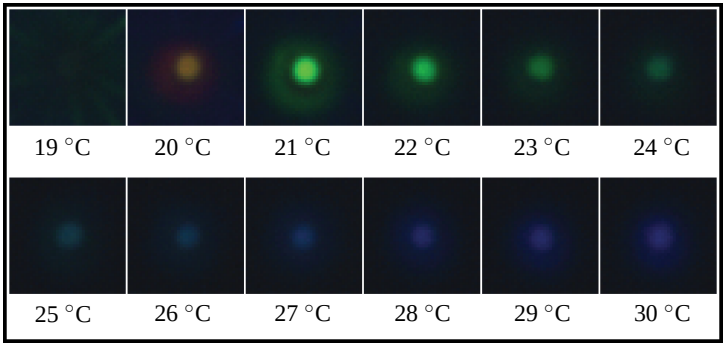

Figure 3.2.: Color images of non-encapsulated TLC particles (Hallcrest R20C5W) over their color response temperature range (20x magnification, illuminated with a HXP 120 W flash lamp).

A laser diffractometer with polarization intensity differential technology (model LS 12 320 by Beckman-Coulter) was used to estimate the particle size distribution of the dispersion. Three measurements were performed at the Institute of Pharmaceutical Technology of the Braunschweig University of Technology to calculate the volume distributions assuming an index of refraction of 1.46 for the TLC particles, 1.33 for the aqueous dispersion medium, and 0.01 for the imaginary part of the refractive index. The estimated particle size distribution for the non-encapsulated TLC particles is plotted in Figure 3.3 along with that of micro encapsulated TLC particles from Hallcrest (NSL40/R25C5W). Both sets display multi-modal distributions but the dominant diameter ($\sim 16\ \mu$m) of the non-encapsulated particles represents a higher relative volume, with a narrower distribution than that of their larger encapsulated counterpart ($\sim 16\ \mu$m). Furthermore, no higher diameter particles were detected in the non-encapsulated sample and the $\sim 1\ \mu$m portion is not discretely discernable with the optical system used for the temperature tracking experiments.

3.2. Light Source and Circular Polarization Filtering

The majority of the TLC thermography experiments reported in the literature mention the use of white light flash lamps to illuminate the TLC material, be it sprayed layers or encapsulated particles. As can be seen in Table 1 of Dabiri's (2009) review, the illumination sources range from halogen to high-power Xenon, metal halide, and mercury lamps. Different flash lamps shine different light spectrums but all of them have deficiencies in certain wavelength bands of the visible spectrum and peaks in other bands. This causes a lack of contrast for some colors and an excess of it for others, as can be seen in Fig-

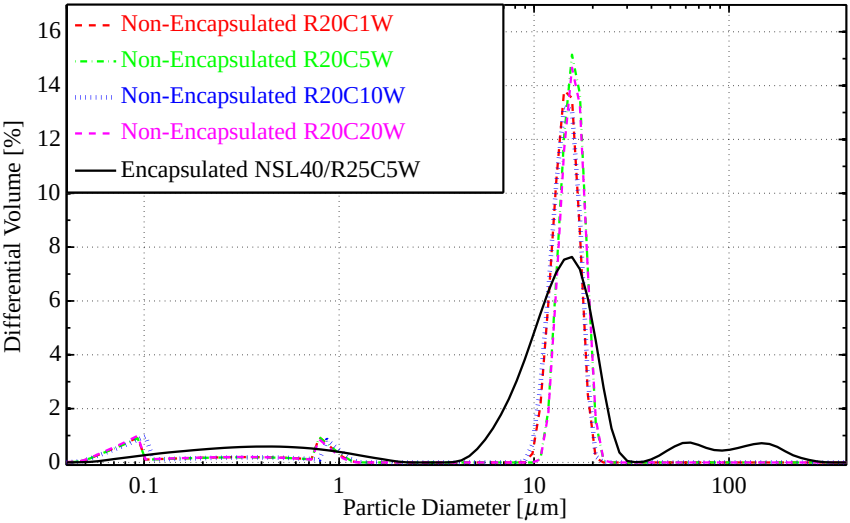

Figure 3.3.: Size distribution of custom made non-encapsulated TLC particles along with that of commercially available encapsulated TLC particles from Hallcrest (NSL40/R25C5W).

ure 3.2. The spectrum generated by the HXP 120 W flash lamp, used to illuminate the TLC particles in Figures 3.1 and 3.2, is plotted in Figure 3.4 (measured with a Laser 2000 BlueWave STE-BW-UVN spectrometer). The spectrum for this particular light displays two narrow peaks in the green band but the blue and red intensities are very low in comparison. Thus, it becomes clear from this plot why the contrast of the TLC particle color image is so vibrant when the particle reflects green light but so weak in the red and blue regions. This is why a different illumination source was used.

A Lumencor Spectra X is a so-called light engine that combines the illumination of six light pipes which shine specific wavelength bands of the visible spectrum. The light pipes are individually adjusted and can be normalized to produce a more homogeneous spectrum. The illumination spectrum used for the experiments in this study is also plotted in Figure 3.4 (measured with a Laser 2000 BlueWave STE-BW-UVN spectrometer) and the TLC particle color images, illuminated with the Spectra X light engine are shown in Figure 3.5. It is evident from Figure 3.5, even for the naked eye, how the color signal of the TLC particles is much better acquired when they are illuminated with a balanced light source. However, when the particles heat up, a halo appears around the blue particle images (probably because they are approaching the temperature where they leave their chiral nematic phase), which makes the color detection of their blue cores less accurate.

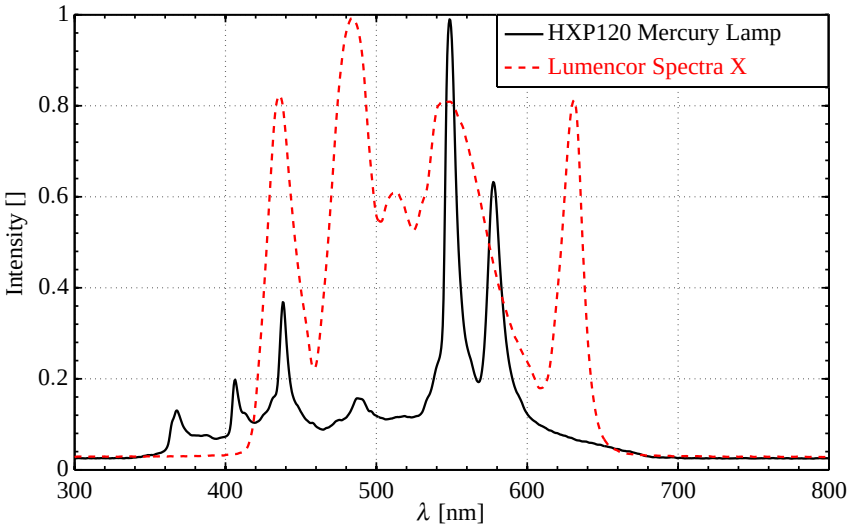

Figure 3.4.: Light spectra of HXP 120 W Mercury flash lamp and Lumencor Spectra X light engine.

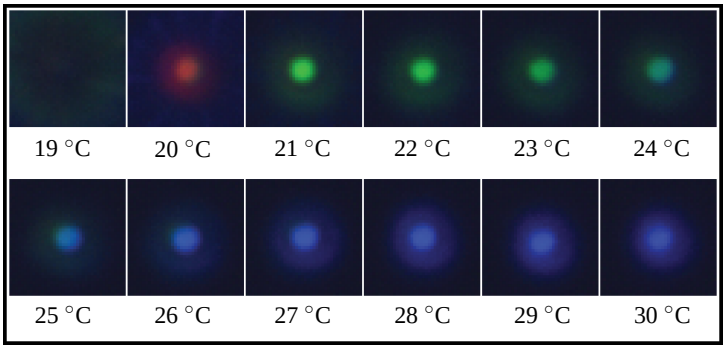

Figure 3.5.: Color images of non-encapsulated TLC particles (Hallcrest R20C5W) over their color response temperature range (20x magnification, illuminated with a Lumencor Spectra X light engine.)

In order to obtain higher quality particle images across the temperature response range of the TLC material, the method proposed by Basson & Pottebaum (2012) was used to remove background noise, as well as unwanted reflections and halos that may surround the TLC particle color-reflecting cores. Since the narrow wavelength bands that TLCs reflect are always circularly polarized with the same polarization chirality, a circular polarization filter can be introduced in the optical system such that only the circularly polarized light scattered by the TLC color particles is transmitted to the camera sensor. This circular polarization filter consists of a linear glass polarizer (Edmund Optics NT47-216), with an extinction ratio of $10^4 : 1$ and a wavelength range of $400 - 700$ nm, used to transmit a single polarization plane of the white light that shines from the light source, combined with an achromatic quarter wave plate (CVI Melles Griot ACWP-400-700-06-4), which is a birefringent crystal through which the speed of light varies as a function of its electric field's orientation.

Figure 3.6 shows a schematic illustration of the operating principle of the circular polarizer. What happens is that the unpolarized white light from the light source becomes linearly polarized after passing through the linear polarizer. Next, assuming that the axis of the linear polarizer is aligned at $45\,^\circ$ from the fast axis of the quarter wave plate, circularly polarized white light will be transmitted to the TLC particle seeded flow. Note that the circular polarization chirality of the transmitted light can be inverted by adjusting the alignment of the quarter wave plate, with respect to the linear polarizer, by $90\,^\circ$. Now, once the circular polarization of the light illuminating the TLC particles matches the rotation of their molecular layers, the narrow wavelength bands reflected by the particle cores, will be transmitted back through the circular polarization filter, while all other light will be blocked by it. This happens because the TLC particles will always reflect circularly polarized light with the same polarization chirality, regardless of the illumination's polarization. On the other hand, other reflections caused by index of refraction gradients or hard boundaries, such as those arising from the glass plate, the surface of the particles, walls or corners of microchip geometries, etc. will scatter light with an inverted circular polarization chirality. This light will be transmitted as linearly polarized light by the quarter wave plate, with a linear polarization perpendicular to the axis of the linear polarizer, which will not be transmitted further to the camera sensor.

Unfortunately, achromatic quarter wave plates do not transmit perfectly circularly polarized light for all wavelengths, hence the background rejection is not perfect. The transmission and retardation of light achieved by the CVI Melles Griot ACWP-400-700-06-4 achromatic quarter wave plate is plotted in Figure 3.7 as a function of incoming wavelength. Nevertheless, though not optimal, the circular polarization principle does work and the TLC particle images obtained using the filter are shown in Figure 3.8.

All in all, the final result of the combination of a balanced white light source with the circular polarization filter is a substantial improvement of the TLC color particle images

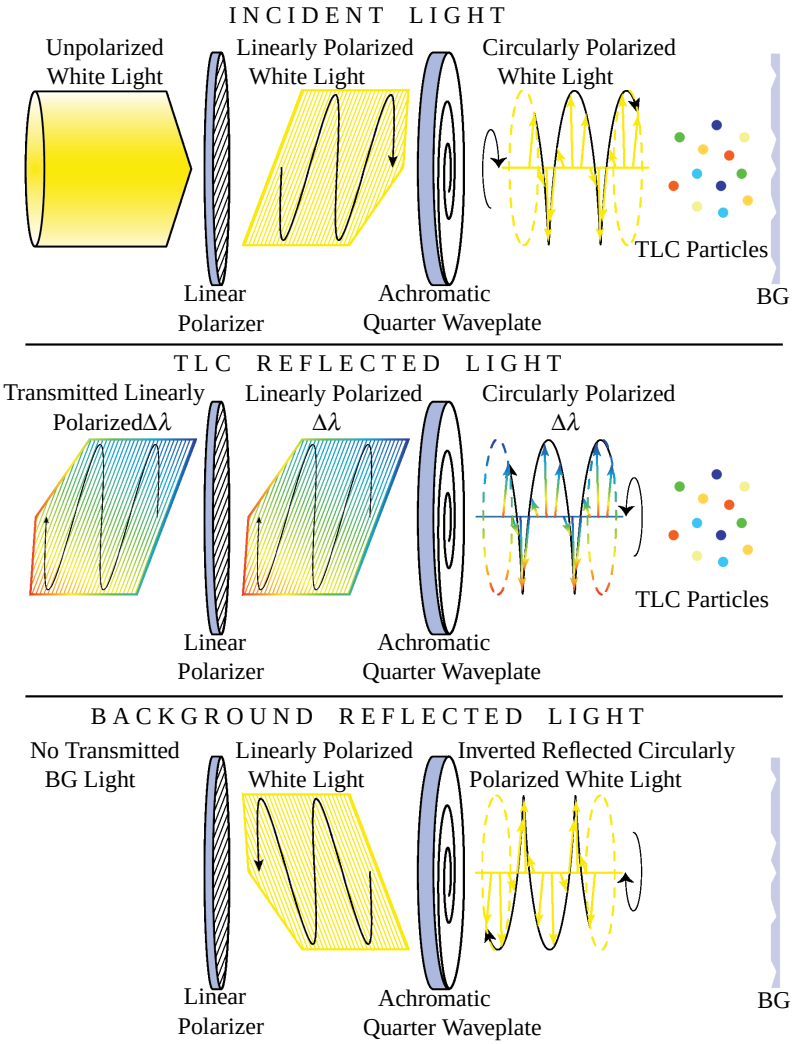

Figure 3.6.: Schematic of circular polarization filter for background reflection removal.

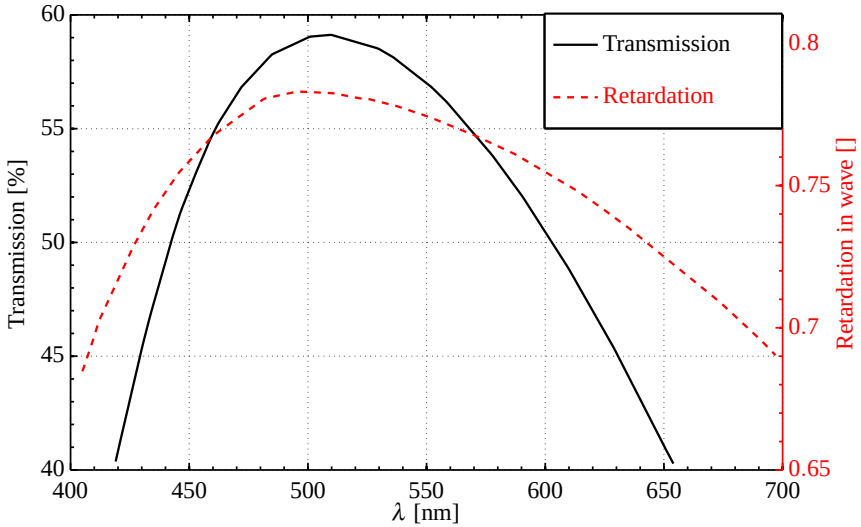

Figure 3.7.: Transmission and retardation of light provided by achromatic quarter wave plate (CVI Melles Griot ACWP-400-700-06-4) as a function of incoming wavelength.

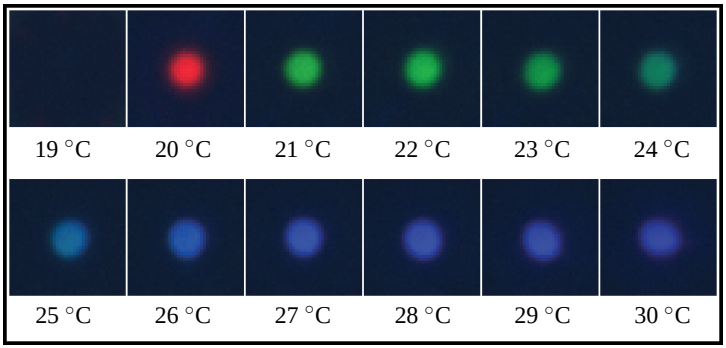

Figure 3.8.: Color images of non-encapsulated TLC particles (Hallcrest R20C5W) over their color response temperature range (20x magnification, illuminated with a Lumencor Spectra X light engine, through the circular polarizer.)

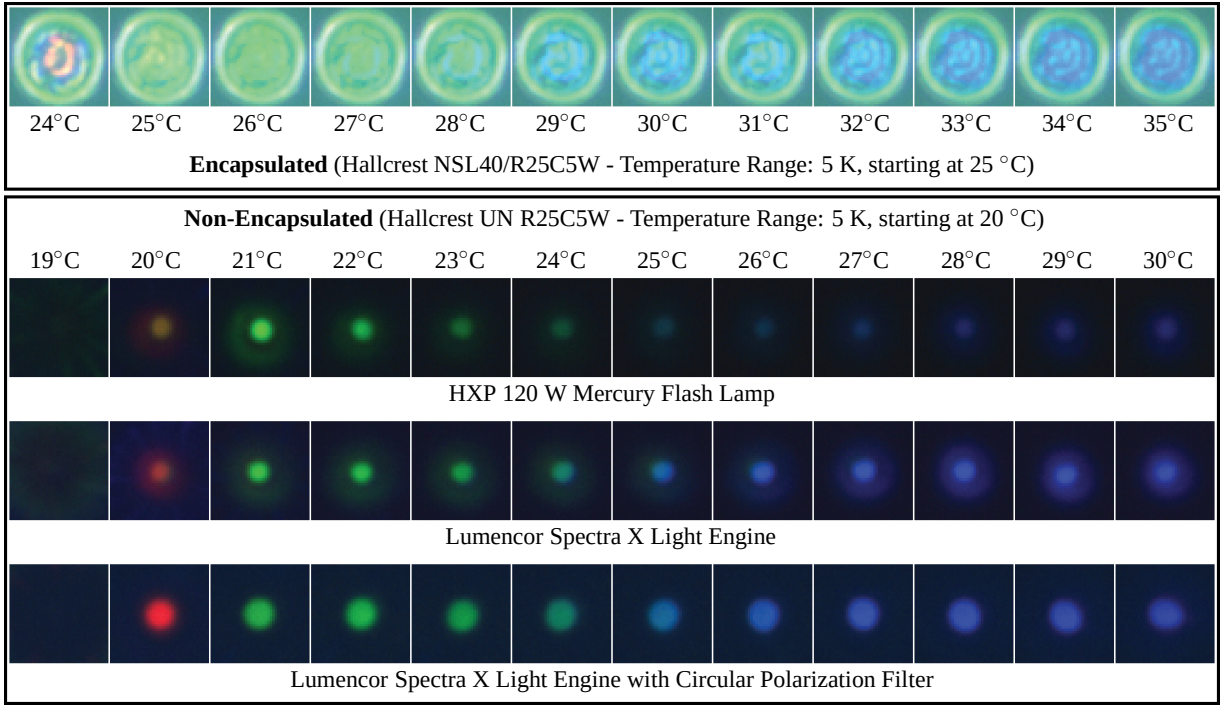

Figure 3.9.: Direct comparison of the particle images obtained with different illumination schemes for both encapsulated and non-encapsulated TLC particles with a temperature response range of 5 K.

that allows for a more precise estimation of the particles' temperature to be used as a flow diagnostic technique. Figure 3.9 shows a direct comparison of the particle images obtained with the various illumination schemes described so far for both encapsulated and non-encapsulated TLC particles with a temperature response range of 5 K. Furthermore, it will be shown in Section 6 that these particle images exhibit a high enough SNR for defocusing methods, such as APTV, to be used for the simultaneous time-resolved estimation of the particles' displacement and temperature in slow flows.

3.3. Image Acquisition Equipment

All experiments were performed at the microfluidics laboratory of the Bundeswehr University Munich (UniBw). The imaging system used to capture the flow snapshots is schematically shown in Figure 3.10 and consists of an Axio Observer Z.1 inverted microscope manufactured by Carl Zeiss AG, a Lumencor Spectra X light engine, a circular

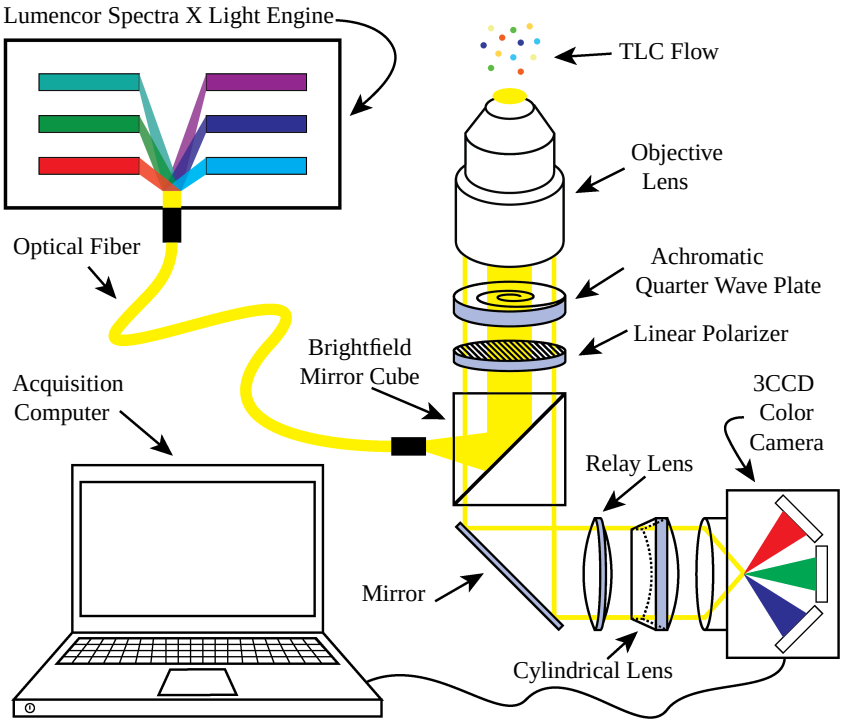

Figure 3.10.: Schematic of image acquisition system.

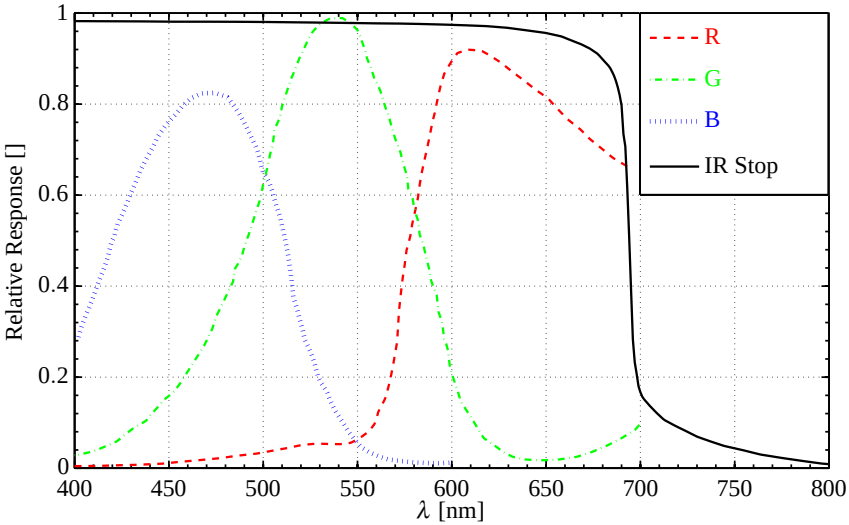

Figure 3.11.: Color response of the red green and blue sensors of a JAI AT-200 GE, 3CCD Progressive Scan RGB Color, 24-bit compounded dynamic range (8-bit per sensor), 1624×1236 pixel digital color camera.

polarizer (described in Section 3.2) and a JAI AT-200 GE, 3CCD Progressive Scan RGB Color, 24-bit compounded dynamic range (8-bit per sensor), 1624×1236 pixel digital color camera. The sensor alignment of the color camera was evaluated and yielded spatial discrepancies of less than 0.5 pixel. The color response of the red green and blue sensors of the camera is plotted in Figure 3.11.

The entire system was installed on a damped optical table to avoid the effect of vibrations in the measurements. The light was routed to the back aperture of the microscope via an optical fiber and redirected towards the flow sample with an brightfield filter cube, mounted inside the microscope. The circular polarization filter described in Section 3.2 was installed and aligned immediately under the objective lens as shown in Figure B.7, such that both the light from the Spectra X light engine, as well as the scattered light from the flow sample, traveled through it. LD Plan-NEOFLUAR, $20\times$ and $10\times$, infinity corrected objective lenses, with numerical apertures of $NA = 0.4$ and $NA = 0.3$, respectively, were used to focus the light on the flow sample, as well as to image the flow itself. The acquisition frame rate for all measurements was the camera's maximum 15 fps and fields of view of 353×269 μm^2 and 677×515 μm^2 were obtained for $20\times$ and $10\times$ magnifications, respectively. The nuclei of the in-focus particle images, without astigmatic aberrations, were approximately 20 pixel and 6 pixel in diameter, on average, for $20\times$ and $10\times$ magnifications, respectively.

4. Astigmatism Particle Tracking Velocimetry

As mentioned in Section 1.2.2, since Santiago et al. (1998)'s introduction of a PIV system for microfluidics, the method has evolved into a mainstream flow diagnostic tool for devices used in lab-on-a-chip, micro-chemical, and micro-biological applications, among others. The μPIV technique provides a two-dimensional, two-component (2D2C) measurement of the velocity field. However, even though flows with microscopic dimensions are usually laminar, their velocity distribution can be very complex and fully three dimensional, e.g. in geometries where obstacles are present. Moreover, μPIV measurements are biased due to the fact that volume illumination is used and the measurement plane is rather a volume thus introducing an unavoidable error when evaluating steep gradients (Olsen & Adrian 2000). This is why there have been multiple recent efforts to develop reliable methods with the capability of evaluating all three components of velocity in microscopic flows.

The adaptation of multi-camera three-dimension, three-component (3D3C) measurement techniques to microscopic applications is not a trivial task due spacial restrictions and limited optical access. Therefore, many 3D3C measurement techniques, applicable to microscopic flows, use a single camera and take advantage of particle defocusing to encode the depth position of the particles, making it possible to track them in 3D. The reader is referred to the summary and discussion of Chen et al. (2009) and Cierpka et al. (2010), for more information of the different defocusing techniques that have been used for microfluidics measurements (Pereira & Gharib 2002, Yoon & Kim 2006). Kumar et al. (2011), Cierpka et al. (2011a,b), Muller et al. (2013) reported other applications of APTV to fully 3D flows in microfluidics.

One of the most important challenges that 3D defocusing techniques face is a reliable calibration procedure to obtain the depth position of the particles using the nature of their images. In Astigmatism Particle Tracking Velocimetry (APTV), the optical symmetry of the imaging system is broken by mounting a cylindrical lens between the imaging optics and the camera sensor. The cylindrical lens introduces an astigmatic aberration to the particle images, allowing for the encoding of the particle's out-of-plane position in the geometry of their image. One of the many advantages of this technique is the simplicity of its implementation; the only requirement for the technique to be successfully used is the proper placement and alignment of the cylindrical lens in front of the camera, as shown in Figure 3.10. This means that standard μPIV systems can be easily modified to make APTV measurements.

4.1. Astigmatism principle

The optical principle of the APTV technique is schematically depicted in Figure 4.1. The top part of the figure shows how particles are imaged by a conventional system. In this case, an arrangement of spherical lenses, which varies depending on the microscope or the optical arrangement, would project spherical particles as circular particle images on the camera sensor, whose diameter is inversely proportional to the distance from the focal plane of the imaging optics. The introduction of a cylindrical lens, as the one shown in the bottom part of Figure 4.1, breaks the symmetry of the imaging system due to the fact that the cylindrical lens focuses light in the *y*-axis, as does a conventional spherical lens, but acts as a flat window in the *x*-axis (assuming, of course, that the axis of the lens

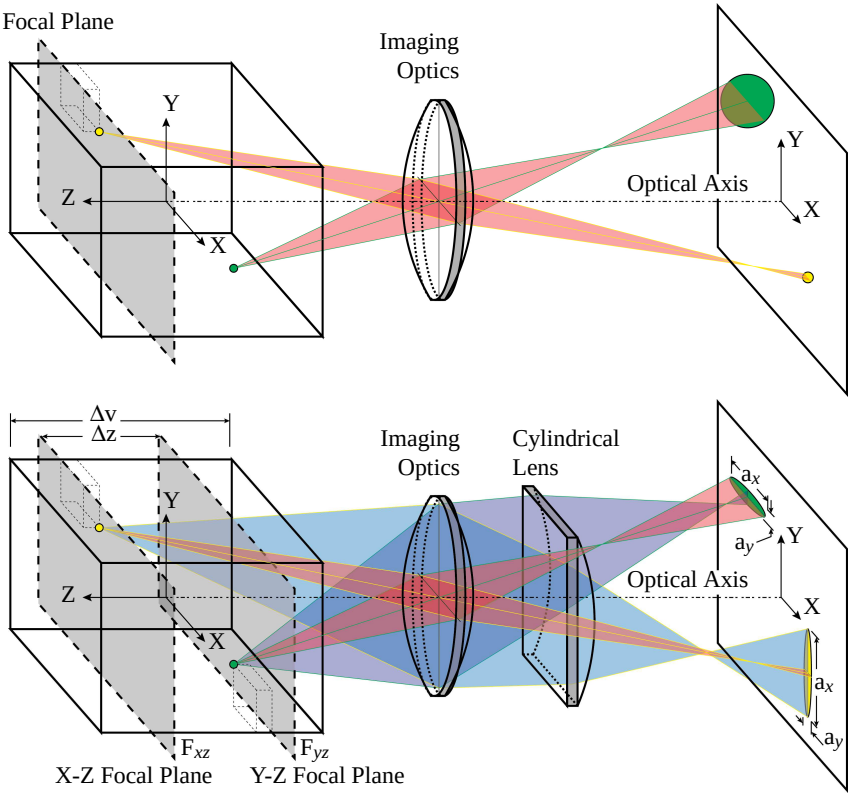

Figure 4.1.: Schematic of optical astigmatism in particle imaging.

is properly aligned), hence not changing the trajectory of transmitted light rays in the $X-Z$ plane. The result are two different $X-Z$ and $Y-Z$ focal planes, labeled as F_{xz} and F_{yz} in Figure 4.1, respectively. Since the cylindrical lens does not affect the optical system in the $X-Z$ plane, F_{xz} lies in the same position as the focal plane of the optical system without the cylindrical lens. Conversely, since the cylindrical lens does act as an additional lens in the $Y-Z$ plane, F_{yz} moves closer to the imaging optics by a distance Δz. Now, since the diameter of the particle images is inversely proportional to their distance from the focal plane, spherical particles are projected as ellipses in an astigmatic imaging system, as opposed to the conventional circular images. What is more, the *x*-axes, a_x, of the elliptical particle images will be the same as their diameter when projected without astigmatism, while their *y*-axes, a_y, will change relative to their distance from F_{yz}. Hence, a particle that lies closer to F_{yz}, yields an elliptical image with a shorter a_y than one that lies further away. This way, horizontal ellipses represent particles that lie close to F_{yz}, while vertical ellipses represent particles that lie close to F_{xz}. This information can then be used to estimate and track the out-of-plane position of the particles in the measurement volume (Cierpka et al. 2010).

4.2. Out-of-plane (z) component calibration

There have been different approaches to the calibration of the out-of-plane position of particles using a_x and a_y. For instance, the difference, $a_x - a_y$, and the ratio, a_x/a_y, were used by Chen et al. (2009) and Cierpka et al. (2010), respectively, to make 3D3C velocity measurements inside a microchannel. Either one of these calibration approaches, however, requires that the detected particles lie in the volume within F_{xz} and F_{yz} to preserve unambiguity, limiting the measurement volume to $\Delta z = F_{xz} - F_{yz}$. This turns out to be a substantial limitation for experiments that produce particle images with high signal-to-noise ratios (SNR) since particles can be detected even when they lie beyond the F_{xz}, F_{yz} boundaries. Cierpka et al. (2011a) used a different calibration approach, using a mathematical model, proposed by Olsen & Adrian (2000), that predicts the particle image diameter as a function of the particle's distance from the focal plane. The intensity profile of the color images obtained from the TLC particles investigated in this study are different from those of monochromatic particle images, such as those present in conventional APTV experiments. Hence, the model proposed by Olsen & Adrian (2000) and implemented by Cierpka et al. (2011a) for the calibration of the *z*-position, was not used for the calibration of TLC-particle color images. Instead, a look-up table of known *z*-positions for specific a_x, a_y pairs, was used to estimate the *z*-position of the TLC particles.

The *z*-position of non-encapsulated Hallcrest R20C1W TLC particles was estimated using the approach outlined in the following paragraphs. The TLC material has a temperature response range of 1 K, and a red start temperature of 20 °C. The color images were acquired with a magnification of 20×, and a cylindrical lens with a focal length

of 500 mm, was mounted in front of the 3CCD camera. The Lumencor Spectra X light engine was used to illuminate the particles, routing the light through a circular polarizer, as outlined in Chapter 3. A droplet of TLC-containing emulsion, diluted in water, was placed between two microscope glass plates and left for some minutes until the TLC particles had settled on the surface of the bottom plate. The particle distribution was then observed with the imaging system described in Section 3.3 and a scanning procedure was carried out, recording images of the TLC particles over a span of 28 μm. Figure 4.2 shows a scatter plot of the horizontal and vertical axes, a_x and a_y, of the elliptical images generated by a single particle as a function of its z-position throughout the scan. As stated above, the axes, a_x and a_y, of the elliptical particle images have an inversely proportional relationship with the distance from their respective focal planes, F_{xz} and F_{yz}, as can be appreciated in Figure 4.2. Moreover, it is also clear from Figure 4.2 that particles can be detected far beyond the Δz limits, hence rendering the use of a relationship between a_x and a_y, for the calibration of the particles' z-location, a waste of data. This is why a look up table will be used for the determination of the z-position instead, which allows for the estimation of z over a larger measurement volume (Δv). Figure 4.3a shows a scatter plot of a_x vs a_y for all the particles detected during the calibration scan, with the z of each data point given by the color map. The algorithm that detects the geometry of the elliptical color particle images is not perfect and occasionally over- or underestimates the axes

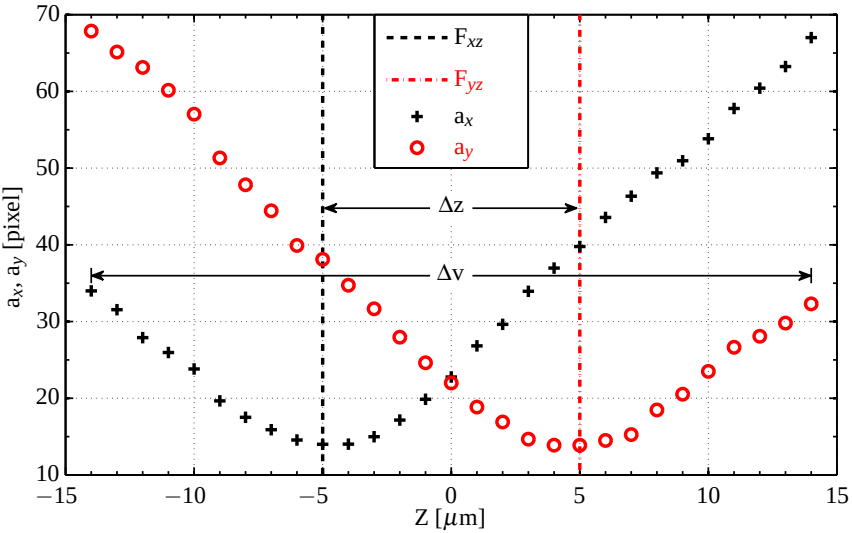

Figure 4.2.: Horizontal and vertical axes, a_x and a_y, of the particle images generated by a single non-encapsulated Hallcrest R20C1W TLC particle as a function of its z-position.

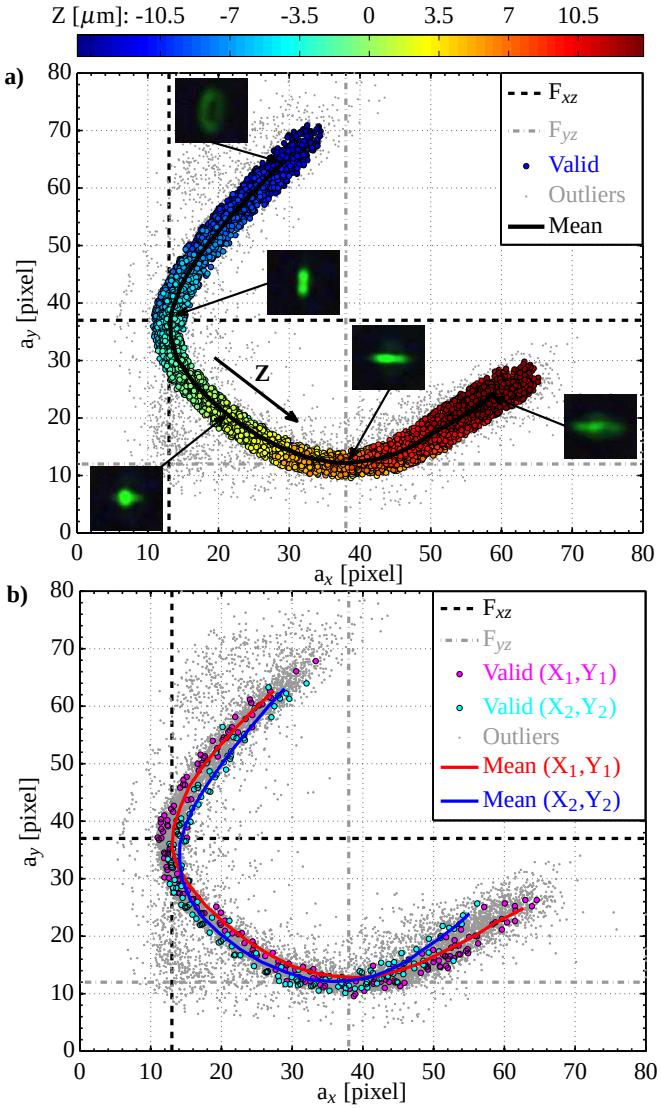

Figure 4.3.: Scatter plot of a_x vs a_y for valid particles detected during the calibration scan. Gray points indicate outlier (a_x, a_y) values and line plots are smooth, interpolated mean (a_x, a_y) values at the temperatures covered in the calibration scan. a) Colored circles indicate viable particles to be used for calibration function computation. b) Colored circles indicate valid particles in different (x,y) of the image and colored lines correspond to the respective colors of the circles.

lengths. This is why a set of detected particles' data, plotted as colored circles, is selected for the calibration of the particles' z-position. Along with the plot of the data points, actual images of the particles at different z-positions are displayed in order to provide the reader a clearer understanding of the underlying pattern that allows for the estimation of the z-position from the geometry of the particle images. The mean a_x and a_y lengths was then calculated for all detected particles at each z step and smoothing and interpolation algorithms were used to obtain the black calibration curve plotted in Figure 4.3a. The z-position, z_i, of a particle image with elliptical axes, (a_{xi}, a_{yi}), was then determined by finding the point, $(a_x(z_i), a_y(z_i))$, along the black curve, that minimizes the Euclidean distance from (a_{xi}, a_{yi}).

However, as reported by Cierpka et al. (2011a), the $X-Z$ and $Y-Z$ focal planes, F_{xz} and F_{yz}, are not actual flat planes in reality, nor are they parallel. Cierpka et al. (2011a) performed a calibration scan, recording images of a square grid at increasing z-positions, and reconstructed the XZ and YZ focal iso-surfaces using a local focus function based on the variance of the image intensity (Sun et al. 2004). The optical aberrations caused by the spherical and cylindrical lenses cause F_{xz} and F_{yz} to be ellipsoid surfaces instead of flat planes. For this reason, the elliptical image's geometry of a particle would vary for different (x,y) locations in the image, introducing a systematic error in the determination of the particle's z-position. To illustrate this effect, Figure 4.3b shows a scatter plot of the same data that is plotted in Figure 4.3a. In Figure 4.3b, however, the smooth red and blue calibration curves were computed using the mean a_x and a_y of particle images (plotted as magenta and cyan colored circles, respectively) located in two different (x,y) regions of the image. Hence, it becomes clear from Figure 4.3b why a single calibration curve for all detected particles introduces a substantial systematic error that can be corrected. In order to make this correction, two-dimensional (2D) square polynomial surface fits were calculated for both a_x and a_y distributions at each z-step of the calibration scan. This procedure provides a specific calibration curve for every (x,y) location in the image, thus compensating for the optical aberrations that cause the distortions in F_{xz} and F_{yz}.

4.3. Uncertainty analysis

The calibration procedure outlined in Section 4.2 was used to estimate the z-position of the particles that were detected in calibration scans, recorded with $20\times$ and $10\times$ magnifications, and a cylindrical lens with a focal length of 500 mm. 13325 and 72137 particle images were detected throughout the entire scan data, using $20\times$ and $10\times$ magnifications, respectively. An outlier detection scheme yielded 10401 (78%) and 62498 (87%) valid particles, for the $20\times$ and $10\times$ magnifications cases, respectively, whose a_x and a_y were not under- or overestimated beyond a threshold, calculated as follows. Since the calibration procedure provides a calibration curve for each and every (x,y) location in the image, outliers were determined by segregating valid particle images as those whose axes

pairs, (a_x, a_y), lay within an Euclidean distance of 2 pixel from their respective calibration curve (determined by their (x,y) location in the image).

The standard deviation of the estimated z from the true value, σ, given by

$$\sigma = \sqrt{\frac{1}{N}\sum_{i=1}^{N}(z_i - z_{\text{real}})^2} \tag{4.1}$$

was calculated for each step of the calibration scan, where N is the number of parti-

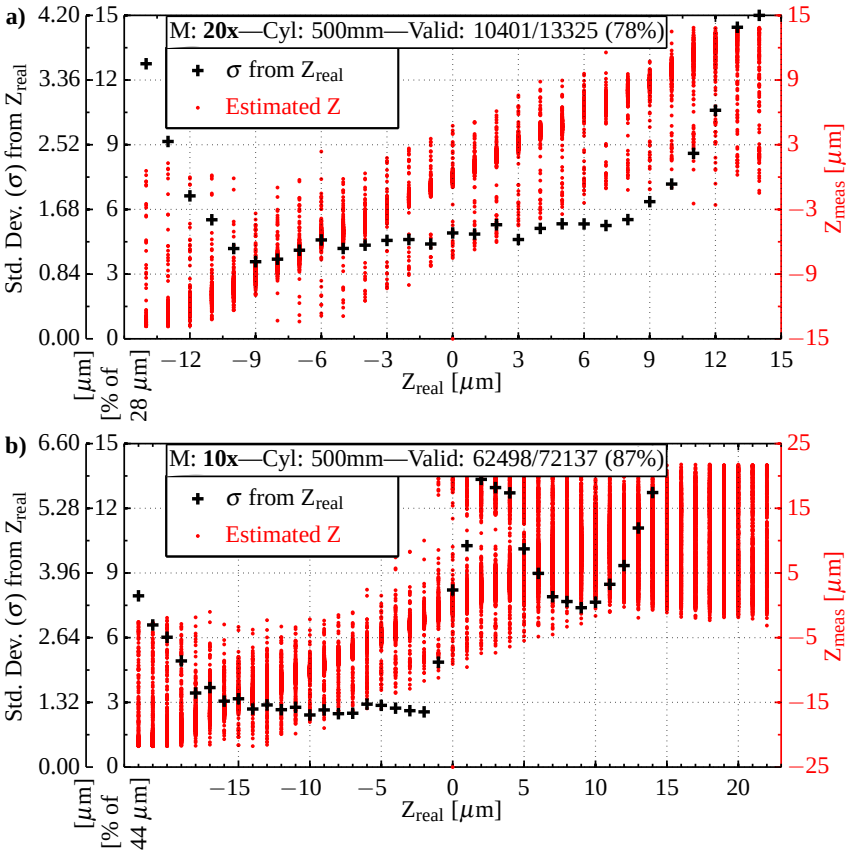

Figure 4.4.: Scatter red point plot of valid particles' estimated z-position. Standard deviation from the true value, σ, as black crosses; left vertical axes in absolute and relative units for uncertainty evaluation. a) Calibration with 20× magnification. b) Calibration with 10× magnification.

cles detected at each step and z_i are the estimated z-positions of valid detected particles. Figure 4.4 shows a red scatter plot of all the valid particles' estimated z-position, z_{meas}, plotted against their real z-position, z_{real}. The standard deviation from the true value, σ, is also plotted in Figure 4.4, as black crosses, for the full span of z positions covered in the calibration scan. The left vertical axis of the plot shows two unit scales, namely μm and % of 28 μm, in order to allow for the calibration approach's uncertainty evaluation in both absolute and relative terms. It is clear from the plots in Figure 4.4 that the calibration procedure allows for the correct determination of the particles' z-position. However, a distribution of particles whose z-position is underestimated can be seen for $-9 < z < 9$ μm in the 20$\times$ magnification case. This is a result of a deficiency in the detection algorithm which would be improved either with a better detection scheme or with higher quality particle images. A substantial increase in the z estimation uncertainty is also evident for $z < -10$ μm and $z > 10$ μm, in the 20$\times$ magnification case, which is also a result of a lack in robustness of the detection algorithm for heavily defocused particle images. For $-12 < z < 9$ μm, in the 20$\times$ magnification case, the standard deviation of the estimated z from the true value, remains under 6% of the measurement volume. On the other hand, using 10$\times$ magnification allows for a larger measurement volume but the defocused particle images, corresponding to particles that lay closer to the camera (the bottom region of the flow, $z_{\text{real}} > 0$), display star-like aberrations which make the proper detection of their elliptical shape very challenging. This is the reason why the current imaging system, using a magnification of 10$\times$, does not meet the quality standards to provide good enough color elliptical particle images that allow for the 3D tracking of these non-encapsulated TLC particles. Nevertheless, the data obtained with a magnification of 20$\times$, is in fact viable for APTV even though the uncertainty values are higher than those reported for standard APTV, using fluorescent particles and laser illumination, by approximately one order of magnitude (Cierpka et al. 2011a, Muller et al. 2013, Fuchs et al. 2014). It should be noted, in any case, that the imaging conditions for conventional APTV experiments are very different, considering that lasers provide light that is orders of magnitude brighter than the white light provided by the Spectra X light engine, and achromatic quarter wave plates do not transmit perfectly circularly polarized light for all wavelengths, thus making background filtering substantially less efficient than that obtained with fluorescent arrangements. All in all, although the measurement method still counts with much room for improvements, the successful 3D tracking of color TLC particles in a flow volume remain unprecedented to this day, and the uncertainty levels obtained in this study still allow for their time-resolved tracking in a microscopic 3D flow, as is shown in Chapter 6.

5. Thermo-Liquid Crystal (TLC) Thermography

5.1. Temperature Calibration

Just like with most measurement techniques, converting the raw measured data to the desired physical quantity, in this case temperature, has been a topic of itself since the birth of the technique. So far, the hue-temperature dependence has been reported on most experimental studies as the basis for the calibration of the digital images even though a limited amount of research has been performed on directly using the R, G, B color components of digital images to extract the temperature (Vejrazka & Marty 2007). A thorough review of the literature pertinent to this particular topic can be found in Section 5.1 of Dabiri (2009)'s review and Section 5.3.1 of Abdullah et al. (2010)'s report. Rao & Zang (2010), Bednarz et al. (2010), and Cukurel et al. (2012) report the most recent studies and advances in the hue-temperature calibration of TLCs. Though this approach has worked for years and sophisticated computational methods such as neural networks have been used to improve the calibration results, the RGB to hue conversion is not the optimal mathematical transformation to evaluate the temperature since the units of hue are in radians, which is a periodic scale and hence presents a challenge at the time of calculating a calibration curve that allows for the estimation of unique temperature values for any measured hue. Furthermore, the hue-temperature relationship neglects the saturation and intensity variables of the HSI color space, which also contain valuable information that can play a role in reducing the uncertainty of the temperature calibration.

The color image data for the temperature calibration was obtained using a droplet of TLC-containing emulsion (see Section 3.1), which was poured on a microscope glass plate. A Peltier element was then mounted immediately above the droplet such that the fluid was in direct contact with its heating surface, as schematically shown in Figure 5.1. The thickness of the fluid layer (TLC droplet) between the glass plate and the surface of the Peltier element was approximately 1.5 mm. The temperature of the Peltier element was automatically controlled by a feedback controlled custom module, implemented in an in-house image acquisition software, written in MATLAB, using a Peltier-Controller TC2812 manufactured by CoolTronic GmbH and a mini Pt1000 thermocouple. The temperature of the Peltier element was initially set to a temperature below the red starting temperature of the TLC material and subsequently increased in discrete steps to a temperature beyond the blue temperature of the material. Color images were acquired at each step and the acquisition software waited until the temperature in the fluid (measured with the mini Pt1000 thermocouple) was stable, within 0.1 K of the target temperature for each step, for ten seconds. The fluid was only illuminated for the short lapses of time

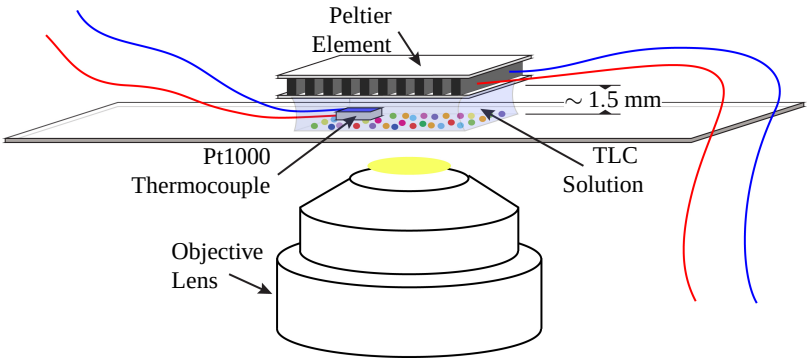

Figure 5.1.: Schematic of TCL calibration experiment.

required for the camera to acquire an image (the microscope shutter was opened once the desired temperature was reached and the camera was ready to acquire, and closed after the images were recorded). The time response of the TLC material was not measured for this study but the reader can refer to Ireland & Jones (1987) for a study on the response time of TLC thin sheets, where they report delay times of 3 ms. The TLC-containing droplet remained in contact with the peltier element for approximately fifteen minutes, which was the time required for the temperature scanning procedure, and no abrasion or bleeding was observed in the TLC particles. An experiment, where the TLC material was exposed to intense light for a longer period of time, is discussed in Section 5.2.

Three different sets of data were used to find the most reliable way to extract the temperature of the individual TLC particles from their color images: 1. The RGB data, normalized by the maximum dynamic range of the 3CCD camera sensors (255 counts), 2. the HSI color space, calculated as described in Section 2.2, and 3. the proper orthogonally decomposed (POD) RGB data, also calculated as described in Section 2.2. Figur 5.2 shows the color variables all three color spaces, plotted as a function of temperature for an emulsion containing Hallcrest R20C5W TLC particles, with a temperature response range of 5 K, and a red start temperature of 20 °C. The color images were recorded with a magnification of 20× and the fluid was illuminated with a Lumencor Spectra X light engine, through the circular polarizer described in Section 3.2. As previously mentioned, the hue (H) variable has been the predominantly used variable to perform the temperature calibration of TLC images, according to the available research reports. It is clear, however, from Figure 5.2b, that not only H shows a temperature-dependent pattern but S and I do as well. Now, if the H values alone can be used to estimate the temperature of the, it is only natural to expect that two more variables showing clear patterns would provide valuable information to improve the accuracy of the calibration. This is the reason why a multi-variable calibration, which makes use of all the color information, as opposed to a single variable in periodic units, is evaluated in this study.

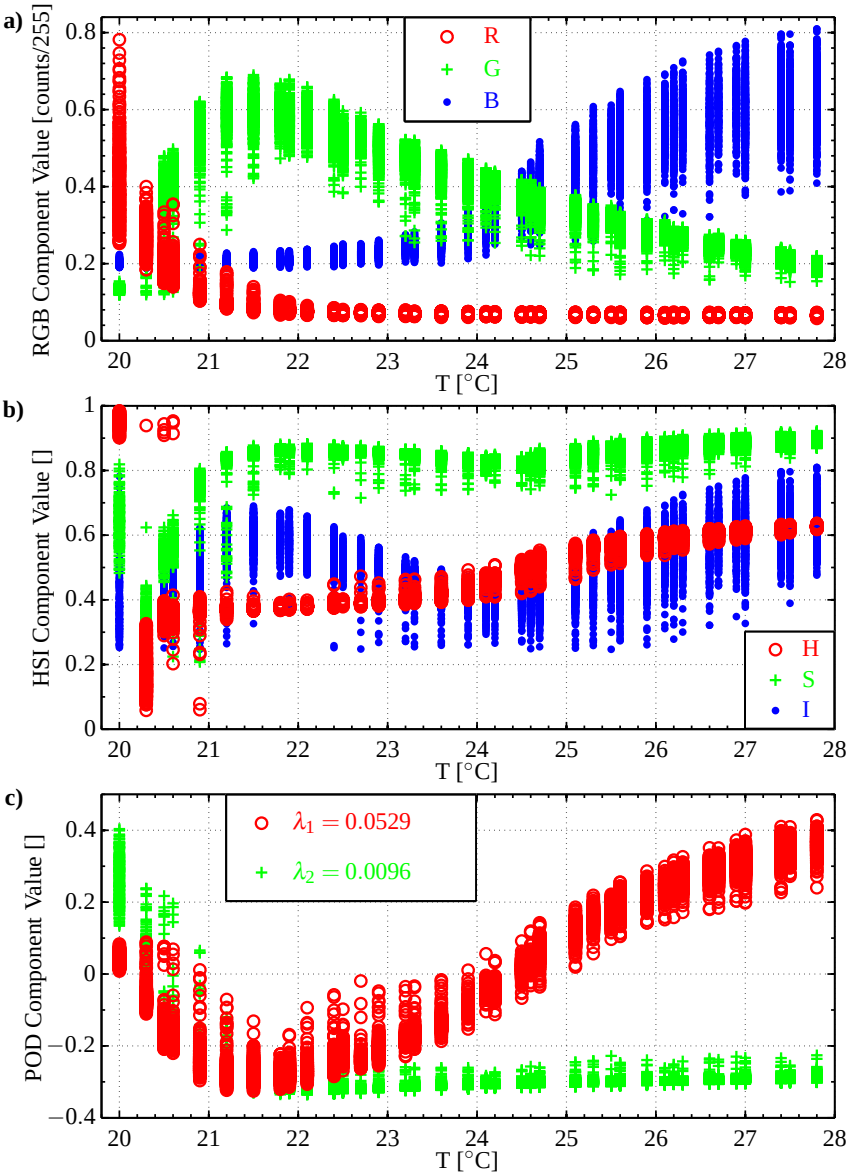

Figure 5.2.: Scatter plot of: a) RGB values, b) HSI values, and c) POD components associated with the eigenvalues $\lambda_1 = 0.0542$ and $\lambda_2 = 0.0075$ for detected TLC particles (Hallcrest R20C5W, 20x magnification).

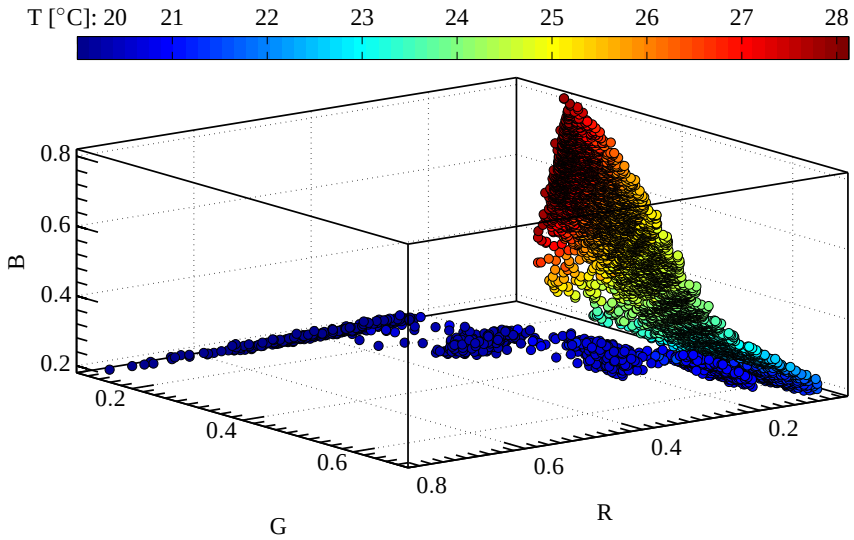

Figure 5.3.: 3D scatter plot of RGB values for detected TLC particles.

A thorough calibration analysis was performed to find the ideal method for extracting the temperature from the colored TLC particle images. Even though RGB values are strongly affected by optical arrangements, and do not necessarily respond to experimental conditions variations in the same manner, thus making them very susceptible to bias errors in the temperature estimation, a calibration was performed using the raw RGB color components of the particle images as did Vejrazka & Marty (2007). Figure 5.3 shows a 3D scatter plot of the RGB components of the particles detected with the temperature of each point given by the color map. This figure illustrates how all three color components provide valuable information required to precisely extract the temperature of particles that lie in the flat regions of the individual component profiles from Figure 5.2a, thus providing a pronounced data pattern to which a 3D polynomial can be fitted in order to obtain a precise calibration curve that works throughout the temperature range. Vejrazka & Marty (2007) used a similar approach to evaluate the average two-dimensional temperature fields of a macroscopic impinging jet flow and reported uncertainty values of < 0.3 K in a range of 8.5 K (3.5%).

As mentioned in Section 2.2, an alternative to directly using the R, G, and B components of color is to use the H, S, and I (HSI) color space. The HSI color space is a perspective of color evaluation that uses a non-reversible mathematical transformation of the R, G, and B data instead of their raw values (see Section 2.2). Furthermore, the relationship between temperature and H (hue value), has been the calibration method used by the great majority of researchers over the lifetime of the TLC thermography technique.

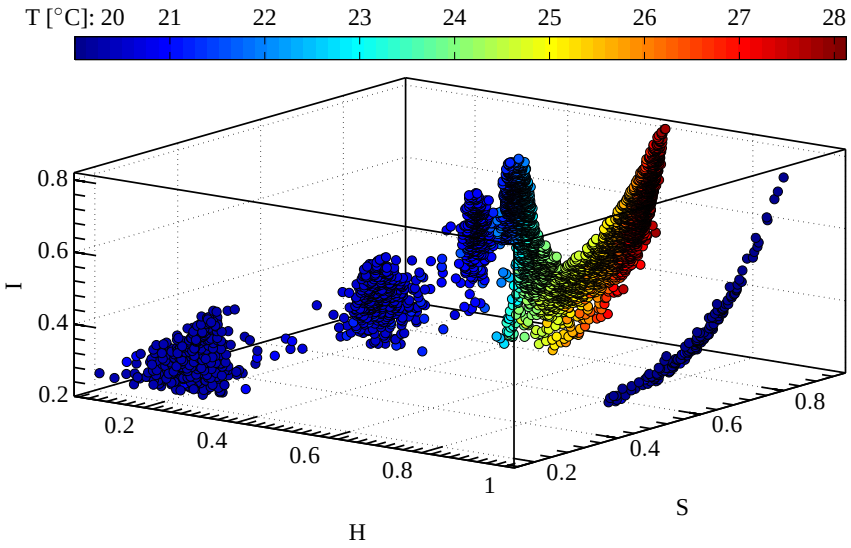

Figure 5.4.: 3D scatter plot of HSI values for detected TLC particles.

Analogous to Figure 5.3, Figure 5.4 shows a 3D scatter plot of the HSI components of the particles detected with the temperature of each point given by the color map. Conversely, this figure also illustrates how the S and I data provide valuable information required to precisely extract the temperature of particles that lie in the flat regions of the H profile from Figure 5.2b, once again providing a pronounced data pattern to which a 3D polynomial can be fitted in order to obtain a precise calibration curve that works throughout the temperature range. The reader should note, however, the group of blue points, corresponding to particles around 20 °C, that lie in a section of the plot, some distance away from where the temperature trend leads. This is a result of the periodic nature of the hue value. Hence, two particles with identical temperatures may scatter slightly different intensities of red, green and blue light, which can cause that their respective hue values vary drastically from 0.01 to 0.99, making the calibration procedure a challenging task. Fujisawa & Hashizume (2001) performed a study with synthetic data and compared results for the calibration of temperature using its relationship with H, H and S, and H, S and I. They state that there is a clear advantage to using the S and I image data and reported an uncertainty of 0.06 K in a range of 2.3 K (2.6%), evaluating the average temperature in interrogation windows. Fujisawa et al. Fujisawa et al. (2005) later reported uncertainty values of 0.13 K, using a stereoscopic setup (also 2D interrogation windows), on TLCs with a temperature response range of 2.3 K (5.7%), also calibrating temperature with all three variables. Note that all of the research done up to this point has been performed us-

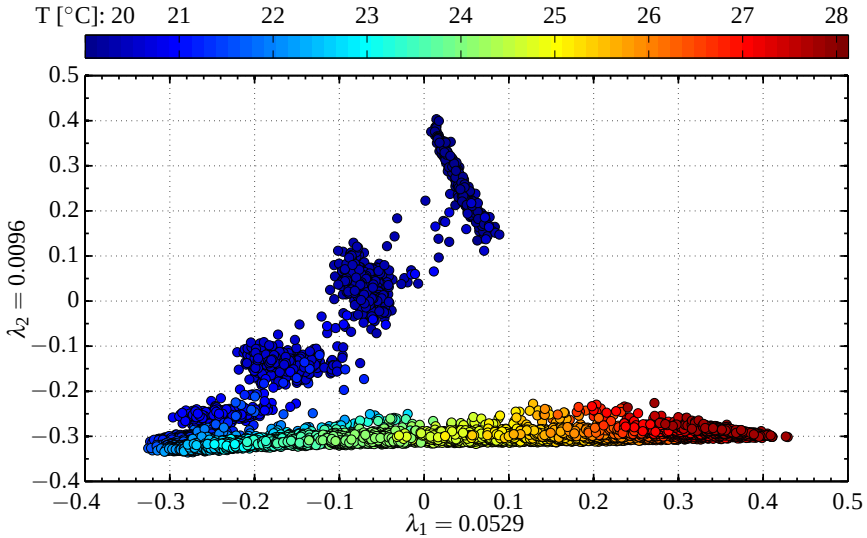

Figure 5.5.: 2D scatter plot of POD components associated with the eigenvalues $\lambda_1 = 0.0542$ and $\lambda_2 = 0.0075$ for detected TLC particles.

ing mean color values, calculated over designated areas of the sensor, and not individually for each tracer particle. As mentioned in previous sections, this fact is of major relevance for experiments in microfluidics since the recorded images integrate the light over the entire illuminated volume, introducing a strong bias in two-dimensional averages which does not occur with three-dimensional particle tracking. The temperature of individual TLC micro droplets evaluated in this study was also calibrated using all three H, S and I color variables evaluated at the core of each particle image.

A third variable space, resulting from the decorrelation of the RGB image data via proper orthogonal decomposition (POD) (Roesgen & Totaro 2002), as outlined in Section 2.2, was used to fit a 2D polynomial in order to obtain a calibration curve for the estimation of the individual particles' temperature. Figure 5.5 shows a 2D scatter plot of the x_1 and x_2 POD components, associated with the non-zero eigenvalues $\lambda_1 = 0.0529$ and $\lambda_2 = 0.0096$, of the detected TLC particles, with the temperature of each point given by the color map.

The algorithm that detects the colored regions of the particle images is not perfect and occasional outliers appear in the color distributions, which is why a select set of detected particle images, plotted in Figures 5.2-5.5, was used to calculate the temperature calibration function. The criteria for the outlier removal procedure include a requirement that valid particle images have a maximum R, G, or B intensity above a defined threshold, in order to ignore detected spots, such as white particle halos or other bright features, that

do not correspond to actual TLC particles; in the case of the particular example depicted in Figures 5.2-5.5, this threshold was $I = 60$ counts. A detailed description of the image processing procedure implemented to detect the color particle images can be found in Appendix A. The RGB values of each particle image were determined by calculating the average intensity counts recorded by the pixels that make up the detected particle image, which are above a threshold of 0.7 times the difference between the maximum and minimum grayscale values of those same pixels. The HSI and POD values of each particle image were then calculated using these RGB values, as outlined in Section 2.2.

Calibrations were made by fitting a three-dimensional third-degree polynomial to the RGB and HSI data, and a two-dimensional third-degree polynomial to the POD data. This was done using a standard least-squares approach to solve the system of linear equations given by,

$$\begin{pmatrix} T_1 \\ T_2 \\ \vdots \\ T_i \end{pmatrix} = \begin{pmatrix} f(V_1,V_1,V_2)_1 \\ f(V_1,V_2,V_3)_2 \\ \vdots \\ f(V_1,V_2,V_3)_i \end{pmatrix} \cdot \begin{pmatrix} c_1 \\ c_2 \\ \vdots \\ c_k \end{pmatrix} \tag{5.1}$$

where $f(V_1,V_2,V_3)_i$ are arrays with the terms of the fit polynomial, corresponding to each particle's color space data, and c_k are the corresponding fit coefficients.

This approach was chosen over the look-up table method outlined in Section 4.2 because it is a more robust calibration method for the three variable spaces considered in this study, namely the RGB, HSI, and POD discussed above. The argument behind this statement is mainly the periodic nature of the H variable, which makes a 3D look-up table approach a very challenging task for the HSI color space, given that a smooth data trend is not present for a color series that progresses from red to blue. Therefore, a calibration function calculated with the system matrix characterized in Equation 5.1 resulted in a more reliable approach to estimate the temperature of the TLC particles using their color, and compare the performance of the method using the aforementioned color spaces.

5.2. Hysteresis and Bleaching

A simple experiment was performed to evaluate the hysteresis displayed by the TLC material when heated and cooled some degrees beyond its blue and red temperatures, respectively. The temperature scanning procedure, described in Section 5.1, was executed four consecutive times and the TLC material was heated to 35 °C and subsequently cooled to 15 °C after each temperature scan. The mean color values for the RGB, HSI and POD color spaces are plotted in Figure 5.6 as a function of temperature for the four individual scanning runs; the symbol size of the scatter plot increases for subsequent scan runs. Even though a hysteresis trend of decreasing blue levels for temperatures above 23 °C is clear

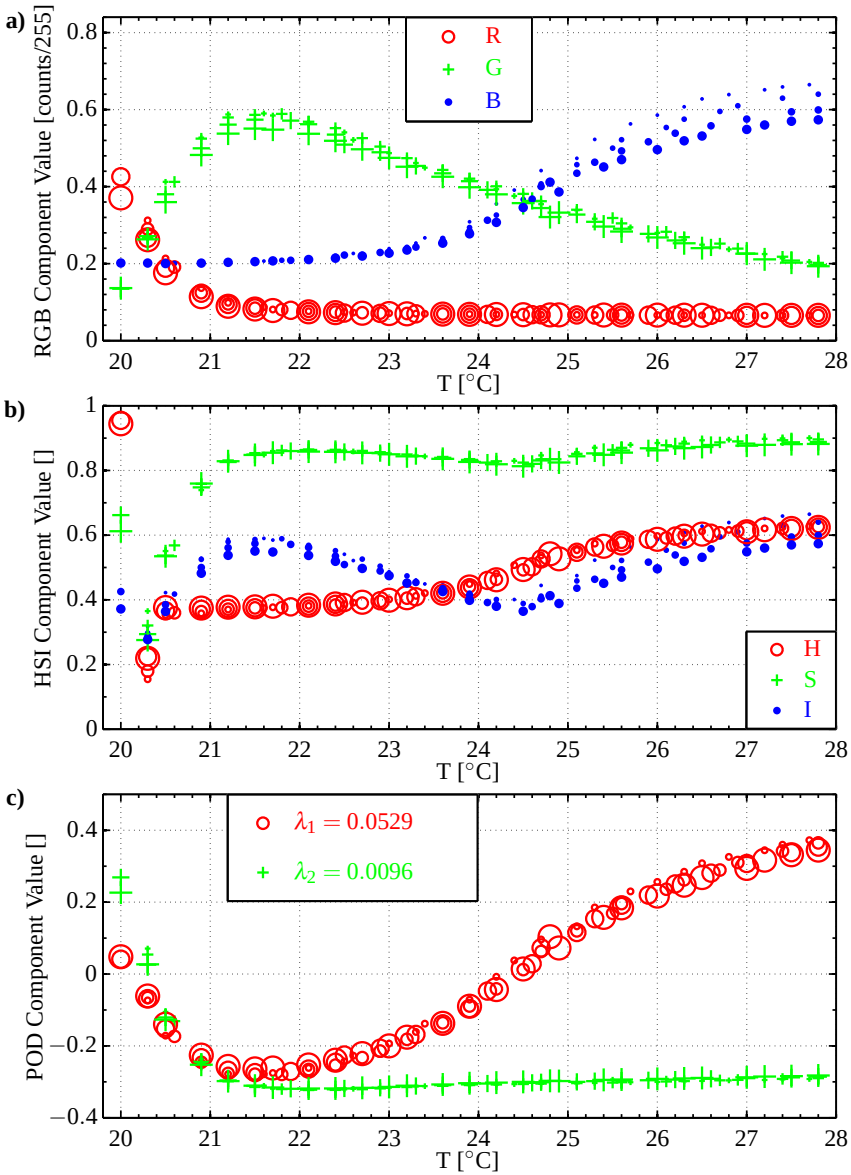

Figure 5.6.: Mean color values of TLC particles detected in four independent calibration scans. a) RGB values, b) HSI values, and c) POD components associated with the eigenvalues $\lambda_1 = 0.0542$ and $\lambda_2 = 0.0075$. The symbol size increases for subsequent scan runs.

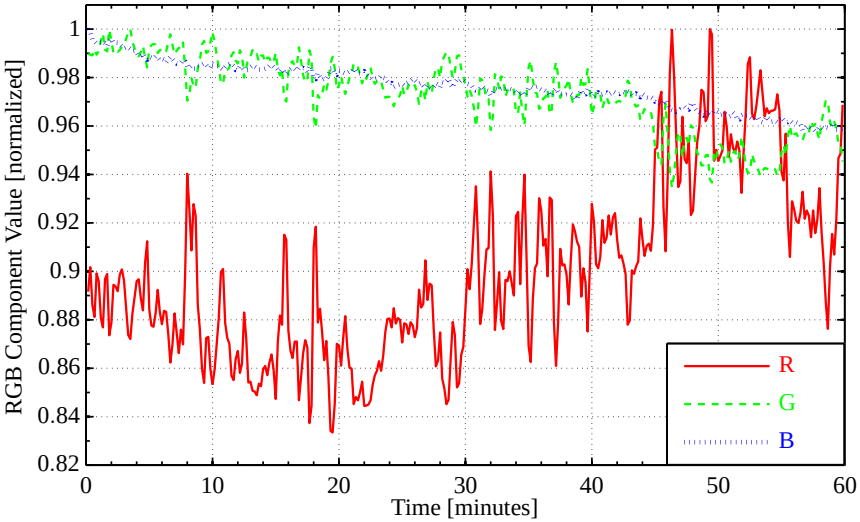

Figure 5.7.: RGB intensities of TLC particle images during 60 minutes of continuous illumination.

in Figure 5.6, from one calibration scan to the next, the red and green intensities do not show a hysteresis effect. In the HSI color space, the hysteresis effect is not as pronounced but a slightly less pronounced decrease in the I signal is evident for temperatures above 25 °C. Lastly, the proper orthogonal decomposition (POD) of the RGB data seems to compensate for the hysteresis in the B signal and a consistent hysteresis pattern was not detected in the POD components associated with the non-zero eigenvalues λ_1 and λ_2.

In order to evaluate the effects that prolonged illumination, using the Lumencor Spectra X light engine, has on the TLC material a simple bleaching experiment was performed, keeping a constant temperature of 21 °C in a droplet seeded with TLC particles. The particles were illuminated for a period of 60 minutes and the mean RGB intensities of 50 particles that remain in focus for the duration of the experiment, are plotted as a function of time in Figure 5.7. The vertical axis units are normalized with the respective maximum value for each data series for visualization purposes. The R value exhibits stronger fluctuations in time, compared to the G and B values. However, the fluctuations do not seem to suggest a bleaching of the TLC material. On the other hand, the G and B signals do show a gradual weakening of their scattering intensity of approximately $4-5$ %, during the 60 min exposure, which is not substantial and would minimally affect their temperature calibration. In any case, the bleaching does not affect the results presented in this study since all the TLC particles used to produce the results presented in this report were illuminated for time periods in the order of a few seconds.

5.3. Uncertainty Analysis

The performance of the temperature estimation obtained with the calibration approach described in Section 5.1 was evaluated for several TLC materials, with temperature response ranges of 1 K, 5 K, 10 K, 20 K at magnifications, M, of $20\times$ and $10\times$. Since the real temperatures of the particles detected during the calibration scans is known, an outlier detection procedure was implemented in order to ignore spurious color values beyond a specific threshold, calculated as follows. Outliers were determined by segregating valid particle images as those whose color values, respective to the variable space being used for the calibration, lay within an Euclidean distance of 0.1 color units from a smooth calibration curve, calculated by interpolating the mean color values of the particles detected at all temperatures covered in the calibration scan. This method was chosen because the dynamic ranges of all color variables considered in this analysis are in the same order of magnitude (see Figure 5.2), hence a constant threshold value for the determination of outliers seems like a reasonable criteria to segregate valid estimated temperatures in all cases.

The standard deviation of the estimated temperature from the true value, σ, given by

$$\sigma = \sqrt{\frac{1}{N}\sum_{i=1}^{N}(T_i - T_{\text{real}})^2} \tag{5.2}$$

was calculated for each step of the calibration scan, where N is the number of particles detected at each step and T_i are the estimated temperatures of valid detected particles. Figures 5.8-5.17 show red scatter plots of all the valid particles' estimated temperatures, T_{meas}, plotted against their real temperature, T_{real}. The standard deviation from the true value (referred to as the uncertainty in the following discussion), σ, is also plotted in Figures 5.8-5.17, as black crosses, for the full span of temperatures covered in each calibration scan. The left vertical axis of the plots shows two unit scales, namely $^{\circ}$C and % of the respective calibration temperature ranges, in order to allow for each calibration approach's uncertainty evaluation in both absolute and relative terms. A text box at the top of each plot states the nominal temperature response range of the TLC material in question, the magnification used to make the recordings during the calibration scan, the focal length of the cylindrical lens mounted in front of the camera (if one was used), and

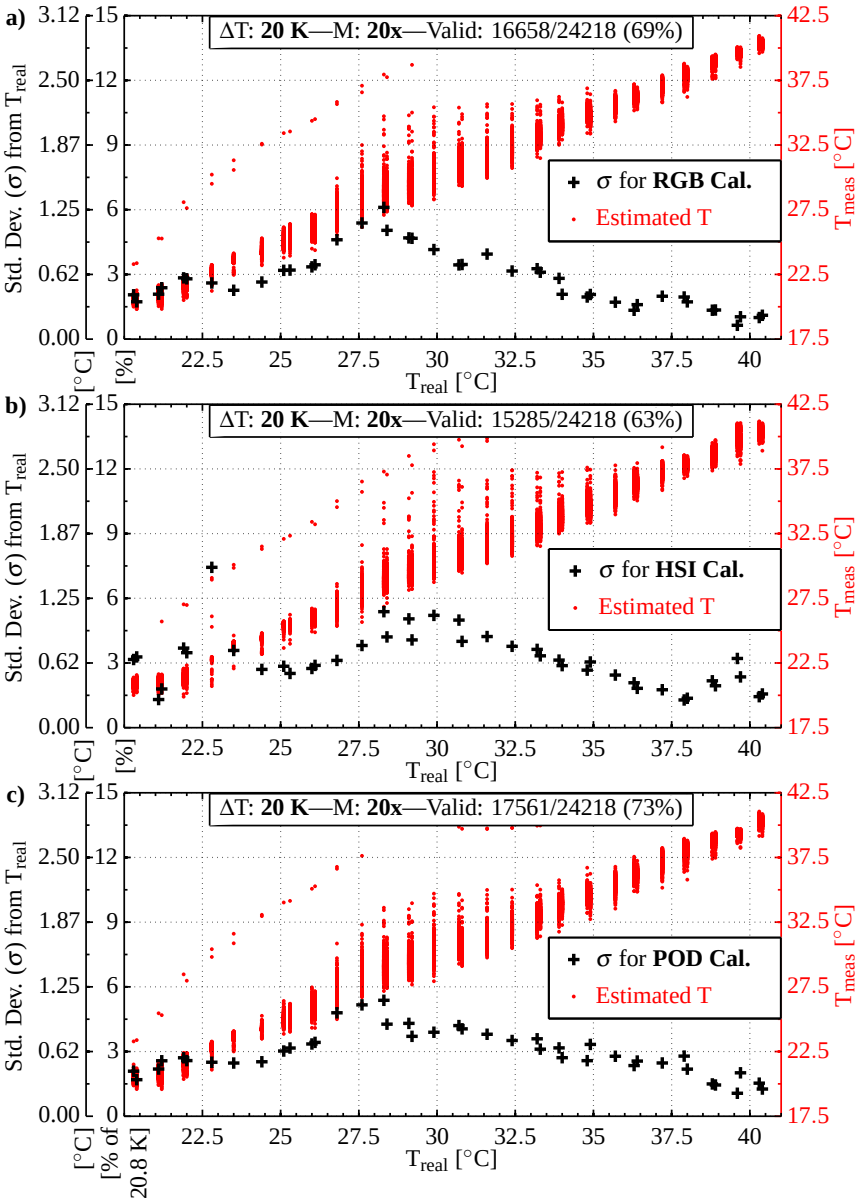

Figure 5.8.: Red points: valid particles' estimated temperature. Black crosses: standard deviation from the true value in absolute and relative units. Temperature calibration for a) RGB, b) HSI, and c) POD color data for Hallcrest R20C20W TLC particles. Nominal $\Delta T = 20$ K, $M = 20\times$.

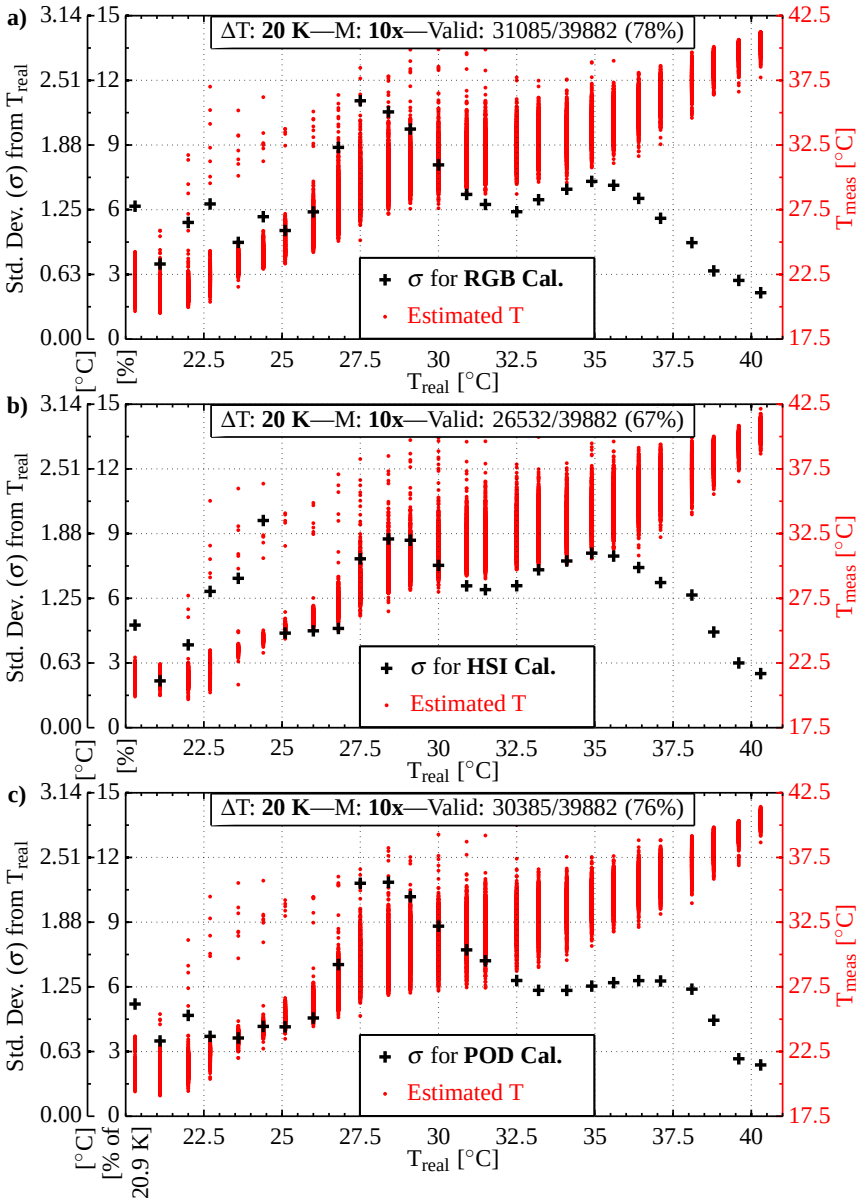

Figure 5.9.: Red points: valid particles' estimated temperature. Black crosses: standard deviation from the true value in absolute and relative units. Temperature calibration for a) RGB, b) HSI, and c) POD color data for Hallcrest R20C20W TLC particles. Nominal $\Delta T = 20$ K, $M = 10\times$.

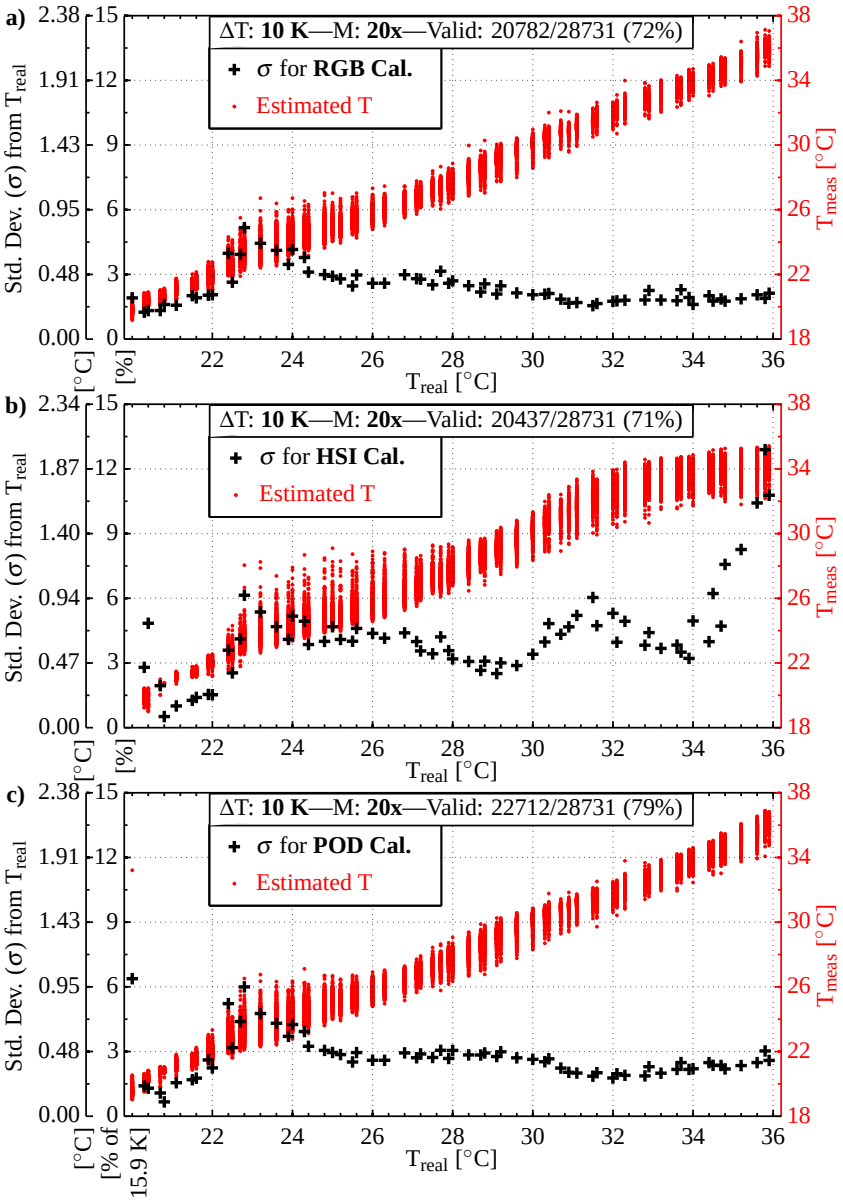

Figure 5.10.: Red points: valid particles' estimated temperature. Black crosses: standard deviation from the true value in absolute and relative units. Temperature calibration for a) RGB, b) HSI, and c) POD color data for Hallcrest R20C10W TLC particles. Nominal $\Delta T = 10$ K, $M = 20\times$.

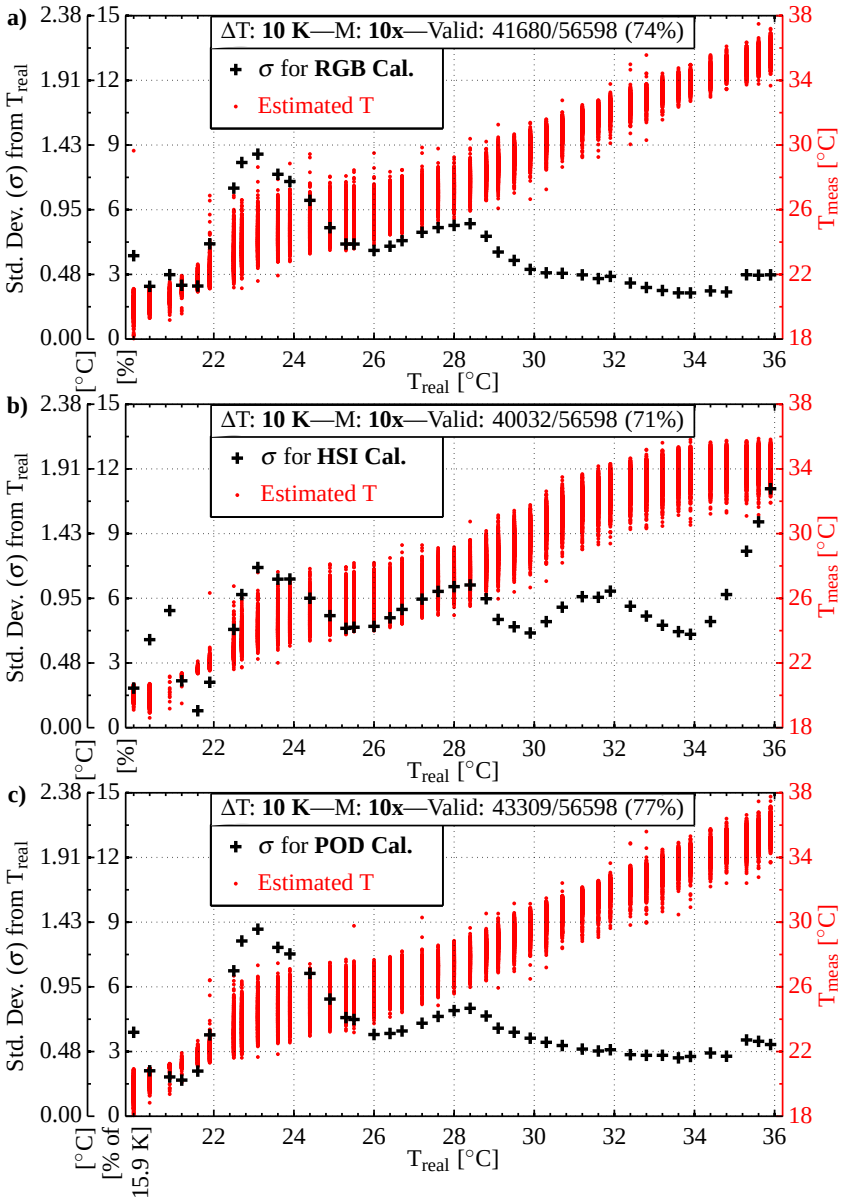

Figure 5.11.: Red points: valid particles' estimated temperature. Black crosses: standard deviation from the true value in absolute and relative units. Temperature calibration for a) RGB, b) HSI, and c) POD color data for Hallcrest R20C10W TLC particles. Nominal $\Delta T = 10$ K, $M = 10\times$.

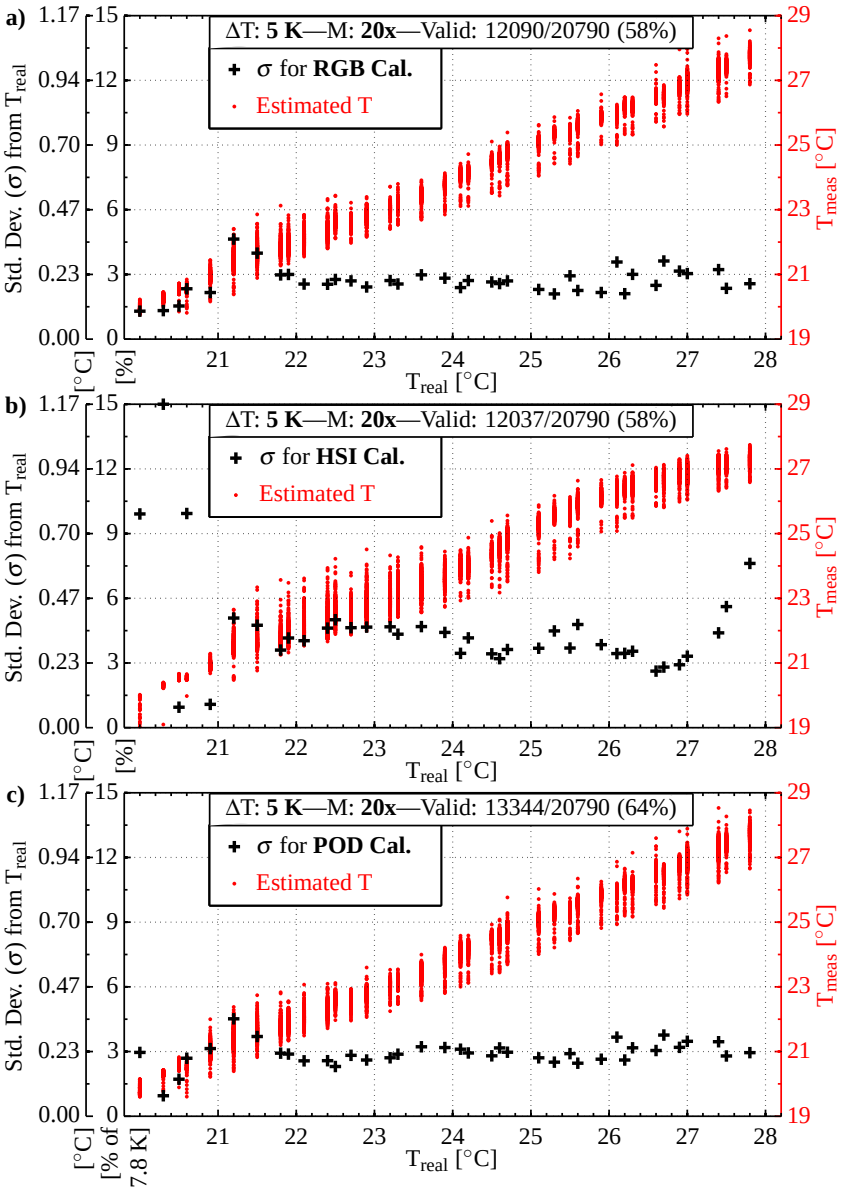

Figure 5.12.: Red points: valid particles' estimated temperature. Black crosses: standard deviation from the true value in absolute and relative units. Temperature calibration for a) RGB, b) HSI, and c) POD color data for Hallcrest R20C5W TLC particles. Nominal $\Delta T = 5$ K, $M = 20\times$.

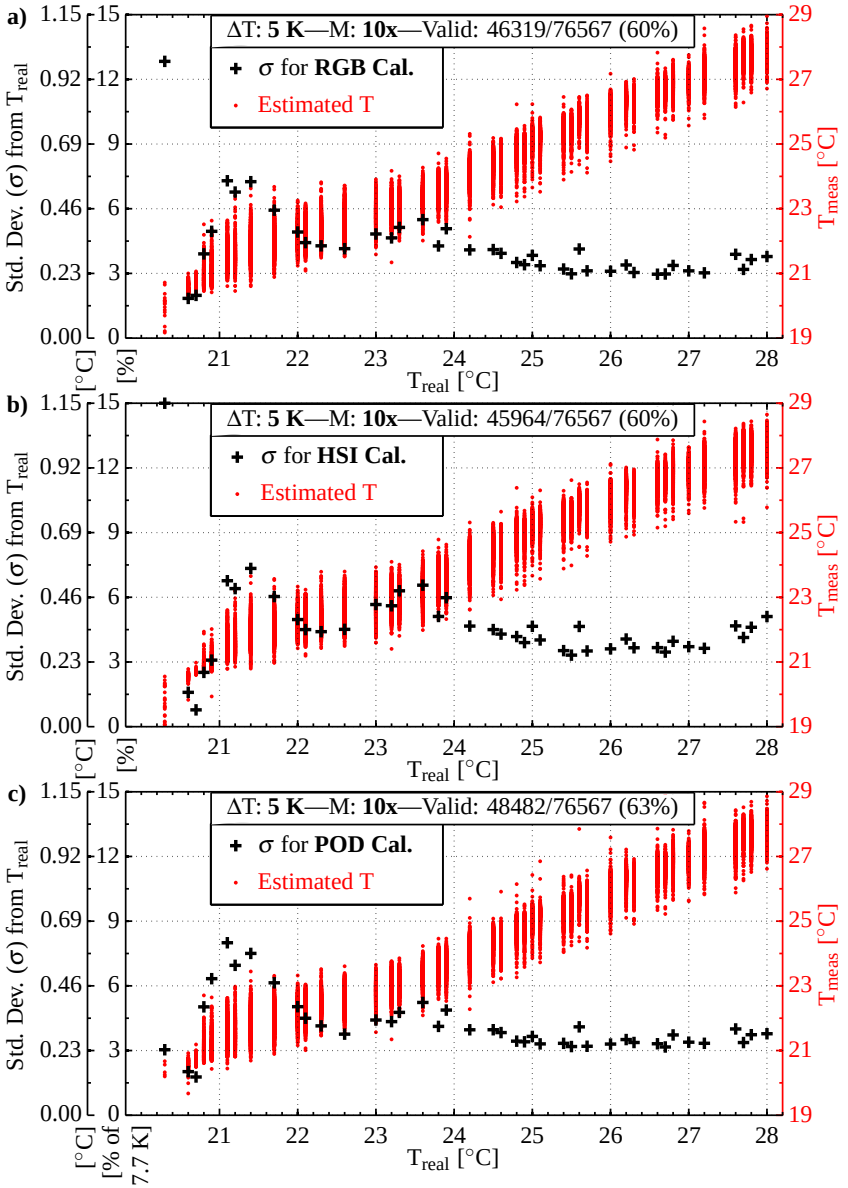

Figure 5.13.: Red points: valid particles' estimated temperature. Black crosses: standard deviation from the true value in absolute and relative units. Temperature calibration for a) RGB, b) HSI, and c) POD color data for Hallcrest R20C5W TLC particles. Nominal $\Delta T = 5$ K, $M = 10\times$.

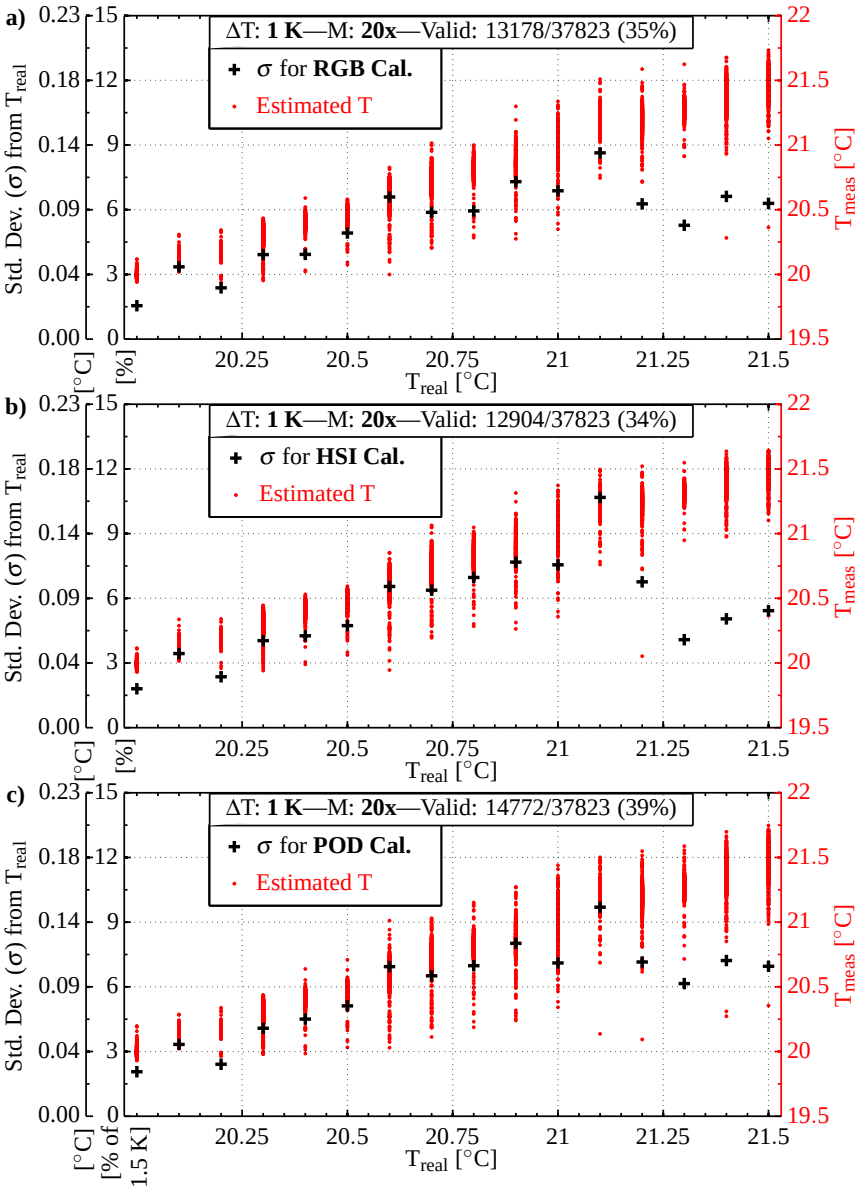

Figure 5.14.: Red points: valid particles' estimated temperature. Black crosses: standard deviation from the true value in absolute and relative units. Temperature calibration for a) RGB, b) HSI, and c) POD color data for Hallcrest R20C1W TLC particles. Nominal $\Delta T = 1$ K, $M = 20\times$.

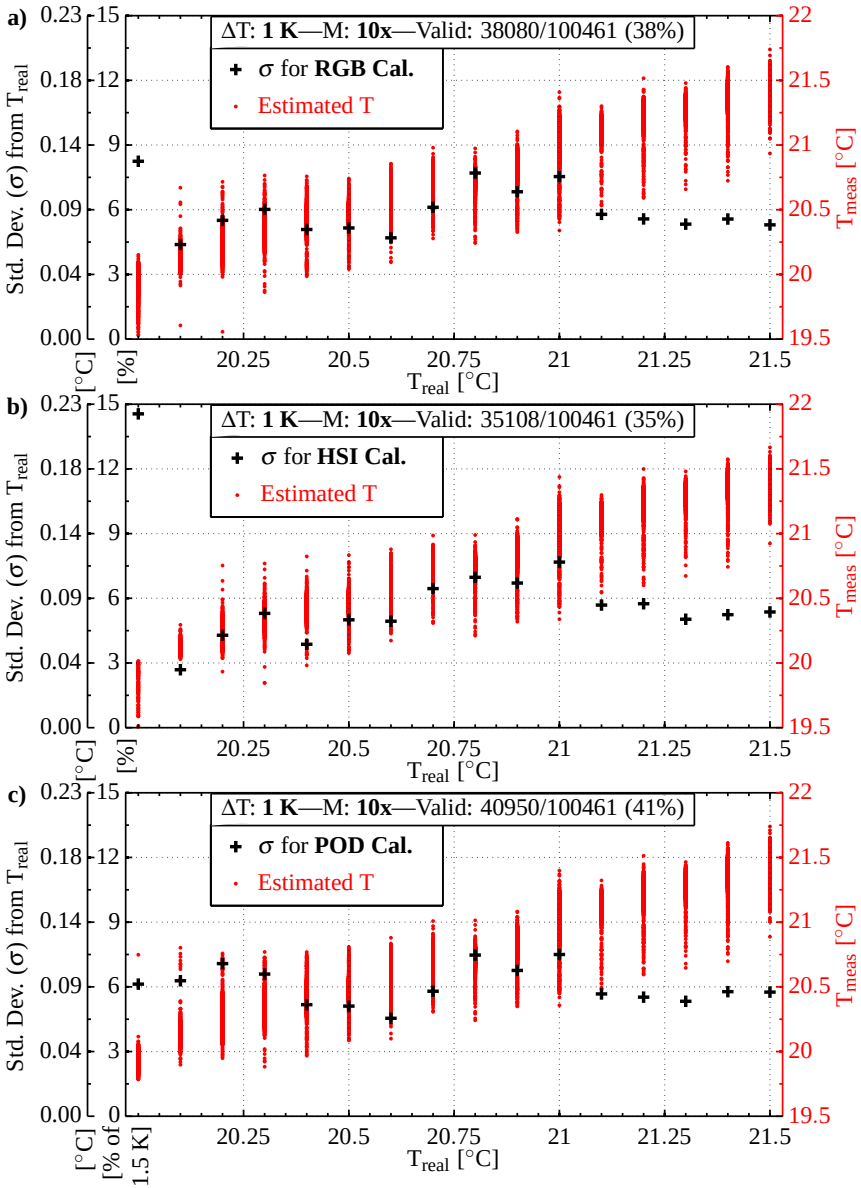

Figure 5.15.: Red points: valid particles' estimated temperature. Black crosses: standard deviation from the true value in absolute and relative units. Temperature calibration for a) RGB, b) HSI, and c) POD color data for Hallcrest R20C1W TLC particles. Nominal $\Delta T = 1$ K, $M = 10\times$.

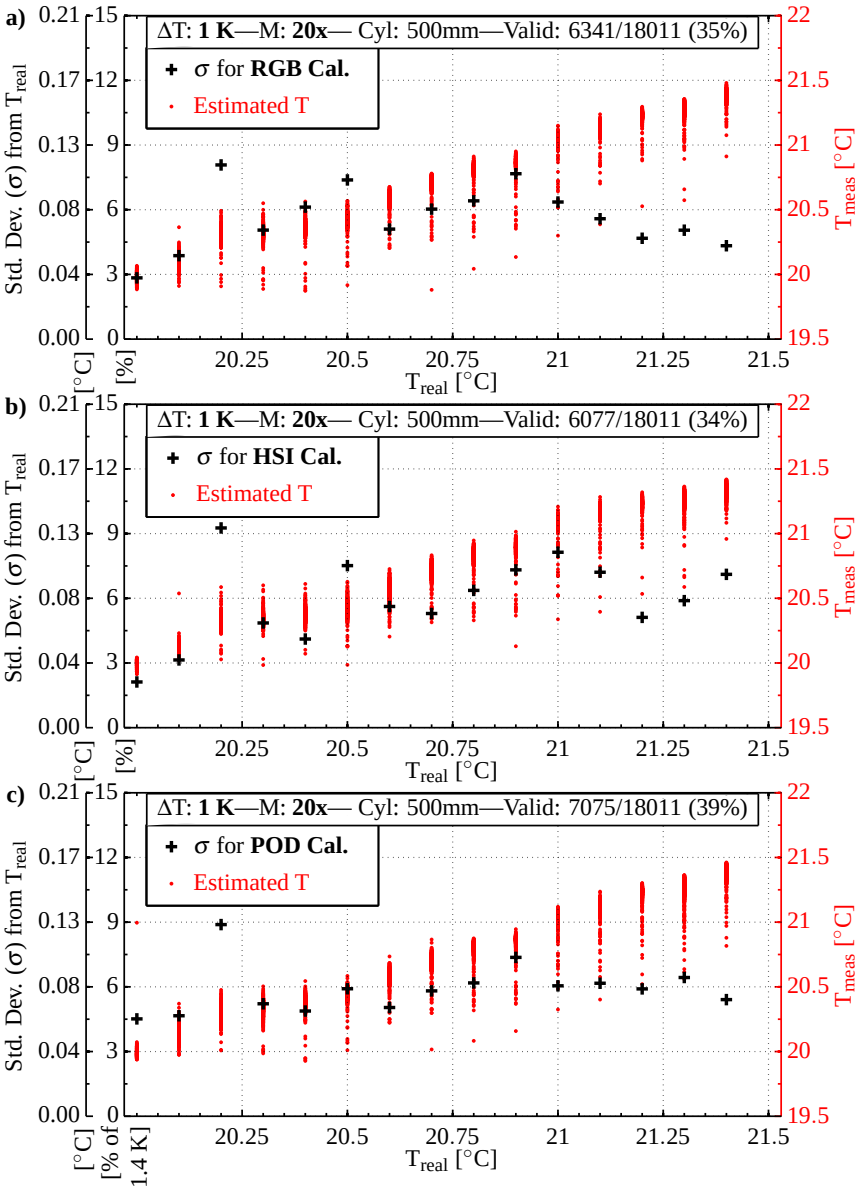

Figure 5.16.: Red points: valid particles' estimated temperature. Black crosses: standard deviation from the true value in absolute and relative units. Temperature calibration for a) RGB, b) HSI, and c) POD color data for Hallcrest R20C1W TLC particles. Nominal $\Delta T = 1$ K, $M = 20\times$, $f_{cyl} = 500$ mm.

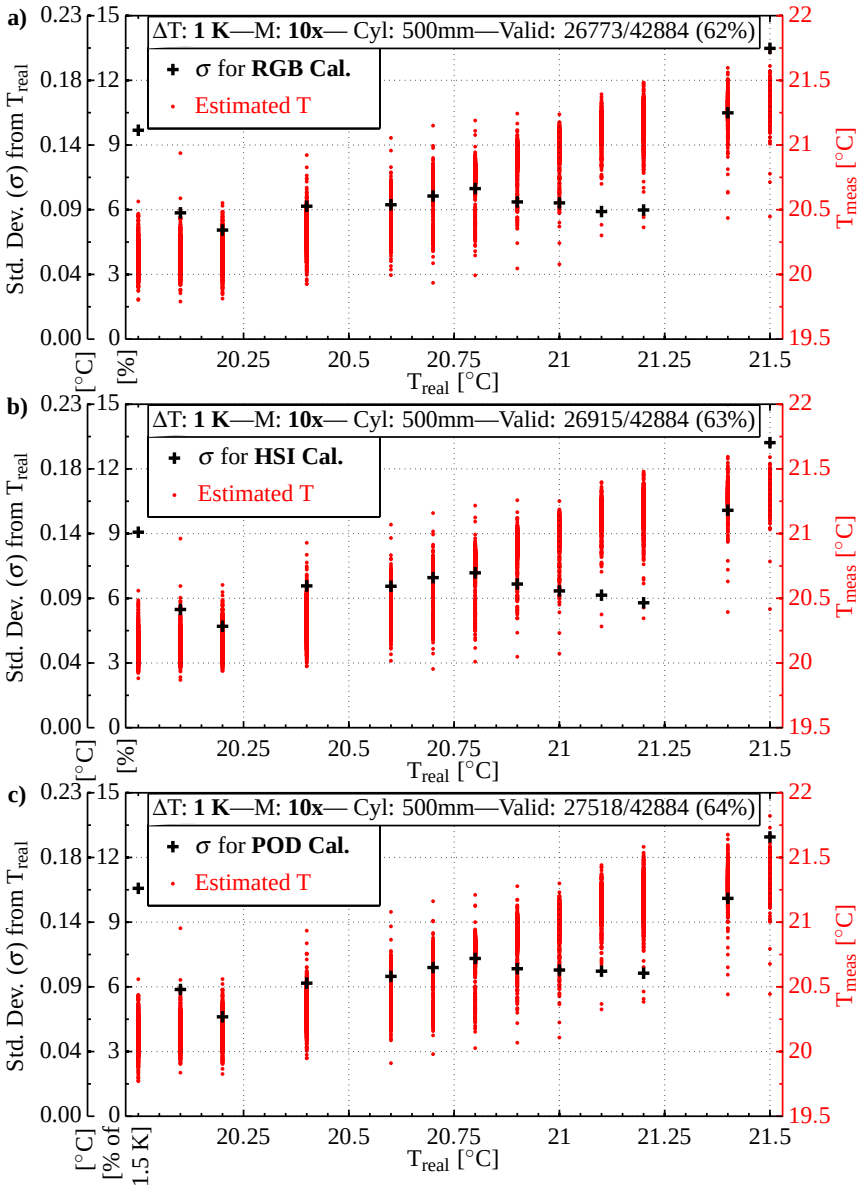

Figure 5.17.: Red points: valid particles' estimated temperature. Black crosses: standard deviation from the true value in absolute and relative units. Temperature calibration for a) RGB, b) HSI, and c) POD color data for Hallcrest R20C1W TLC particles. Nominal $\Delta T = 1$ K, $M = 10\times$, $f_{cyl} = 500$ mm.

the number of particles deemed as valid by the outlier detection scheme outlined above. It is clear from the plots in Figures 5.8-5.15 that the calibration procedure allows for the correct determination of the particles' temperature. However, the uncertainty, normalized with the temperature response range of the TLC material, varies for the different materials, and is higher for the Hallcrest R20C1W particles, with a nominal response range of 1 K, than for the TLC materials with broader temperature response ranges. The signal-to-noise ratio (SNR) of the color images acquired using the polarization filter and the Lumencor Spectra X light engine was high enough to detect particle images with a magnification as low as $10\times$, over a broader temperature span than the one quoted as the nominal temperature response range of the TLC materials. However, the error is higher for the $10\times$ magnification in most cases, probably due to the fact that the particle images are smaller, and defocusing effects play a stronger role in the color signals of the detected particles. Figures 5.8 and 5.9 show some data that strongly deviates from the correct temperature estimation trend. These outliers correspond to a few particles (approximately 1 out of 300) whose color behavior differs from that of the other particles. This can be due to a damage in the molecular structure of the material and the author regards such particles as faulty probes that do not affect the performance of the method due to the low frequency in which they appear. The detection of these outliers is not a trivial task given that their temperature is not known in a real experiment and they display valid color values for a different temperature.

The temperature calibration with the POD variable space appears to be more robust than the calibrations using the RGB and HSI color variables, considering it uses two calibration variables, as opposed to three, and yields comparable or lower uncertainty values than the other two in all cases. The calibration using the HSI data consistently underestimates the temperature of the particles when they reach a blue color at higher temperatures, and generally yields higher error values at low temperatures as well. Using the RGB data yields similar error values as the POD calibration in most cases, even though it uses three, as opposed to two calibration variables. This serves as confirmation of Roesgen & Totaro (2002)'s statement that the optimal decorrelation of the RGB data, via POD, yields calibration variables that are better suited to obtain a reversible relationship with temperature. Figures 5.16-5.17 show the calibration performance for the TLC material with a temperature response of 1 K, with a 500mm cylindrical lens mounted in front of the 3-CCD color camera. The ability of the measurement technique to evaluate the color of elliptical particle images in order to estimate their temperature does not seem to be negatively affected by the fact that the images are defocused with an astigmatic aberration. The uncertainty of the calibration oscillates around 6% using the POD color variables. Even though this uncertainty levels are not low, the measurement technique is viable to make time-resolved measurements of the 3D position and temperature of TLC particles in a microscopic flow, as will be shown in Chapter 6.

6. Temperature and Displacement Tracking in a Cooling Droplet

In order to evaluate the feasibility of TLC Thermography, combined with APTV, to real-life applications, a test case was necessary in which the TLC particles show a measurable displacement in the z-direction as well as an evident change in color caused by a temperature gradient in the flow. Since the z-component estimation of the particles' location in the flow volume, using the current state-of-the-art imaging system, yielded high uncertainty values using a magnification of $10\times$, all measurements of a real flow field were made with a magnification of $20\times$. Now, the ideal case would have been to measure a constant temperature gradient over a known distance in a microscopic geometry that drives a 3D flow. However, the construction of a device that can drive such flow while holding a controlled temperature gradient over a distance of 352 μm (corresponding to the field of view at $20\times$ magnification) is not a trivial task and an alternative test case was chosen.

Instead of a constant temperature gradient, the flow inside a droplet as it cools down to room temperature was measured, as schematically shown in Figure 6.1. The experiment was carried out in a temperature controlled laboratory, with the temperature of the room set to 19 °C. The temperature of the room oscillated around the temperature set on the thermostat with the oscillations reaching magnitudes of up to ~ 1 K. The convective streams coming from the ventilation outlets of the room were perceivable to the people in the room so the droplet was shielded with a rudimentary cardboard chamber to minimize the air temperature fluctuations around it. A thermocouple was installed in the vicinity of the droplet and temperature fluctuations were still detected inside the cardboard chamber, with amplitudes of approximately 0.3 °C. The droplet was seeded with Hallcrest R20C1W TLC particles, with a temperature response range of 1 K, and a red start temperature of 20 °C. Warm air was blown at the droplet until the particles images became blue and the temperature inside the cardboard chamber read 21.5 °C. Images of the flow were then acquired at rate of 2.2 Hz until the temperature in the chamber went under

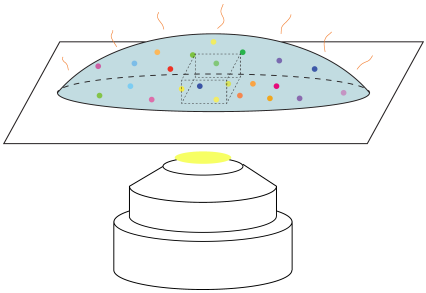

Figure 6.1.: Schematic of cooling drop experiment.

20 °C, and the particles no longer reflected detectable colors.

The experiment was initially performed without a cylindrical lens. A series of images, at constant time intervals during the cooling of the droplet are shown in Figure 6.2.

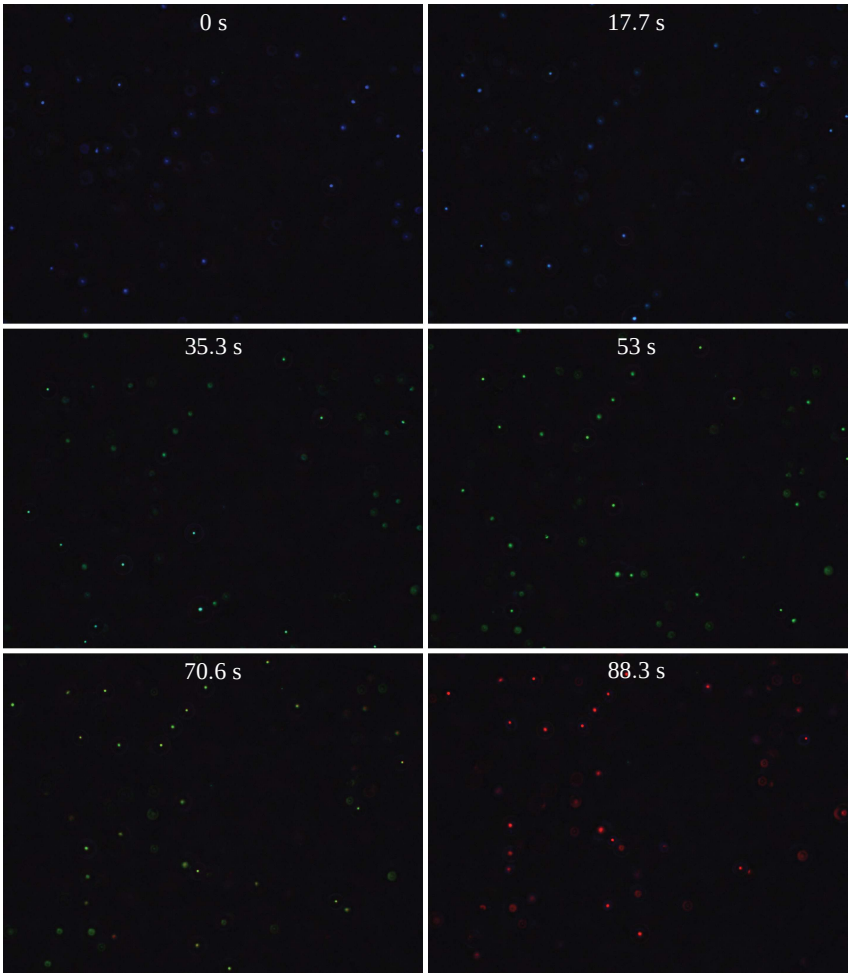

Figure 6.2.: Sample image series of the flow inside a cooling droplet acquired with 20× magnification.

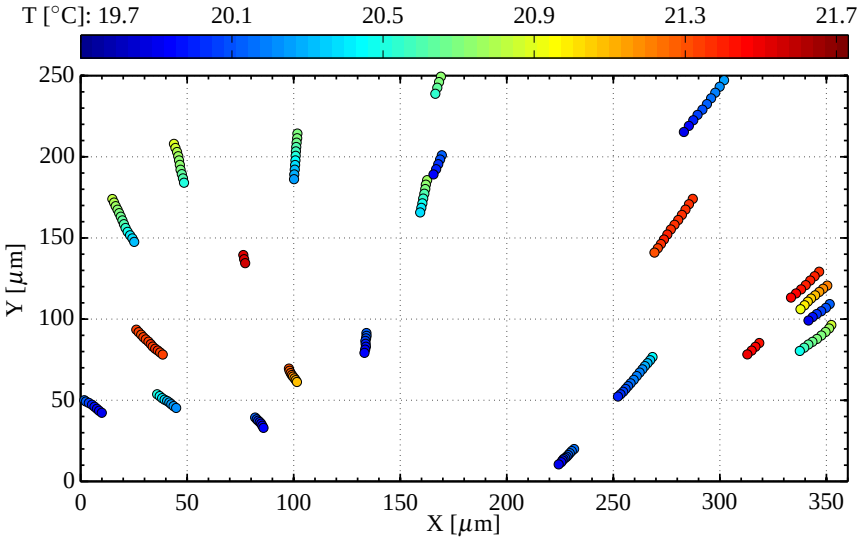

Figure 6.3.: TLC particle 2D motion inside a droplet, as it cools to room temperature.

The warm air blown around the droplet induces some convective flow inside it which the TLC particles follow while they cool down to room temperature and gradually change their color from blue to red. The flow is three-dimensional and the particle images become blurry over time as they distance themselves from the focal plane and become undetectable. In-focus particle images were detected using the image processing scheme outlined in Appendix A and their temperature was estimated using the system matrix calibration approach discussed in Section 5.1 on the proper orthogonally decomposed (POD) RGB data, calculated as explained in Section 2.2. Since the seeding density was not high, a nearest neighbor approach (Malik et al. 1993) was implemented to track the motion of the particles, using the detected particle images' (x,y) positions over time, and reconstruct their trajectories. Figure 6.3 shows a plot of particle tracks for particles whose images were properly detected in more than 5 consecutive frames, such that a trajectory could be reconstructed, with the temperature of the particles given by the color map. The time frame of individual trajectories is independent of the others, hence they do not necessarily begin and end simultaneously. All trajectories detected during the time it took for the droplet to cool down are plotted in the figure but the reader should note that trajectories with different colors correspond to particles detected during different times of the cooling process. The temperature calibration function is able to resolve the temperature decrease of individual particles as the droplet cools down, allowing for a lagrangian analysis of the flow's temperature for the first time using tracer particles. These data only provide a 2D reconstruction of the particles motion, even though a depth component of velocity is clearly evident to the naked eye, when watching the image series as a motion picture.

This is why the APTV method was used to evaluate the third component of the particles' displacement and reconstruct the 3D trajectories of the particles motion.

The same measurement was made with a cylindrical lens (focal length of 500 mm) installed in front of the camera. A series of images, at constant time intervals during the

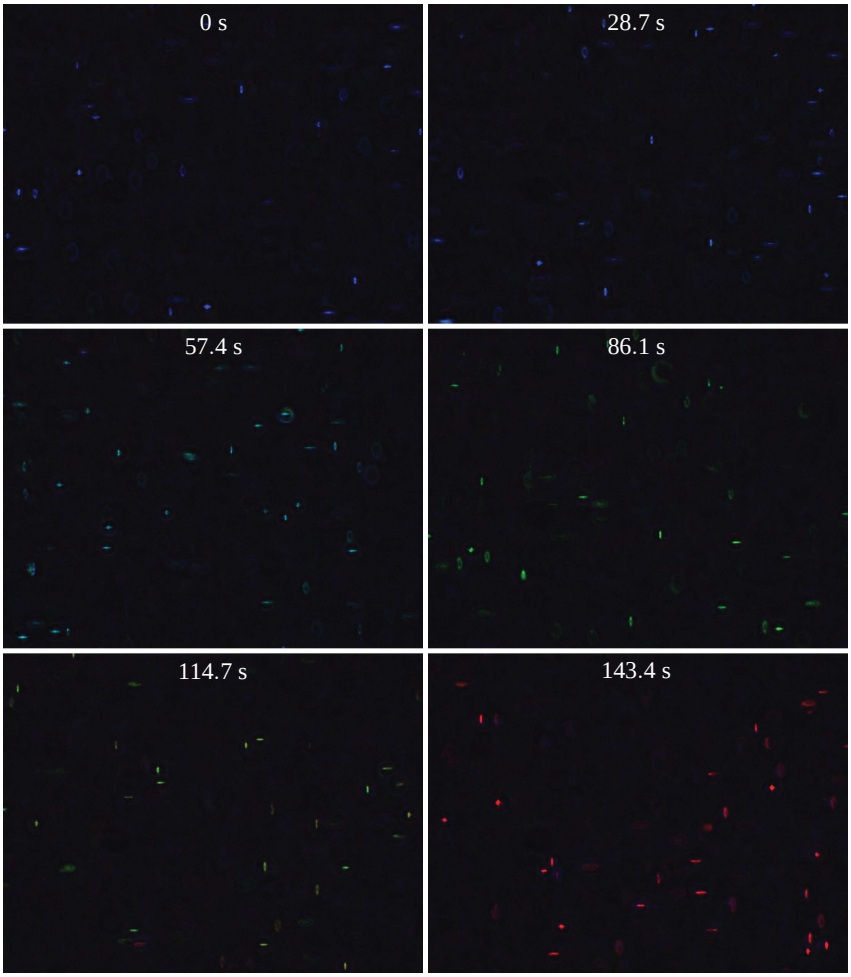

Figure 6.4.: Sample image series of the flow inside a cooling droplet acquired with 20× magnification and a cylindrical lens with a focal length of 500 mm.

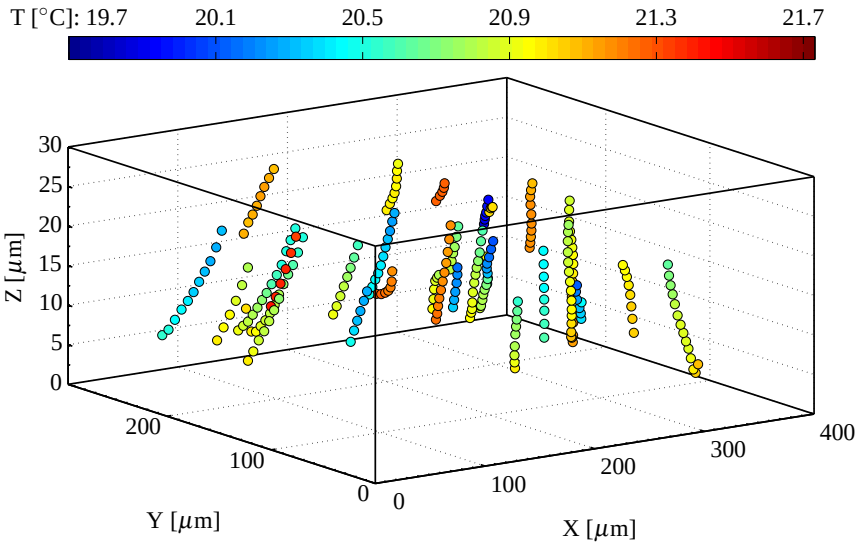

Figure 6.5.: TLC particle 3D motion inside a droplet, as it cools to room temperature.

cooling of the droplet are shown in Figure 6.4. Like the experiment described above, without a cylindrical lens, particle images were detected with the detection scheme outlined in Appendix A, and the temperature of the particles was estimated using the system matrix calibration approach discussed in Section 5.1 on the proper orthogonally decomposed (POD) RGB data. The geometry of the elliptical particle images, on the other hand, was used to estimate the z-positions of the particles using the z-calibration method discussed in Section 4.2 and a nearest neighbor approach (Malik et al. 1993) was implemented to track the 3D motion of the particles, using the detected particle images' (x, y, z) positions over time, and reconstruct their trajectories. Figure 6.5 shows a 3D plot of particle tracks for particles whose images were properly detected in more than 5 consecutive frames, such that a trajectory could be reconstructed, with the temperature of the particles given by the color map. Once again, the time frame of individual trajectories is independent of the others, hence they do not necessarily begin and end simultaneously. All trajectories detected during the time it took for the droplet to cool down are plotted in the figure but the reader should note that trajectories with different colors correspond to particles detected during different times of the cooling process. The temperature calibration function is able to resolve the temperature decrease of individual particles as the droplet cools down, in this case allowing for a 3D lagrangian analysis of the flow's temperature for the first time using tracer particles. Moreover, the particles clearly have a considerable velocity in the z-direction, as they migrate up and inwards, as if following

some recirculation pattern. This depth component of displacement was, of course, not measured without astigmatism, which leaves a substantial bias in the 2D tracking of the particles' motion.

6.1. Considerations and technological limitations

The author performed other experiments to illustrate the functionality of the measurement technique but controlled temperature gradients in slow enough flows are not straightforward in such small dimensions and no satisfactory results were obtained. The reader should note that even though the current state of technology did allow for the successful 3D tracking of TLC particles along with their temperature in a cooling droplet, limitations remain to be overcome in order to extend the applicability of the method to more complex microfluidics problems where higher velocities and weaker temperature gradients need to be resolved. Among the many challenges that must be overcome, the most prominent are the following:

- The maximum frame rates and dynamic ranges offered by state-of-the-art low-noise 3CCD color cameras place a low cap on the velocity ranges that can be evaluated, as well as the amount of defocusing that can be applied. Therefore, the flow in impinging jets or colliding fronts, which would be exemplary test cases for the method, cannot be characterized at this time.

- White light sources with a homogeneous spectrum remain far less powerful than lasers, making the intensity of detected particle images, especially defocused ones, substantially lower than that of fluorescent particles in conventional APTV experiments. This translates into a limitation of the measurement volume's depth to only a few tenths of microns, with $20\times$ magnification, given that not enough light is scattered at lower magnification to make real-life experiments with a low enough measurement uncertainty. More light means brighter particle images. Ergo, strongly defocused particles that are undetectable using the current illumination scheme will be detected when more powerful light sources become available. With an expansion of the measurement volume of $3-4\times$ the current value, experimental setups using standard microchannels ($50-100\mu m$ deep) can be designed to produce controlled temperature gradients that can be evaluated.

- The design and production of non-encapsulated TLC particles for these applications is a young research field and there is room for much improvement in the fabrication of smaller particles with lower amounts of surfactant that can better follow complex flows and have brighter color cores. Even though the fabrication procedure of the non-encapsulated TLC particles used in this study yields high quality color images, the portion of the particles that scatters color is proportionally small relative to the size of the particles. This can be a product of the amount of surfactant

used to stabilize the emulsion containing the TLC particles and more optimal production parameters are probably possible, which yield smaller non-encapsulated particles that scatter more colored light. On the other hand, the bigger the particles the stronger their interactions with each other, which at higher concentration and low Reynolds numbers can interfere with their ability to follow the flow that is evaluated.

In any case, better hardware is available continuously and the overcoming of these limitations is only a matter of time. That being said, the groundwork for a powerful method to simultaneously reconstruct 3D velocity and temperature fields in microscopic flows is laid out and proof of its functionality has been presented.

6.2. Future outlook

There are several fields where a temperature field characterization is missing to complete interesting studies of fluid transport in microscopic flows. Kumar et al. (2011), for instance, performed a Lagrangian analysis of an electrothermal microvortex and measured its toroidal velocity distribution, which led to validation of simplistic models and the further understanding of the interaction between the laser beam and the microfluidic device. As its name says, the fluid phenomenon investigated in this case is a product of an induced temperature gradient which has not been measured. Needless to say, the ability to reconstruct the temperature field in this flow would shed light on the forces that drive the vortex and probably fuel improvements to its applications in the rapid transport of particles via electrokinetic patterning.

On a different note, Marangoni flows play an important part in the engineering of photonic materials, thin coatings, deposition in thin fluid films, and crystal growth, among other fields. Yet, many open questions remain regarding its driving forces and even its existence in pure water, as well as the impact that environmental conditions and surface contaminants have on its behavior. Marangoni flow is basically a transport of fluid caused by a gradient in surface tension, generated by a composition or temperature variation along the free surface of the liquid. Hu & Larson (2005) presented an analytical study of the Marangoni flow in an evaporating sessile droplet. They developed a finite element method to resolve the thermal field as the droplet evaporates and calculated the time-dependent velocity fields within it. Xuefeng & Luo (2007) presented experimental evidence of what appears to be a redirection pattern at the contact line of an evaporating water droplet. They seeded the flow with fluorescent nano-particles and followed their approach towards the contact line followed by their migration away from it. However, a 3D reconstruction was not presented in their report, given that the particles became defocused as they moved away from the contact line and there was no way to tell their motion in the depth direction. Xuefeng & Luo (2007) stated that their observations indicated a monotonic temperature variation along the free surface of the droplet but, off course, they did not have the means to measure it. An experiment in an evaporating water

droplet was attempted using non-encapsulated TLC particles but the amount of surfactant in the TLC-containing emulsion seemed to annul the Marangoni effect and no discernable temperature gradient was detected. This remains a good test case for a future time when production solutions are found regarding the fabrication of smaller TLC micro particles and the temperature estimation uncertainty of the method is further decreased to the order of such temperature gradients.

7. Conclusion and Outlook

The combination of Thermo-Liquid Crystal (TLC) Thermography and Astigmatism particle Tracking Velocimetry (APTV), along with other technological advances in experimental measurement techniques, allows for the simultaneous measurement of the three-dimensional (3D) temperature and velocity fields of microscopic flows. After many years of research and progress in the fields of TLC thermography and optical velocimetry, the technology has become available to record high quality color images of TLC micro particles, whose position and temperature can be tracked in 3D using defocused color particle images by means of astigmatic aberrations.

The first step in the process of making this measurement method a reality was the fabrication of stable non-encapsulated TLC micro spheres, to replace the commonly encapsulated TLC particles that are reported in most other reports of TLC thermography in fluids. A manufacturing process known as Shirasu Porous Glass (SPG) membrane emulsification process was used to produce a water based emulsion of stable non-encapsulated micro spheres with a narrower size distribution than that available in commercial encapsulated TLC particle solutions (see Section 3.1). These non-encapsulated particles not only have a narrow size distribution but also lack a polymer shell which is why their images have homogeneous intensity profiles without internal color patterns, making their detection, as well as the evaluation of their color at specific temperatures, possible with lower uncertainty levels.

In principle, it is possible to detect the color of the particle images generated by these non-encapsulated using conventional imaging systems. However, the illumination sources that are usually used for TLC thermography experiments do not shine a homogeneous light spectrum and have peaks at certain wavelengths. What happens with these white light sources is that particles at narrow ranges of temperatures scatter substantially stronger colors than at others, making the detection of the weak colors a challenging task, not to mention the temperature calibration. Fortunately, with the accelerating rate of technology newer illumination systems become available regularly and a 'light engine' using light pipes that shine different wavelength ranges is currently available commercially. This device provides a more homogeneous spectrum with enough power to record color images of TLC particles of all visible colors with comparable intensities. On top of that, TLCs exhibit a very convenient physical property. When the liquid crystals enter their chiral-nematic phase, they begin to scatter circularly polarized light of select wavelength ranges as a function of their temperature. The chirality of the circular polarization, however, is independent of the incoming light's nature. This particular feature of TLCs allows for background noise filtering in images of flow seeded with TLC particles, fur-

ther increasing the contrast and color quality of the particle images. A custom circular polarization filter was then designed and fabricated and, as expected, the quality of the color images improved considerably (see Section 3.2).

A cylindrical lens was then mounted in the system in order to evaluate the feasibility of introducing astigmatic aberrations to the images, in order to apply Astigmatism Particle Tracking Velocimettry (APTV) to track the motion of the particles in 3D. Elliptical images were successfully detected and a calibration procedure was implemented to estimate the depth position of the particles in a flow volume. The calibration approach was successful in achieving this task, although the uncertainty values are higher than those reported in the literature for experiments with fluorescent particles. However, the reader should note that fluorescent filtering has been a standard technique for a long time and very efficient filters are available commercially, which provide very high signal-to-noise ratios (SNR). On the other hand, the achromatic quarter wave plate used for background filtering in the circular polarization filter, does not transmit perfectly polarized light for all wavelengths and the filtering in general is not as good as with fluorescence. Nevertheless, it provides high enough quality images to detect the geometry and color of even highly defocused particle images, which allows for the tracking of the particles' motion and temperature simultaneously for the first time.

In the past, the relationship between hue and temperature has been the most prominent approach to estimate the temperature from the color of TLCs. However, a calibration approach using more than a single variable was evaluated in this study, which yields a better performance that the traditional temperature-Hue relationship. The approach was implemented using three color spaces, as calibration variables, namely RGB, HSI and POD. POD stands for the proper orthogonally decomposed RGB data, which is a set of optimally uncorrelated variables that provide a more robust way of temperature calibration. Four different TLC materials with different temperature response ranges were calibrated in order to assess their feasibility for real life applications.

The TLC material with a temperature response range of 1 K was then used to track the motion and temperature of the TLC particles as they followed the convective flow inside a cooling droplet. The results prove that the measurement technique is capable of resolving 3D temperature gradients, in both time and space, in microscopic flows.

The uncertainty values vary for different TLC materials, being higher for materials with narrower temperature response ranges. Fortunately the method has plenty of room for improvements in multiple fronts. First of all, there is not much research in the manufacturing of non-encapsulated particles such as the ones used for this study. The performance of the method has a wide margin of improvement if solutions with lower amounts of surfactant were developed. The surface properties and wettability of the particles could also be engineered to provide particles that scatter brighter colors. On the other hand, better circular polarization filtering can also play a role in the acquisition of higher-quality particle images. the same can be said for illuminations sources. Today, newer and more powerful illumination devices are becoming available regularly, which can significantly improve the results reported in this document. Lastly, the detection algorithms and calibration

schemes can also be perfected further. A substantial portion of the performance of the calibration approaches, relies on the particle image detection schemes and the algorithms that carry them out. Higher-quality images, along with improved methods to detect their color and their geometry, would go a long way in improving the estimation of both the depth position and temperature of the particles.

LIST OF REFERENCES

ABBATE G, TKACHENKO V, MARINO A, VITA F, GIOCONDO M & DE STEFANO L (**2007**). *Optical characterization of liquid crystals by combined ellipsometry and half-leaky-guided-mode spectroscopy in the visible-near infrared range*. Journal of Applied Physics 101:073,105, DOI: 10.1063/1.2714768

ABDULLAH N, ABU TALIB AR, JAAFAR AA, MOHD SALLEH MA & CHONG WT (**2010**). *The basics and issues of thermochromic liquid crystal calibrations*. Experimental Thermal and Fluid Science 34:1089–1121, DOI: 10.1016/j.expthermflusci.2010.03.011

ADAMS JE, HAAS W & WYSOCKI J (**1969**). *Optical properties of certain cholesteric liquid-crystal films*. Journal of Chemical Physics 50:2458–2464, DOI: 10.1063/1.1671402

AKINO N, KUNUGI T, ICHIMIYA K, MITSUSHIRO K & UEDA M (**1989**). *Improved liquid-crystal thermometry excluding human color sensation*. Journal of Heat Transfer 111:558–565

AZAR K & FARINA DJ (**1997**). *Measuring chip temperature with thermochromic liquid crystals*. Electronics Cooling Magazine 3

BASSON M & POTTEBAUM TS (**2012**). *Measuring the temperature of fluid in a microchannel using thermochromic liquid crystals*. Experiments in Fluids 53:803–814, DOI: 10.1007/s00348-012-1326-0

BAUGHN JW (**1995**). *Liquid crystal methods for studying turbulent heat transfer*. International Journal of Heat and Fluid Flow 16:365–375

BEDNARZ TP, LEI C & PATTERSON JC (**2010**). *Various aspects of camera settings and image processing in the calibration of thermo-chromic liquid crystals for accurate particle image thermometry measurements*. Journal of Visualization 13:241–250, DOI: 10.1007/s12650-010-0038-x

BEHLE M, SCHULZ K, LEINER W & FIEBIG M (**1996**). *Color-based image processing to measure local temperature distributions by wide-band liquid crystal thermography*. Applied Scientific Research 56:113–143

BERREMAN DW & SCHEFFER TJ (**1970**a). *Bragg reflection of light from single-domain cholesteric liquid-crystal films*. Physical Review Letters 25:577–581

BERREMAN DW & SCHEFFER TJ (**1970**b). *Bragg reflection of light from single-domain cholesteric liquid-crystal films: Errata*. Physical Review Letters 25:902

BERREMAN DW & SCHEFFER TJ (**1970**c). *Reflection and transmission by single-domain cholesteric liquid crystal films: Theory and verification*. Molecular Liquid Crystals and Liquid Crystals 11:395–405, DOI: 10.1080/15421407008083530

BHARARA M, COBB JE & CLAREMONT DJ (**2008**). *Thermography and thermometry in the assessment of diabetic neuropathic foot: A case for furthering the role of thermal techniques*. Lower Extremity Wounds 5:250–260

BRILL MH (**1998**). *How the CIE 1931 color-matching functions were derived from Wright-Guild data - Erratum*. Color Research & Application 23:259

BROSTOW W (**1990**). *Properties of polymer liquid crystals: Choosing molecular structures and blending*. Polymer 31:979–995, DOI: 10.1016/0032-3861(90)90242-Q

BROWN PK & WALD G (**1964**). *Visual pigments in single rods and cones of the human retina*. Science 144:45–52

CHAUDHARI AM, WOUDENBERG MT, ALBIN M & GOODSON KE (**1998**). *Transient liquid crystal thermometry of microfabricated PCR vessel arrays*. Journal of Microelectromechanical Systems 7:345–355

CHEN GS & YEH HC (**2012**). *Polarization-selective color-filter Fresnel lens in polymer-stabilized cholesteric liquid crystals*. Journal of Applied Physics 112:054,501, DOI: 10.1063/1.4750042

CHEN S, ANGARITA-JAIMES N, ANGARITA-JAIMES D, PELC B, GREENAWAY AH, TOWERS CE, LIN D & TOWERS DP (**2009**). *Wavefront sensing for three-component three-dimensional flow velocimetry in microfluidics*. Experiments in Fluids 47:849–863, DOI: {10.1007/s00348-009-0737-z}

CHIN Y, LAKSHMINARASIMHAN MS, LU Q, HOLLINGSWORTH DK & WITTE LC (**2002**). *Convective heat transfer in vertical asymmetrically heated narrow channels*. Journal of Heat Transfer 124:1019–1025, DOI: 10.1115/1.1497356

CHUNG JW, GRIGOROPOULOS CP & GREIF R (**2003**). *Infrared thermal velocimetry in MEMS-based fluidic devices*. Journal of Microelectromechanical Systems 12:365–372, DOI: {10.1109/JMEMS.2003.811753}

CIERPKA C & KÄHLER CJ (**2012**). *Particle imaging techniques for volumetric three-component (3D3C) velocity measurements in microfluidics*. Journal of Visualization 15:1–31, open access, DOI: 10.1007/s12650-011-0107-9

CIERPKA C, SEGURA R, HAIN R & KÄHLER CJ (**2010**). *A simple single camera 3C3D velocity measurement technique without errors due to depth of correlation and spatial averaging for microfluidics*. Measurement, Science & Technology 21:045,401, DOI: 10.1088/0957-0233/21/4/045401

CIERPKA C, ROSSI M, SEGURA R & KÄHLER CJ (**2011**a). *On the calibration of astigmatism particle tracking velocimetry for microflows*. Measurement, Science & Technology 22:015,401, DOI: 10.1088/0957-0233/22/1/015401

CIERPKA C, TSCHULIK K, SEGURA R, UHLEMANN M & KÄHLER CJ (**2011**b). *Zeitaufgelöste 3D3K Geschwindigkeitsfeldmessungen mit der fernmikroskopischen*

Astigmatismus PTV zur Analyse der elektrochemischen Kupferabscheidung. Technisches Messen 78:232–238, DOI: 10.1524/teme.2011.013

CIOFALO M, SIGNORINO M & SIMIANO M (**2003**). *Tomographic particle-image velocimetry and thermography in Rayleigh-Bernard convection using suspended thermochromic liquid crystals and digital image processing*. Experiments in Fluids 34:156–172

COPPETA J & ROGERS C (**1998**). *Dual emission laser induced fluorescence for direct planar scalar behavior measurements*. Experiments in Fluids 25:1–15

COWLEY JM (**1995**). Diffraction physics 3rd revised edition. Elsevier Science B. V., DOI: ISBN0-444-10791-6

CUKUREL B, SELCAN C & ARTS T (**2012**). *Color theroy perception of steady wide band liquid crystal thermometry*. Experimental Thermal and Fluid Science 39:112–122, DOI: 10.1016/j.expthermflusci.2012.01.015

DABIRI D (**2009**). *Digital particle image thermometry/velocimetry: a review*. Experiments in Fluids 46:191–241, DOI: 10.1007/s00348-008-0590-5

DABIRI D & GHARIB M (**1991**). *Digital particle image thermometry: The method and implementation*. Experiments in Fluids 11:77–86

DREHER R & MEIER G (**1971**). *Selective reflection by cholesteric liquid crystals*. Molecular Crystals and Liquid Crystals 13:17–26

DREHER R & MEIER G (**1973**). *Optical properties of cholesteric liquid crystals*. Physical Review A: General Physics 6:1616–1623

FAIRMAN HS, BRILL MH & HEMMENDINGER H (**1997**). *How the CIE 1931 color-matching functions were derived from Wright-Guild data*. Color Research & Application 22:22–23

FARINA DJ (**1995**). *Making surface temperature measurements using liquid crystal thermography*. Electronics Cooling Magazine 1

FERGASON JL (**1964**). *Liquid crystals*. Scientific American 211:77–85

FERGASON JL (**1966**). *Cholesteric structure - 1 optical properties*. Molecular Crystals 1:293–307

FUCHS T, HAIN R & KÄHLER C (**2014**). *Three-dimensional location of micrometer-sized particles in macroscopic domains using astigmatic aberrations*. Optics Letters 39:1298–1301, DOI: 10.1364/OL.39.001298

FUJISAWA N & FUNATANI S (**2000**). *Simultaneous measurement of temperature and velocity in a turbulent thermal convetion by the extended range scanning liquid crystal visualization technique*. Experiments in Fluids Suppl.:S158–S165

FUJISAWA N & HASHIZUME Y (**2001**). *An uncertainty analysis of temperature and velocity measured by a liquid crystal visualization technique*. Measurement Science & Technology 12:1235–1242

FUJISAWA N, NAKAJIMA T, KATOH N & HASHIZUME Y (**2004**). *An uncertainty analysis of temperature and velocity measured by stereo liquid-crystal thermometry and velocimetry*. Measurement Science & Technology 15:799–806, DOI: 10.1088/0957-0233/15/5/004

FUJISAWA N, FUNATANI S & KATOH N (**2005**). *Scanning liquid-crystal thermometry and stereo velocimetry for simultaneous three-dimensional measurement of temperature and velocity field in a turbulent Rayleigh-Bernard convection*. Experiments in Fluids 38:291–303, DOI: 10.1007/s00348-004-0891-2

FUNATANI S & FUJISAWA N (**2002**). *Simultaneous measurement of temperature and three velocity components in planar cross section by liquid-crystal thermometry combined with stereoscopic particle image velocimetry*. Measurement Science & Technology 13:1187–1205

GLEESON HF & COLES HJ (**1989**). *Optical properties of chiral nematic liquid crystals*. Molecular Crystals and Liquid Crystals 170:9–34

GUILD J (**1931**). *The colorimetric properties of the spectrum*. The Royal Society of London Series A 230:149–187

HAY JL & HOLLINGSWORTH DK (**1996**). *A comparison of trichromic systems for use in the calibration of polymer-dispersed thermochromic liquid crystals*. Experimental Thermal and Fluid Science 12:1–12

HAY JL & HOLLINGSWORTH DK (**1998**). *Calibration of micro-encapsulated liquid crystals using hue angle and a dimensionless temperature*. Experimental Thermal and Fluid Science 18:251–257

HÖHMANN C & STEPHAN P (**2002**). *Microscalse temperature measurement at an evaporating liquid meniscus*. Experimental Thermal and Fluid Science 26:157–162

HOHREITER V, WERELEY ST, OLSEN MG & CHUNG JN (**2002**). *Cross-correlatioin analysis for temperature measurement*. Measurement Science & Technology 13:1072–1078

HU H & LARSON RG (**2005**). *Analysis of the effects of Marangoni stresses on the microflow in an evaporating sessile droplet*. Langmuir 21:3972–3980, DOI: 10.1021/la0475270

IRELAND PT & JONES TV (**1987**). *The response time of a surface thermometer employing encapsulated thermochromic liquid crystals*. Journal of Physics E: Scientific Instruments 20:1195–1199

JOBLOVE GH & GREENBERG D (**1978**). *Color spaces for computer graphics*. In: ACM SIGGRAPH 5th Annual Conference on Computer Graphics and Interactive Techniques, New York, USA, August

JOSCELYNE SM & TRÄGÅRDH G (**2000**). *Membrane emulsification - a literature review*. Journal of Membrane Science 169:107–117, DOI: 10.1016/S0376-7388(99)00334-8

KUMAR A, CIERPKA C, WILLIAMS SJ, KÄHLER CJ & WERELEY ST (**2011**). *3D3C velocimetry measurements of an electrothermal microvortex using wavefront deformation PTV and a single camera*. Microfluidics and Nanofluidics 10:355–365, DOI: 10.1007/s10404-010-0674-4

LEE SJ & KIM S (**2009**). *Advanced particle-based velocimetry techniques for a microscale flows*. Microfluidics and N 6:577–588, DOI: DOI10.1007/s10404-009-0409-6

LINDKEN R, ROSSI M, GROSSE S & WESTERWEEL J (**2009**). *Micro-Particle Image Velocimetry (μPIV): Recent developments, applications, and guidelines*. Lab on a Chip 9:2551–2567

LUTJEN PM, MISHRA D & PRASAD V (**2001**). *Three-dimensional visualization and measurement of temperature field using liquid crystal scanning thermography*. Journal of Heat Transfer 123:1006–1014, DOI: 10.1115/1.1370514

MALIK N, DRACOS T & PAPANTONIOU D (**1993**). *Particle Tracking Velocimetry in 3-Dimensional flows. 3. Particle Tracking*. Experiments in Fluids 15:279–294

MAXWELL JC (**1855**). *Experiments on color, as perceived by the eye, with remarks on colour-blindness*. Transactions of the Royal Society of Edimburgh 24:275–298

MELAMED L & RUBIN D (**1971**). *Selected optical properties of misxtures of cholesteric liquid crystals*. Applied Optics 10:1103–1107, DOI: 10.1364/AO.10.001103

MERZKIRCH W (**1987**). Flow Visualization 2nd Edition. Academic Press

MICHALSKI L, ECKERSDORF K, KUCHARSKI J & MCGHEE J (**2001**). Temperature Measurement 2nd Edition. Wiley

MISHRA D, LUTJEN PM, CHEN QS & PRASAD V (**2000**). *Tomographic reconstruction of three-dimensional temperature field using liquid crystal scanning thermography*. Experimental Heat Transfer 13:235–258

MITCHELL BS (**2004**). An introduction to materials engineering and science for chemical and materials engineering. John Wiley & Sons Inc.

MULLER PB, ROSSI M, MARIN AG, BARNKOB R, AUGUSTSSON P, LAURELL T, KÄHLER CJ & BRUUS H (**2013**). *Ultrasound-induced acoustophoretic motion of microparticles in three dimensions*. Physical Review E p 023006

MUWANGA R & HASSAN I (**2006**a). *Local heat transfer measurements in a curved microsurface using liquid crystal thermography*. Journal of Thermophysics and Heat Transfer 20:884–894, DOI: 10.2514/1.17907

MUWANGA R & HASSAN I (**2006**b). *Local heat transfer measurements in microchannels using liquid crystal thermography: methodology development and validation*. Journal of Heat Transfer 128:617–626, DOI: 10.1115/1.2193541

MUWANGA R & HASSAN I (**2007**). *A flow boiling heat transfer investigation of FC-72 in a microtube using liquid crystal thermography*. Journal of Heat Transfer 129:977–987, DOI: 10.1115/1.2728905

MYERS HP (**2009**). Introductory solid state physics 2nd edition. Taylor & Francis, DOI: ISBN0-7484-0660-3

NAKASHIMA T, SHIMIZU M & KUKIZAKI M (**1992**). *Membrane emulsification by microporous glass*. Key Engineering Materials 61-62:513–516, DOI: 10.4028/www.scientific.net/KEM.61-62.513

NASAREK R (**2010**). *Temperature field measurement with high spatial and temporal resolution using liquid crystal thermography and laser induced fluorescence*. PhD thesis, Technische Universität Darmstadt

OLSEN MG & ADRIAN RJ (**2000**). *Out-of-focus effects on particle image visibility and correlation in microscopic particle image velocimetry*. Experiments in Fluids 29:S166–S174

OSEEN CW (**1933**). *The theory of liquid crystals*. Transactions of the Faraday Society 29:883–900

OSWALD P & PIERANSKI P (**2005**). Nematic and cholesteric liquid crystals. Taylor & Francis

OTSU N (**1979**). *A thershold selection method from gray-level histograms*. IEEE Transactions on Systems, Man, and Cybernetics 9:62–66

PARK HG, DABIRI D & GHARIB M (**2001**). *Digital particle image velocimetry/thermometry and application to the wake of a heated circular cylinder*. Experiments in Fluids 30:327–338, DOI: 10.1007/s003480000199

PARSLEY M (**1991**). *Handbook of thermochromic liquid crystal technology*. Hallcrest, Glenview, Il

PEREIRA F & GHARIB M (**2002**). *Defocusing digital particle image velocimetry and the three-dimensional characterization of two-phase flows*. Measurement Science & Technology 13

PRATT WK (**2007**). Digital image processing fourth edition. Wiley & Sons, Inc.

RAFFEL M, WILLERT CE, WERELEY ST & KOMPENHANS J (**2007**). Particle image velocimetry: a practical guide. Springer Verlag

RAO Y & ZANG S (**2010**). *Calibrations and the measurement uncertainty of wide-band liquid crystal thermography*. Measurement Science & Technology 21:015,105, DOI: 10.1088/0957-0233/21/1/015105

ROBERTS GT & EAST RA (**1996**). *Liquid crystal thermography for heat transfer measurement in hypersonic flows: a review*. Journal of Spacecraft and Rockets 33:761–768

ROESGEN T & TOTARO R (**2002**). *A statistical calibration technique for thermochromic liquid crystals*. Experiments in Fluids 33:732–734, DOI: 10.1007/s00348-002-0525-5

ROSSI M, CIERPKA C, SEGURA R & KÄHLER CJ (**2011**). *Volumetric reconstruction of the 3D boundary of stream tubes with general topology using tracer particles*. Measurement, Science & Technology 22:105,405, DOI: 10.1088/0957-0233/22/10/105405

RUSS JC (**2002**). The Image Processing Handbook. CRC, Boca Raton

SABATINO DR, PRAISNER TJ & SMITH CR (**2000**). *A high-accuracy calibration technique for thermochromic liquid crystal temperature measurements*. Experiments in Fluids 28:497–505

SAGE I (**2011**). *Thermochromic liquid crystals*. Liquid Crystals 38:1551–1561, DOI: 10.1080/02678292.2011.631302

SAKAKIBARA J & ADRIAN (**1999**). *Whole field measurement of temperature in water using two-color laser induced fluorescence*. Experiments in Fluids 26:7–15, DOI: 10.1007/s003480050260

SAKAKIBARA J & ADRIAN R (**2004**). *Measurement of temperature field of a Rayleigh-Bernard convection using two-color laser-induced fluorescence*. Experiments in Fluids 37:331–340, DOI: DOI10.1007/s00348-004-0821-3

SANTIAGO JG, WERELEY ST, MEINHART CD, BEEBE DJ & ADRIAN RJ (**1998**). *A particle image velocimetry system for microfluidics*. Experiments in Fluids 25:316–319

SEGURA R, CIERPKA C, ROSSI M, JOSEPH S, BUNJES H & KÄHLER CJ (**2013**). *Non-encapsulated thermo-liquid crystals for digital particle tracking thermography/velocimetry in microfluidics*. Microfluidics and Nanofluidics 14:445–456, open access, DOI: 10.1007/s10404-012-1063-y

SMITH CR, SABATINO DR & PRAISNER TJ (**2001**). *Temperature sensing with thermochromic liquid crystals*. Experiments in Fluids 30:190–201

SMITH T & GUILD J (**1931**). *The C.I.E. colorimetric standards and their use*. Transactions of the Optical Society 33:73–134, DOI: 10.1088/1475-4878/33/3/301

SOMEYA S, BANDO S, SONG Y, CHEN B & NISHIO M (**2005**). *Delif measurement of ph distribution around dissolving co2 droplet in high pressure vessel*. International journal of heat and mass transfer 48:2508–2515

SOMEYA S, YOSHIDA S, LI Y & OKAMOTO K (**2009**). *Combined measurement of velocity and temperature distributions in oil based on the luminescent lifetimes of seeded particles*. Measurement Science & Technology 20

SOMEYA S, LI Y, ISHII K & OKAMOTO K (**2011**). *Combined two-dimensional velocity and temperature measurements of natural convection using a high-speed camera and temperature-sensitive particles*. Experiments in Fluids 50:65–73, DOI: 10.1007/s00348-010-0894-0

STASIEK J (**1997**). *Thermochromic liquid crystals and true colour image processing in heat transfer and fluid flow research*. Heat and Mass Transfer 33:27–39

STASIEK J, STASIEK A, JEWARTOWSKI M & COLLINS MW (**2006**). *Liquid crystal thermography and true-colour digital image processing*. Optics & Laser Technology 38:243–256

STASIEK JA & KOWALEWSKI TA (**2002**). *Thermochromic liquid crystals applied for heat transfer research*. Opto-Electronics Review 10:1–10

SUN Y, DUTHALER S & NELSON BJ (**2004**). *Autofocusing in computer microscopy: Selecting the optimal focus algorithm*. Microscopy Research and Technique 65:139–149

VEJRAZKA J & MARTY P (**2007**). *An alternative technique for the interpretation of temperature measurements using thermochromic liquid crystals*. Heat Transfer Engineering 28:154–162, DOI: 10.1080/01457630601023641

VOGT J & STEPHAN P (**2012**). *Using microencapsulated fluorescent dyes for simultaneous measurement of temperature and velocity fields*. Measurement Science & Technology 23:105,306, DOI: 10.1088/0957-0233/23/10/105306

DE VRIES H (**1951**). *Rotatory power and other optical properties of certain liquid crystals*. Acta Crystallographica 4:219–226

WALD G (**1964**). *The receptors of human color vision*. Science 145:1007–1016

WERELEY ST & MEINHART CD (**2010**). *Recent Advances in Micro-Particle Image Velocimetry*. Annual Review of Fluid Mechanics 42:557–576, DOI: {10.1146/annurev-fluid-121108-145427}

WILLIAMS SJ, PARK C & WERELEY ST (**2010**). *Advances and applications on microfluidic velocimetry techniques*. Microfluidics and Nanofluidics 8:709–726, DOI: {10.1007/s10404-010-0588-1}

WOZNIAK G, WOZNIAK K & SIEKMANN J (**1996**). *Non-isothermal flow diagnostics using microencapsulated cholesteric particles*. Applied Scientific Research 56:145–156

WRIGHT WD (**1929**a). *A re-determination of the mixture curves of the spectrum*. Transactions of the Optical Society of London 30:141–164

WRIGHT WD (**1929**b). *A re-determination of the trichromatic coefficients of the spectral colours*. Transactions of the Optical Society 30:141–164

XUEFENG X & LUO J (**2007**). *Marangoni fflow in an evaporating water droplet*. Applied Physics Letters 91:124,102, DOI: 10.1063/1.2789402

YOON SY & KIM KC (**2006**). *3D particle position and 3D velocity field measurement in a microvolume via the defocusing concept*. Measurement Science & Technology 17:2897–2905

YOUNG T (**1802**). *On the theory of light and colours*. Philosophical Transactions of the Royal Society of London 92:12–48

ZINK H & VAN DAEL W (**1993**). *Selective reflection in the cholesteric and blue pphase of a chiral-racemic mixture of CE6*. Liquid 14:603–609, DOI: 10.1080/02678299308027738

Appendices

A. Image Processing

A series of preprocessing steps were implemented to improve the contrast of the TLC particles' color images. Even though a circular polarization filter was mounted to acquire the images used for the calibration of the *z*-position and the temperature of the TLC particles, as well as to track the flow inside a cooling droplet, the quarter-wave plate does not transmit perfectly circularly polarized light for all wavelengths and some background noise is still transmitted. The detection of particle images, especially the heavily defocused ones recorded with APTV, requires a high signal-to-noise ratio (SNR) which can be considerably improved by using background removal methods. After careful evaluation of several different methods to improve the contrast of the color images and remove their background noise, the following approach yielded the best particle image detection performance for a variety of color particle images with a broad range of defocused geometries.

- A morphological operation was performed on the raw images (see Figure A.1a), consisting of an erosion- followed by a dilation algorithm, both of which used a flat, disk-shaped structuring element with a defined radius which was chosen depending on the size and shape of the particle images (different radii were chosen for different magnifications and cylindrical lens arrangements). The product of this morphological operation acts as a smooth dark image, with the topology of the background noise levels in the raw color image as shown in Figure A.1b.

- This background image was them subtracted from the raw RGB image, nearly eliminating completely the background noise surrounding the particle images, while their colors remain bright and vibrant, as shown in Figure A.1c.

- In order to detect the perimeters of the particles, a segmentation algorithm will be used but the grayscale intensity profiles of the particles images in Figure A.1c remain noisy and the determination of a segmentation threshold that works on particle images of different colors and shapes is difficult to find under these conditions. Therefore, a smoothing gaussian filter is applied to the color images in order to reduce the noise in the intensity profiles of the particle images, which yields the image shown in Figure A.1d.

These high-contrast images with smooth intensity profiles are used to detect the general shape of the particle images before a sub-pixel boundary detection algorithm is implemented on the raw images to accurately determine the (x,y) location of the particles,

as well as the horizontal and vertical axis of elliptical particle images, (a_x, a_y), when APTV is used. Once the general shape of the particle images is determined, their RGB intensity values, which are used later for the temperature calibration procedure, are also calculated. This process of particle image geometry and color determination is carried out in the following fashion.

A basic segmentation filter is applied to the smooth high-contrast images generated with the preprocessing steps outlined above (see Figure A.1d). This filter simply converts

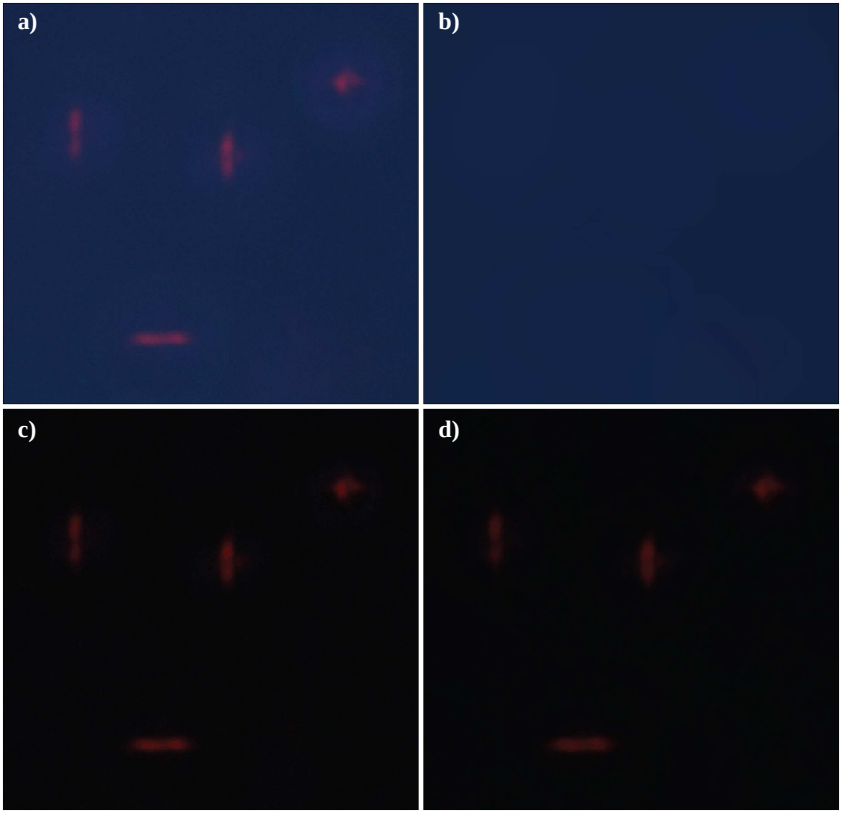

Figure A.1.: a) Raw RGB image. b) Raw RGB image's background. c) High-contrast RGB image after background subtraction. d) Smooth image used for segmentation.

the color images to grayscale and binarizes them using a count threshold, chosen through an iterative process, testing images that contain particles of different colors and shapes. Automatic approaches to determine the optimal segmentation threshold for each image were attempted but the detection performance yield varied substantially from one image to the next. For instance, an automatic segmentation threshold was calculated for each grayscale image, maximizing the separability of its black and white values as proposed by Otsu (1979). Even though this method works well for particle images of certain colors, it failed almost entirely for other color. Hence, a constant segmentation threshold was

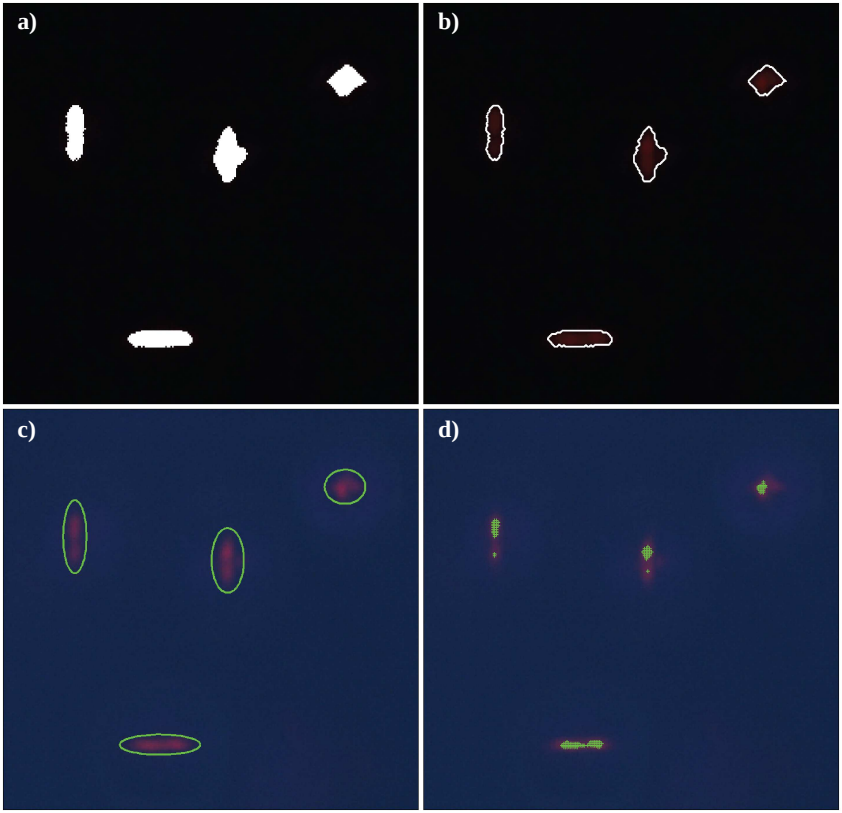

Figure A.2.: a) Segmented particle image areas. b) Segmented particle image perimeters. c) Particle images' elliptical shapes calculated with sub-pixel accuracy. d) Pixels used to calculate the mean RGB values of particle images.

used and a consistent detection performance was achieved for particles of all colors and shapes. Figure A.2a shows the result of the segmentation filter applied to the image in Figure A.1d and Figure A.2b shows the perimeter of the particle image areas shown in Figure A.2a, found with the segmentation filter.

These segmented pixel regions are used next to determine the (x,y) locations of the particles, as as well as the horizontal and vertical axis of elliptical particle images, (a_x, a_y), with sub-pixel accuracy. Rectangular windows, with dimensions corresponding to twice the maximum width and height of the segmented particles regions, were used to calculate a 2D Gaussian fit of the raw RGB particle images, converted to grayscale. The variance values of the fit in both dimensions were used as the vertical and horizontal axes, (a_x, a_y), of the elliptical particle images and the center of the fit's mean determined the (x,y) location of the particle's center. Figure A.2c shows the raw RGB image with plots of the elliptical boundaries of the particle images, calculated with the 2D gaussian fit approach described above.

Lastly, several schemes were evaluated to determine the RGB values of each particle image. The first was to use the RGB values of the pixel where the centroid of the segmented area of each particle image lies. Unfortunately, the particle images are not symmetric and occasionally exhibit dark patterns as they become defocused, which caused a broad scatter of color values for particles that were recorded at the exact same temperature. The same happened when using the pixel containing the center point of the ellipses calculated with the sub-pixel algorithm explained above. An alternative method was to try the mean of a group of pixels contained within a certain radius of either the centroid of the segmented area or the center point of the ellipse. This method yielded better results for in-focus circular particle images but not for elliptical ones mainly due to the fact that some of the pixels in the group would occasionally lie in the dark patterns of the particle image, throwing off the mean values. Instead, the maximum grayscale intensities of each particle images were evaluated and a threshold was set at 70% of their difference. Then, the mean RGB values of all the pixels in the particle image, with a grayscale value above this threshold, were used as the RGB values of the particle image to be used in the color spaces and calibration computations. This method yielded consistently narrower distributions of color values for particles images recorded at the same temperature. Figure A.2d shows green crosses indicating the pixels used to calculate the mean values that determined the RGB values corresponding to each particle.

B. System Photographs

High resolution photos of the laboratory and and the experimental setup components are shown in Figures B.1-B.7.

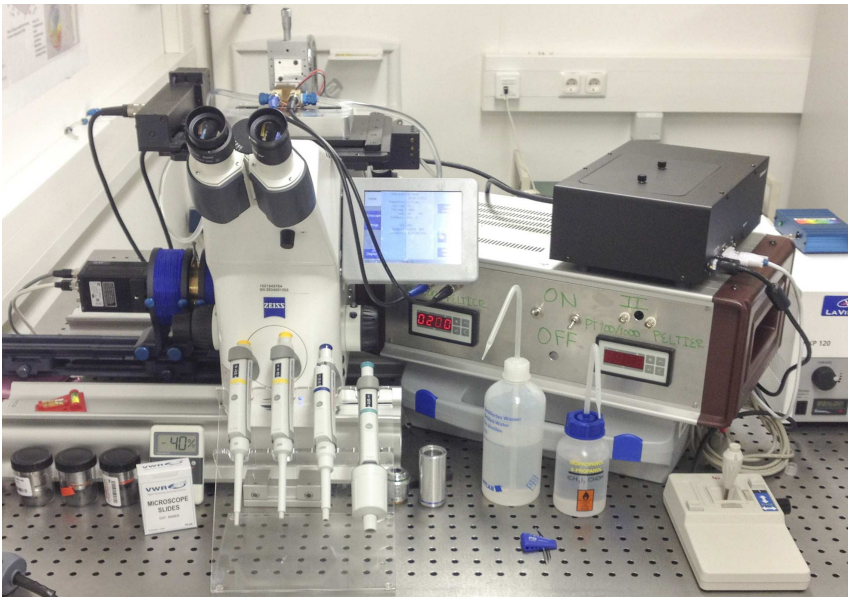

Figure B.1.: Imaging and temperature control system.

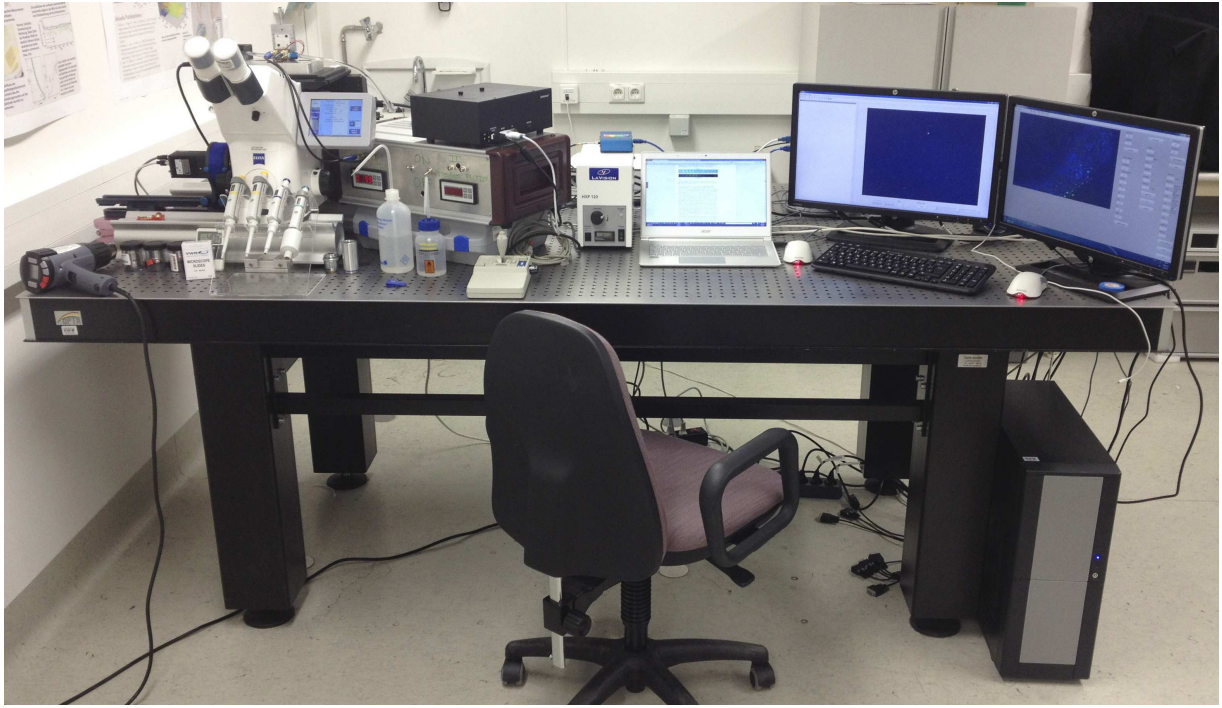

Figure B.2.: Microflulidics laboratory.

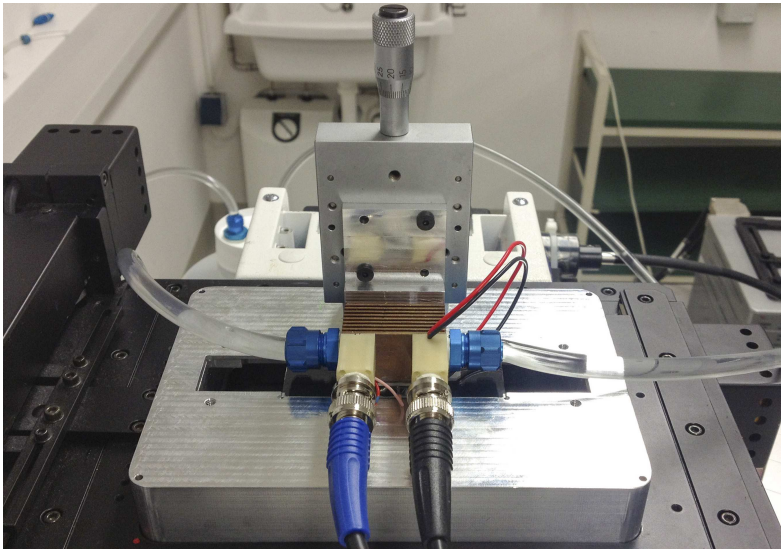

Figure B.3.: Temperature calibration experimental setup.

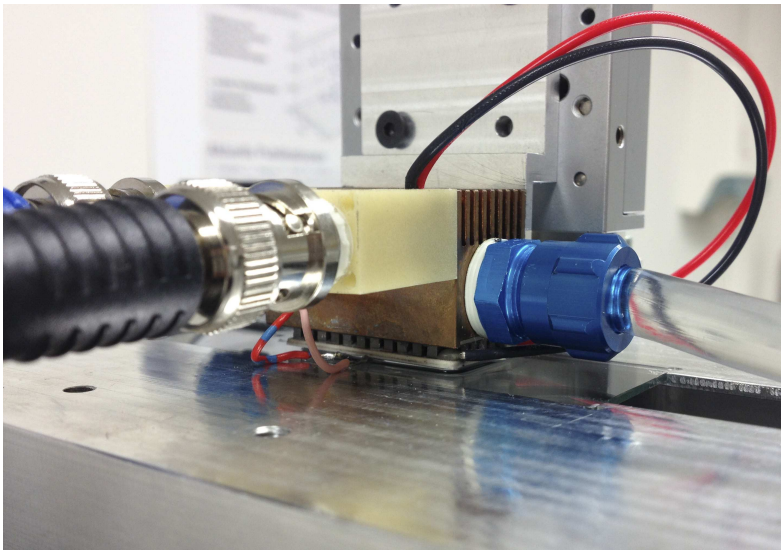

Figure B.4.: Temperature calibration experimental setup.

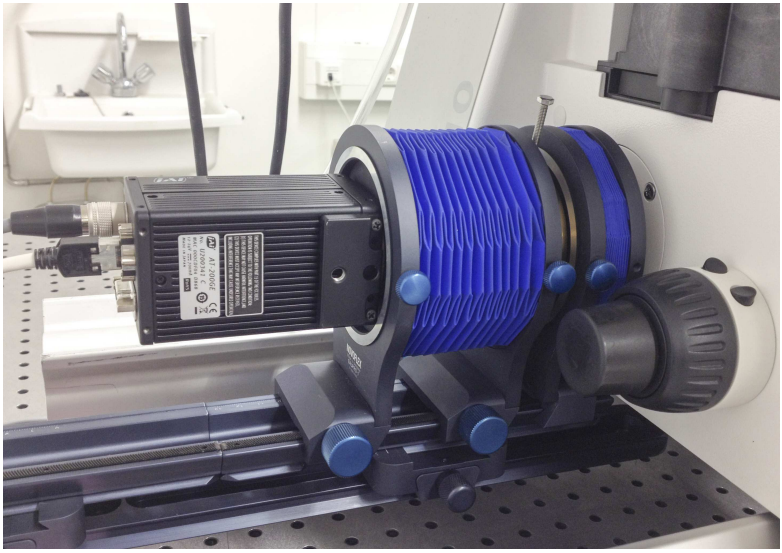

Figure B.5.: 3CCD color camera mounted behind cylindrical lens.

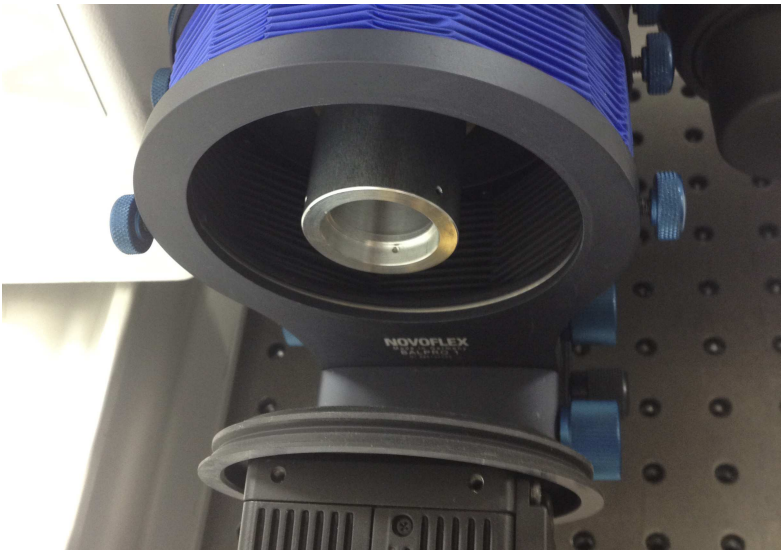

Figure B.6.: Cylindrical lens mount.

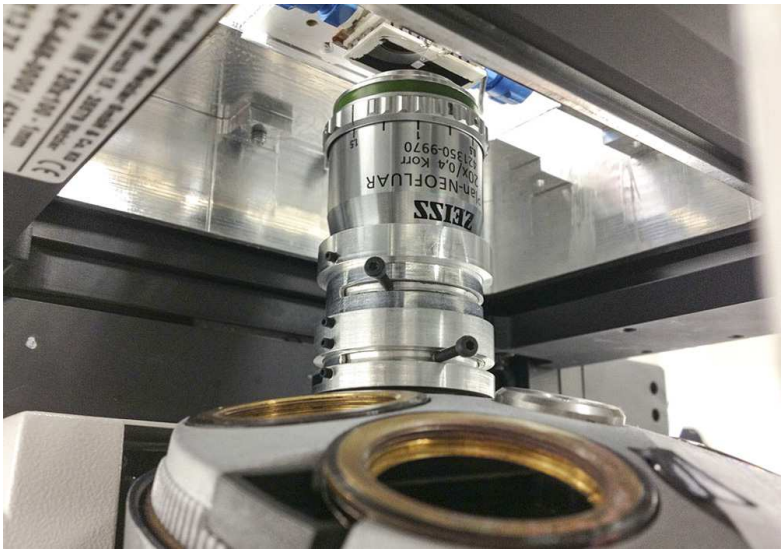

Figure B.7.: Circular polarization filter.